THE UNIVERSITY OF CHICAGO

TRAPPING A SINGLE ELECTRON ON SUPERFLUID HELIUM USING A SUPERCONDUCTING RESONATOR

A DISSERTATION SUBMITTED TO
THE FACULTY OF THE DIVISION OF THE PHYSICAL SCIENCES
IN CANDIDACY FOR THE DEGREE OF
DOCTOR OF PHILOSOPHY

DEPARTMENT OF PHYSICS

BY
GERWIN KOOLSTRA

CHICAGO, ILLINOIS
DECEMBER 2019

Table of Contents

List of Figures

List of Tables

ACKNOWLEDGMENTS

First and foremost, I must thank my PhD advisor David Schuster, who is a scientist and person of extraordinary caliber. Even after six years, I continue to be impressed by his unparalleled creativity, broad scientific curiosity and ability to see through the hardest physics problems. I have always felt welcome in the lab and comfortable to make a mistake, even some pretty stupid ones. Dave, thank you for your mentorship and advice in the final stages of my PhD, when it became time to find another adventure.

During the first couple of years Ge Yang taught me everything I needed to know about microwaves and electrons on helium. He taught me how to operate the fridge and very importantly: how to stay calm, even at 1:30 am when the fridge is about the explode. For most of my other skills I have to thank Dr. Dave McKay, who taught me the ins and outs of our simulations and fabrication methods, and we worked together on the lock box to stabilize the liquid helium. Thank you Dr. Dave for taking the time to be a teacher.

Over the years I was lucky to work with a few people more closely. Sam, even though you roam between labs, you always know to find me at my desk. I was glad to be part of the first few SAW resonator experiments. Abigail, thank you for giving me the opportunity to contribute to your titanium nitride work. Your diligence is admirable and I am sure you will continue to be successful as a graduate student. I have also had the pleasure to work with Andrew, who has a special talent for engineering and building beautiful, high-precision machined experiments. Thank you for your continued cryogenic advice and letting me use *Breton* for initial sample characterizations.

I also want to thank a few people whom I didn't get to work with closely, but who still made a significant impact on my graduate school career. Firstly, our post-doc extraordinaire Srivatsan Chakram, who taught me the physics I didn't know, but should know: thank you for your patience, your passion for physics and your company during the many mornings, afternoons and nights in the lab. Another thanks goes to Jon Simon, whose enthusiasm of condensed matter physics is contagious. His continued interest in the electrons-on-helium

project and help with the vibration problems were instrumental. Jon, I am also grateful for your role in my thesis committee and for giving me career advice. Nate and Ravi, both of your positive, good-natured personalities convinced me to join the lab and I regret we did not get the chance to work together more during our PhDs. Lastly, a shout-out to my office mates, Sasha, Ankur and Akash for their company, conversations, and patience, as they endured the terrible noise of the coffee grinder every morning.

Finally, I owe thanks to the people I love. Thank you to my parents and Kirsten, for being supportive of my decision to pursue grad school so far from home. And lastly, thank you to my soon-to-be wife, Mary, who has supported me more than she knows. She kept me sane when experiments drove me insane and cheered me up when experiments had put me down. Without her love and support this thesis would not be here.

ABSTRACT

Electrons on helium form a unique two-dimensional system on the interface of superfluid ^{4}He and vacuum. At low temperatures and weak confinement, trapped electrons can arrange into strongly correlated states known as Wigner molecules, which can be used to study electron interactions in the absence of disorder, or as a promising resource for quantum computation. Wigner molecules have orbital frequencies in the microwave regime and can therefore be integrated with circuit quantum electrodynamics, which would allow rapid detection and manipulation of such a molecule's orbital state.

In this thesis, we demonstrate deterministic preparation of one to four-electron Wigner molecules in an electron-on-helium quantum dot located at the tip of an on-chip microwave resonator. The Wigner molecule dipole coupling to the resonator allows us to measure spectral features of Wigner molecules in the microwave regime. We find that different-sized Wigner molecules have strikingly different spectra, and each spectrum serves as a fingerprint for the molecule's internal structure and its surroundings. By modeling the electron-cavity system, we extract each molecule's orbital frequency and electron configuration. For a single electron, the orbital frequency crosses the cavity resonance and we measure a large coherent electron-photon coupling rate of $g/2\pi = 4.8$ MHz, which exceeds the incoherent cavity decay rate by ten times. These results provide a solid base for the development of an electron-on-helium qubit. Looking forward, our platform allows for new microwave studies of strongly correlated electron states and can be used to couple a single microwave photon to a single electron spin.

CHAPTER 1

INTRODUCTION

1.1 Electrons on helium

1.1.1 The quantum mechanics of an electron floating on liquid helium

As an experimental physicist, it is rare to encounter a stable, trapped elementary particle. Such particles are usually embedded within matter (e.g. an electron in a solid state defect), and are easiliy perturbed or absorbed (e.g. photons trapped in a cavity). An electron on helium is unique in this respect, since it forms a stable isolated quantum system on the interface of liquid helium and vacuum. Electrons on helium naturally float approximately 10 nm above the helium surface [1] and can move across this surface almost effortlessly, so they can be thought of as microscopic quantum hoverboards. This behavior is quite remarkable, but can be explained by the competition between an attractive force between the electron and its induced image charge, and a repulsive barrier caused by the helium surface.

The image charge is induced below the liquid helium surface and is schematically depicted in Fig. 1.1. Continuity of the displacement $\varepsilon_i E_\perp$ perpendicular to the helium surface dictates that the image charge is of opposite sign [2]

$$q' = e\frac{\varepsilon_{\mathrm{He}} - 1}{\varepsilon_{\mathrm{He}} + 1}, \tag{1.1}$$

where $\varepsilon_{\mathrm{He}} = 1.056$ is the dielectric constant of liquid helium [3], and therefore attracts the negative electron towards the helium surface. The repulsive force that balances the electrostatic force arises from the energy that is needed to place an electron inside the bulk helium. In that case, the electron energy is minimized when it is at the center of a vacuum bubble. The energy needed to form this electron bubble amounts to

$$E \approx \frac{h^2}{8m_e R^2} + 4\pi\sigma R^2, \tag{1.2}$$

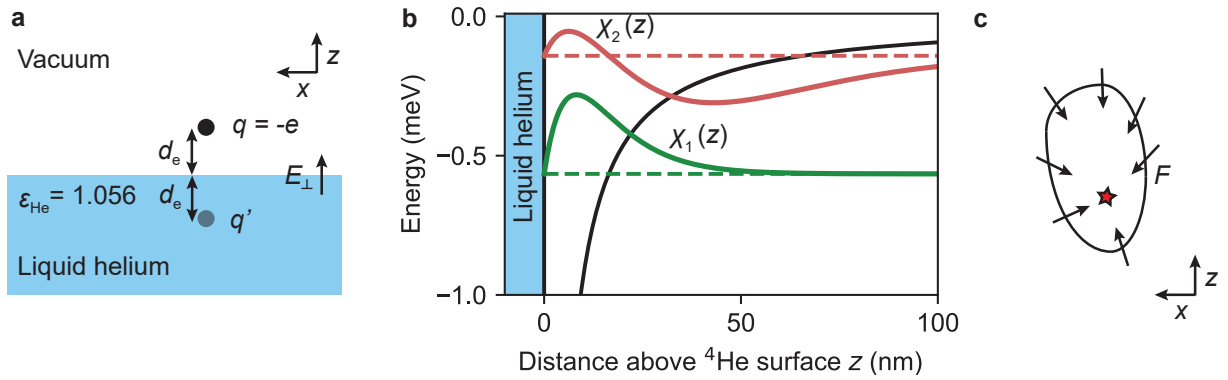

Figure 1.1: (a) An electron on floating a distance d_e above a liquid helium surface induces an image charge inside the helium a distance d_e below the surface. An electric pressing field $E_\perp$, generated by a positively biased submersed electrode (not shown), is used in experiments to control the electron density. (b) Electronic wavefunctions for the ground state $|1\rangle = \chi_1(z)$ and first excited state $|2\rangle = \chi_2(z)$ obtained by solving the Schrödinger equation (Eq. (1.6)). The potential $V(z)$ in the absence of a pressing field $E_\perp$ is shown as a solid black line and dashed lines indicate energy levels E_1 and E_2. The expected position in the ground (first excited) state is approx. 11 (46) nm above the surface. (c) A stable electron trap must have a force F pointing towards an electrostatic potential minimum, indicated by a red star. This means there must be a net flux of electric field lines through the surface around the potential minimum (solid black line), which contradicts Maxwell's equations for electrostatic potentials in vacuum. Electrons on helium can be trapped using electrostatic potentials since the helium provides a restoring force.

where the first term in Eq. (1.2) represents the zero-point energy of the electron and the second term represents the energy to warp the surface [4, 5], with σ and R the surface tension of liquid helium and radius of the bubble, respectively. Experiments performed by Sommer in 1964 [6] measured the energy for electrons to penetrate the surface and form such bubbles to be 1.3 eV.

An electron on helium and its positive image charge resemble the canonical quantum mechanical system of a hydrogen atom, where instead of an electron orbiting the positively charged proton, an electron on helium is bound to the surface by its image charge, resulting in the potential energy

$$V(z) = V_0\theta(-z) - \frac{\Lambda}{z + z_0}\theta(z) + eE_\perp z, \tag{1.3}$$

where $V_0 \approx 1$ eV [1, 6] is the helium penetration barrier, $\theta(z)$ is the step function, $E_\perp$ is the electric field always present in experiments, $z_0 \approx 1.01$ Å is an offset to avoid the singularity at the helium surface $z = 0$ and

$$\Lambda = \frac{e^2}{4\pi\varepsilon_0\varepsilon_{\mathrm{He}}}\frac{1}{4}\frac{\varepsilon_{\mathrm{He}}-1}{\varepsilon_{\mathrm{He}}+1}. \tag{1.4}$$

The analogy between an electron on helium and the hydrogen atom becomes more clear when we solve the Schrodinger equation for an electron on helium:

$$-\frac{\hbar^2}{2m_e}\nabla^2\psi(\mathbf{r},z) + V(z)\psi(\mathbf{r},z) = E\psi(\mathbf{r},z). \tag{1.5}$$

Without confinement in the plane of the helium surface, the wavefunction $\psi(\mathbf{r},z)$ must be a plane wave normalized by the surface area S: $\psi(\mathbf{r},z) = \frac{1}{\sqrt{S}}e^{i\mathbf{k}\cdot\mathbf{r}}\chi_n(z)$. Plugging in this ansatz gives an equation for the wavefunction in the z-direction:

$$\frac{d\chi_n(z)}{dz^2} + \frac{2m_e}{\hbar^2}\left(E_n - V\right)\chi_n(z) = 0. \tag{1.6}$$

In the simplest case of no electric field ($E_\perp = 0$), this equation can be solved by approximating the helium surface as an infinite potential barrier ($V_0 \to \infty$ and $z_0 \to 0$). This yields eigenenergies

$$E_n = -\frac{m_e}{2\hbar^2 n^2}\Lambda^2 \quad (n = 1, 2, 3, \ldots) \tag{1.7}$$

which resemble the spectrum of the hydrogen atom:

$$E_n = -\frac{m_e}{2\hbar^2 n^2}\left(\frac{e^2}{4\pi\varepsilon_0}\right)^2. \tag{1.8}$$

The transition energies of an electron on helium can therefore be straightforwardly mapped onto those of the hydrogen atom with a modified Rydberg constant.

In an experimental setting, an electric field $E_\perp$ is always present to control the two-

dimensional electron density. Solving Eq. (1.6) with the full expression for $V(z)$ can be done numerically, and results in a linear Stark shift for electrons on helium:

$$\Delta E_n \approx eE_\perp \langle n|z|n\rangle. \tag{1.9}$$

Note that the Stark shift is positive, indicating that the transition frequencies increase with $E_\perp$, which was experimentally verified by Grimes *et al.* in 1976 [7].

In the absence of $E_\perp$, the energy difference between the ground and first excited state amounts to approximately $(E_2 - E_1)/h \approx 119$ GHz, and $(E_3 - E_1)/h \approx 141$ GHz. The ground state wave function has its expected value $\langle 1|z|1\rangle \approx 11$ nm above the helium surface (Fig. 1.1b) and for higher excited states, the average distance to the helium surface $\langle n|z|n\rangle$ increases. For example, the first excited state floats approximately $\langle 2|z|2\rangle \approx 46$ nm above the surface. This dependence can be exploited for vertical state detection, for example by using a nearby capacitor which detects small changes in induced charge. Control and read-out of these states is an important requirement for an electron-on-helium quantum computer, which has been proposed almost two decades ago [8, 9] and is still actively explored today [10].

The transition frequency $(E_2 - E_1)/h$ is much larger than conventional microwave frequencies but smaller than optical frequencies, and lack of available off-the-shelf technology in this regime has slowed down progress towards coherent control of the vertical energy states of electrons on helium. On the other hand, the large transition frequency also implies that at temperatures below $T \ll (E_2 - E_1)/k_B \approx 6$ K, an electron on helium is well cooled to its vertical ground state. Such low temperatures are easily reached in commercial cryogenic systems, opening the door for exploring other degrees of freedom, such as its motion parallel to the helium surface.

With the electron's vertical degree of freedom frozen in the ground state, the electron can move effortlessly across the helium surface unless it is further confined in the plane of the

helium surface. Confining the electron in the x, y plane fully quantizes the electron states, and forms the basis of an electron-on-helium motional state qubit. Unlike trapped ions, electrons on helium are trapped by direct current (DC) electrostatic potentials, rather than alternating current (AC) potentials. At first glance, this seems to contradict Earnshaw's theorem, which states that point charges in vacuum cannot be trapped using only a DC voltage. Let us briefly discuss why this does not hold for electrons on helium.

From Maxwell's equations, any DC electric field $\mathbf{E}$ used to create a stable trap must be divergence free: $\nabla \cdot \mathbf{E} = 0$. In other words, the flux of electric field lines through a surface around a potential minimum most add to zero. However, a stable electrostatic trap must have a force pointing towards a potential minimum, as depicted in Fig. 1.1c. This requires a net flux of electric field lines through this surface, and thus contradicts the first requirement. Therefore, according to Earnshaw's theorem, a stable trap generated by DC potentials does not exist in vacuum.

For electrons on helium it *is* possible to create a stable trap with electrostatic potentials, since the electron is bound the the helium surface. The helium surface therefore provides a restoring force for the electric field perpendicular to the helium surface that would otherwise create an unstable trap in vacuum. An electron on helium can therefore be trapped simply by applying a positive DC voltage to a submersed electrode.

1.1.2 Electron interactions on liquid helium

Electrons floating above a helium surface behave differently from electrons in a metal or a semiconductor, because electrons reside in the vacuum rather than a high-ε dielectric substrate. This has a number of important consequences for interactions between electrons above the helium.

Interactions between electrons in semiconductors are often screened, meaning that their

interaction energy $U(r)$ is not described by the familiar Coulomb interaction

$$U(r) = \frac{e^2}{4\pi\varepsilon_0\varepsilon_s}\frac{1}{r}, \tag{1.10}$$

but is modified to the so-called Yukawa potential [11]:

$$U(r) = \frac{e^2}{4\pi\varepsilon_0\varepsilon_s}\frac{e^{-r/\lambda}}{r}, \tag{1.11}$$

where λ is the screening length and ε_s is the dielectric constant of the substrate. Without nearby charges or dielectrics, the screening length is infinite and $U(r)$ reduces to the typical Coulomb interaction. A finite screening length arises when electrons are placed near a dielectric substrate or conducting surface, such that $\lambda \approx 2d$, where $2d$ is the distance between the electrons and their induced image charges. Physically, a finite screening length reduces the repulsion between electrons, since image charges divert electric field lines into the nearby dielectric. This reduces the inter-electron distance, causes the electron wavefunctions to overlap and makes it harder to observe strongly-correlated electron physics [12]. In addition, these high-ε semiconductors are often artificially grown in a cleanroom and often come with impurities that destroy long-range order [13].

An ensemble of electrons on helium resides in the vacuum and the closest dielectric is liquid helium, which has a low dielectric constant $\varepsilon_{\mathrm{He}} = 1.056$. Interactions between electrons on helium are therefore almost purely Coulombic. The dominant corrections to the Coulomb interaction do not come from the helium surface, but rather originate from conducting electrodes below the helium surface, which are needed to provide a trapping potential or pressing field $E_\perp$ for the ensemble. However, these corrections are small compared to those in semiconductors, since electrons typically float far above the electrodes (approx. 1 µm).

Coulomb interactions are long-range and can give rise to long-range order. At sufficiently low temperatures, electrons on helium arrange into a two-dimensional hexagonal lattice, called a Wigner crystal or Wigner solid. Electrons on helium are one of the few physical

systems that exhibit this behavior, since the liquid helium substrate is atomically smooth and free of defects that may destroy long-range order.

Analogously to freezing a liquid, a Wigner crystal forms if the potential energy (i.e. interaction energy) of an electron ensemble dominates the kinetic energy [14]. The first measurements performed by Grimes and Adams in 1979 [15], established that when the ratio of the potential to kinetic energy

$$\Gamma = \frac{U}{E_{\text{kin}}} = \frac{e^2\sqrt{\pi n_s}}{4\pi\varepsilon_0\varepsilon_{\text{He}}k_BT} \tag{1.12}$$

exceeds 137, the ensemble forms a Wigner solid. In Eq. (1.12) n_s is the surface electron density in m^{-2} and k_B is Boltzmann's constant. In contrast, for $\Gamma < 137$ the thermal energy k_BT is large enough to introduce crystal defects and destroy long-range order, such that the ensemble transitions into an electron fluid. These two different regimes are traditionally studied with capacitive transport measurements, where the Wigner crystal phase is distinguished from the liquid phase by its lower conductivity [1, 16, 17].

The Wigner solid phase is an example of a strongly-correlated electron system, since the interaction energy is over one hundred times larger than the kinetic energy. In this regime the typical electron density ranges from $n_s = 10^9$ m^{-2} to 10^{13} m^{-2}, which corresponds to a Wigner crystal lattice spacing of order $r = (\pi n_s)^{-1/2} \approx 0.1 - 10$ µm. Under these conditions a Wigner crystal melts at a few hundred milliKelvin. The melting behavior of a Wigner crystal and how this is affected by Wigner crystal confinement, applied voltage and commensurability, are still active research topics in this field [17–21].

1.1.3 Properties of the liquid helium substrate

The Wigner solid phase is destroyed if long-range order is interrupted by substrate defects, so we typically do not observe the Wigner solid phase in semiconductors, except in ultra clean one-dimensional carbon nanotubes [12, 22]. In contrast to even the cleanest semiconductors,

liquid helium offers an atomically smooth interface that supports long-range order and the formation of a two-dimensional Wigner solid. There are a number of other important properties that make liquid helium a unique electronic substrate. In this section, we highlight the superfluid properties from an experimentalist's point of view and discuss possible alternative electronic substrates to liquid ^{4}He.

When gaseous ^{4}He is cooled below $T_\lambda = 2.1$ K, it first condenses and then transforms into a superfluid. In the two-fluid model of superfluidity, liquid helium consists of a normal fluid and a superfluid. The normal fluid fraction decreases exponentially with temperature and below 100 mK, the entire fluid can be thought of a superfluid, which has zero viscosity and flows through microscopic holes inaccessible to the normal component, as long as the velocity of superfluid flow does not exceed a critical value[1]. As a result, superfluid helium leaks may spontaneously appear at low temperatures and cause inadvertent heating. Luckily they can be prevented by properly sealing the liquid helium container with indium seals or by using film burners [23].

The persistent flow of superfluid helium also causes superfluid film creep, a phenomenon where a thin superfluid film seemingly defies gravity by creeping up the walls of its container. The thickness of this film d depends on the height h measured from the superfluid-vacuum interface

$$d = \left(\frac{\alpha_{\mathrm{He}}}{mgh}\right)^{\frac{1}{3}}, \tag{1.13}$$

where α_{He} is the van der Waals constant, and d typically amounts to 30 nm [24]. In the experiments presented in this thesis, we rely on the superfluid film creep to fill our microchannels with superfluid helium (section 4.1).

Liquid helium is host to a range of excitations, such as first, second and third sound [25], rotons [26] and ripplons [27]. Electrons on helium are most affected by phonons (i.e. bulk density waves) and ripplons (i.e. surface waves), which limit the mobility of surface electrons and affect the coherence properties of the vertical Rydberg states [8, 9] and electron motional

1. This critical velocity is much like the critical current density for superconductors.

states [28] (section 1.3.2).

Classicaly, ripplons can be thought of as capillary waves on the liquid helium surface, similar to surface acoustic waves in piezo-electric substrates. However, unlike these Raleigh waves ripplons follow an anomalous dispersion relation ($\omega \neq ck$), which consists of two parts:

$$\omega_{\mathbf{k}}^2 = \frac{\sigma}{\rho}\left(\mathbf{k}^2 + \kappa^2\right)|\mathbf{k}|\tanh\left(|\mathbf{k}|d\right), \tag{1.14}$$

where $\omega_{\mathbf{k}}/2\pi$ is the ripplon frequency, $\mathbf{k}$ is the wave vector, $\kappa^2 = \rho/\sigma\left(g + 3\alpha_{\mathrm{He}}/\rho d^4\right)$ and d is the liquid helium film thickness. The first part in Eq. (1.14) is the contribution of capillary waves and becomes dominant for short wavelengths (large k), whereas the second part describes the gravity waves with dispersion $\omega_{\mathbf{k}} \approx \sqrt{g|\mathbf{k}|}$. Ripplons are important to electrons on helium because they distort electronic wavefuctions and cause energy relaxation and dephasing of quantized electron-on-helium states.

Liquid helium is an excellent electron substrate but it is not the only cryogenic substrate known to bind electrons. Solid hydrogen ($\varepsilon_{\mathrm{H_2}} = 1.28$ [29]) and solid neon, which freeze at 14.0 K and 24.5 K, respectively also bind electrons and are attractive, because they can support much larger electron densities; unlike the liquid helium surface, a solid cannot buckle under the electron pressure. In addition, these substrates are insensitive to external vibrations. On the other hand, solid H_2 or Ne crystallize in micron-sized domains such that the free surface is not as smooth as that of liquid ^{4}He. As a consequence, electrons on solid substrates typically have lower mobilities than on liquid helium [1] and are not studied as extensively.

1.1.4 Strongly correlated few-electron states

At low temperatures and electron densities below $n_s \sim 10^{13}$ m^{-2} a large electron ensemble on helium forms a Wigner crystal. Under approximately similar conditions, a small number of trapped electrons also forms a strongly interacting state of matter, which resembles an

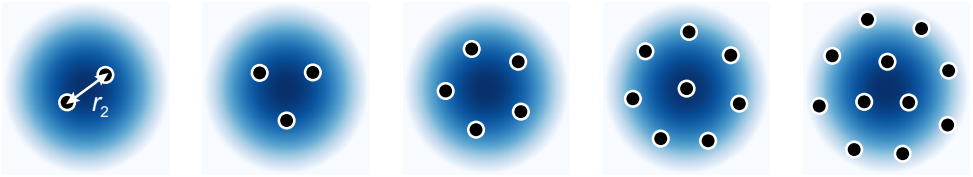

Figure 1.2: Electron molecule (Wigner molecule) configurations for 2, 3, 5, 8 and 11-electron molecules in a harmonic electrostatic potential.

electron molecule rather than a crystal (Fig. 1.2). Accessing the interesting few-electron regime, where the molecule's symmetry changes drastically upon adding or subtracting a single electron, requires precise control over single electrons in an electrostatic trap.

Experimental control over single electrons on helium was established in the late 2000's in the experiments by Papageorgiou *et al.*, who used a micron-sized pool with a concentric guard electrode to trap only a few electrons [30, 31]. With the detection of Wigner molecules in a similar quantum dot, Rousseau *et al.* introduced electron-on-helium dots as a platform for strongly correlated electron-on-helium physics [32]. Below, we briefly discuss the defining properties of Wigner molecules and the conditions for which they appear.

Wigner molecules

Wigner molecules are strongly correlated electron states that form if a small number of electrons are trapped in an electrostatic potential, while they are subject to weak confinement and low temperatures. They are easily distinguished from few-electron states in semiconductors, where the electron wavefunctions overlap and form a more homogeneous charge distribution inside the dot. The charge distribution of a Wigner molecule peaks sharply around the classical electron positions and the symmetry of a Wigner molecule changes drastically with the number of electrons N and shape of the confinement potential.

Before describing the formation of Wigner molecules, it is instructive to solve for the quantum mechanical wavefunction of the simplest Wigner molecule, which consists of two electrons in a harmonic potential. These wavefunctions will show characteristic Wigner molecule features, and the relevant parameters for Wigner molecule melting become appar-

ent.

Two electrons in a one-dimensional trap

Schrödinger's equation for two electrons in a one-dimensional harmonic well $eV(x) = \frac{1}{2}m_e\omega_{\text{trap}}^2 x^2$ is given by

$$\left[-\frac{\hbar^2}{2m_e}\left(\frac{\partial^2}{\partial x_1^2}+\frac{\partial^2}{\partial x_2^2}\right)+\frac{e^2}{4\pi\varepsilon_0}\frac{1}{|x_1-x_2|}+\frac{1}{2}m_e\omega_{\text{trap}}^2(x_1^2+x_2^2)\right]\Psi(x_1,x_2)=E\Psi(x_1,x_2) \tag{1.15}$$

where x_1 and x_2 are the position of the two electrons. To solve this equation, we may transform to a common coordinate $x_c = x_1 + x_2$ and a differential coordinate $x_d = x_1 - x_2$.

$$\left[-\frac{\hbar^2}{m_e}\left(\frac{\partial^2}{\partial x_c^2}+\frac{\partial^2}{\partial x_d^2}\right)+\frac{e^2}{4\pi\varepsilon_0}\frac{1}{|x_d|}+\frac{1}{4}m_e\omega_{\text{trap}}^2(x_c^2+x_d^2)\right]\Psi(x_c,x_d)=E\Psi(x_c,x_d) \tag{1.16}$$

In this form Eq. (1.16) becomes separable[2] if we let $\Psi(x_c, x_d) = \psi(x_c)\phi(x_d)$. This leaves two equations for $\psi(x_c)$ and $\phi(x_d)$:

$$-\frac{\hbar^2}{m_e}\frac{\psi''}{\psi}+\frac{1}{4}m_e\omega_{\text{trap}}^2 x_c^2=\lambda_1 \tag{1.17}$$

$$-\frac{\hbar^2}{m_e}\frac{\phi''}{\phi}+\frac{e^2}{4\pi\varepsilon_0|x_d|}+\frac{1}{4}m_e\omega_{\text{trap}}^2 x_d^2=\lambda_2, \tag{1.18}$$

where $\lambda_{1,2}$ are the eigenenergies corresponding to the common and differential motion, respectively. Eqs. (1.17) and (1.18) can be solved numerically by discretizing $x_{c,d}$ and solving the corresponding system of equations in matrix form. The eigenmodes $\psi(x_c)$ are shown in Fig. 1.3, represent common-mode electron motion and closely resemble Hermite polynomials. The eigenmodes $\phi(x_d)$ are more interesting and indicate that the average separation

2. This transformation is not specific to the Coulomb interaction but works for any interaction that only depends on the distance between the two electrons. For anharmonic potentials $V(x)$, this transformation breaks down, unless the $V(x_1) + V(x_2) = f(x_c) + g(x_d)$ separates into two functions of x_c and x_d. For example, adding an x^4 term to $V(x)$ does not result in a separable equation.

between the electrons is sharply peaked around the classical position (see Fig. 1.2)

$$r_2 = \left(\frac{e^2}{2\pi\varepsilon_0 m_e \omega_{\text{trap}}^2} \right)^{\frac{1}{3}}. \tag{1.19}$$

Since the extent of the wavefunction l_0 is much smaller than the electron separation r_2, the overlap between individual electron wavefunctions is negligible, which is a direct result of the strong Coulomb interaction. The sharply peaked, non-overlapping wavefunctions are characteristic features also seen in larger Wigner molecules [33].

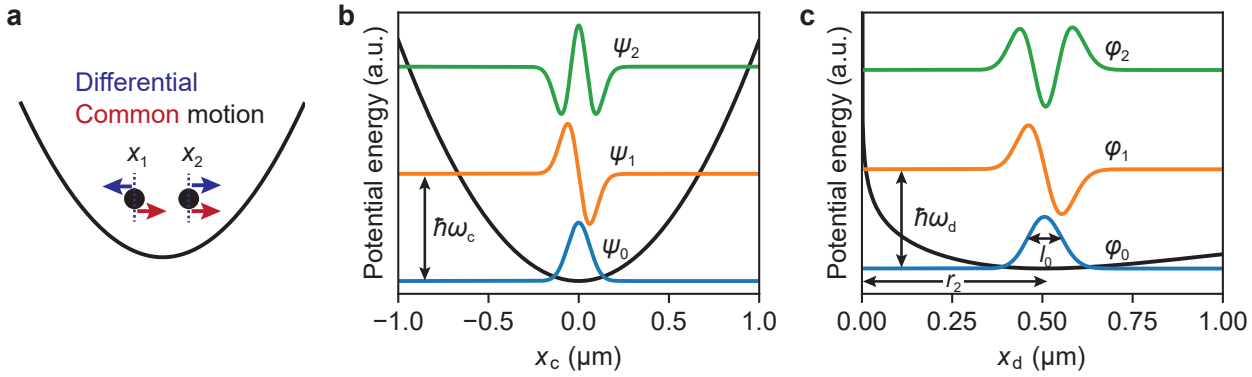

Figure 1.3: (a) Two types of motion for two electrons trapped in a harmonic electrostatic potential with trap frequency $\omega_{\text{trap}}/2\pi = 10$ GHz. (b) The wavefunctions for common motion $\psi(x_c)$ are centered around $x_c = x_1 + x_2 = 0$, meaning $x_1 = -x_2$ and the spectrum is equally spaced with frequency $\omega_c = \omega_{\text{trap}}$. The potential energy $V(x_c) = \frac{1}{2} m_e \omega_{\text{trap}}^2 x_c^2$ is shown as a solid black line. (c) Same as in (b) for the relative (differential) electron motion $x_d = x_1 - x_2$. The potential energy $eV(x_d)$ is shown in log-scale to show the divergence of the Coulomb interaction at $x_d = 0$ and the minimum of the potential at $x_d \approx 0.5$ μm. The two electrons are separated by $r_2 \approx 0.5$ μm for $\omega_{\text{trap}}/2\pi = 10$ GHz. The size of the wavefunction is given by $l_0 = \sqrt{\hbar/(m_e \omega_{\text{trap}})}$. The frequency $\omega_d/2\pi = 17$ GHz is larger than the common mode frequency $\omega_c = \omega_{\text{trap}}$, since the Coulomb interaction stiffens the spring constant.

Phase diagram of Wigner molecules

Eq. (1.19) suggests that the electron separation varies with confinement via ω_{trap}. For very large ω_{trap} the electron separation is so small that wavefunctions will start to overlap, which initiates Wigner molecule melting [34, 35]. In addition, finite temperature broadens the

eigenfunctions $\phi(x_d)$ and may also melt Wigner molecules.

The concept of Wigner molecule melting due to confinement and finite temperature, for arbitrary number of electrons N, is more generally parametrized by the two variables

$$\Gamma = \frac{E_c}{k_B T} = \frac{e^2}{4\pi\varepsilon_0 r_0 k_B T} \tag{1.20}$$

$$\bar{n} = \sqrt{2}\left(\frac{l_0}{r_0}\right)^2, \tag{1.21}$$

where $l_0 = \sqrt{\hbar/m_e\omega_{\text{trap}}}$ is the spatial extent of the electron wavefunction and $r_0 \approx r_2$ is the average electron separation. A Wigner molecule phase diagram, which can be found in Refs. [32, 35], shows that for low $\bar{n} \lesssim 1/\sqrt{37}$ and large $\Gamma > 137$ (i.e. low T) electrons arrange into Wigner molecules. This is consistent with previous statements, since $\bar{n}$ is a measure of wavefunction overlap and $1/\Gamma$ a measure of temperature. It should be noted that the melting transition is broad, occurs in two stages [35], and the melting temperature of a Wigner molecule depends strongly on the number of electrons N and the shape of the potential $V(x)$, if it is not harmonic. We can estimate however, that for a harmonic potential with $\omega_{\text{trap}}/2\pi = 6.5$ GHz, Wigner molecules are expected to form when $T \lesssim 0.2$ K.

The established method of detecting Wigner molecules is through the unequal spacing in the addition spectrum of an electron-on-helium dot [32]. The addition spectrum is usually measured by varying the dot's trap depth while monitoring changes in occupation of the dot. While the unequal step size signals the presence of Wigner molecules it is not a sensitive probe for the internal charge distribution of Wigner molecules. The coherent motion of these molecules parallel to the helium surface can serve as an additional, more sensitive probe of the internal structure of Wigner molecules. However to date, the common and differential motion of Wigner molecules have never been observed due to a lack of a microwave interface. By designing an electron trap in the microwave range ($\omega_{\text{trap}}/2\pi \approx 0 - 10$ GHz) and by integrating it with a microwave resonator, measurement of the electron motion becomes feasible. This could shed light on the two-stage melting process and could lead to a qubit

based on the orbital state of an electron on helium [28].

1.1.5 Electrons on helium as quantum bits

A single electron floating in vacuum is far away from substrate impurities and voltage noise from electrodes, making it a well-isolated quantum system and therefore, a potentially promising building block for a solid-state quantum computer. Using any quantum system as a resource for quantum computation requires two clearly defined states, which are long-lived and can be manipulated to perform single qubit gates for quantum algorithms [36]. Quantum algorithms make use of superposition and entanglement to solve a special subset of problems more efficiently than classical computers [37]. It is important that the quantum states do not decay or lose their phase information during a computation. Therefore, quantum bits (qubits) are often ranked by their T_1 (decay) and T_2 (dephasing) coherence times. Electrons on helium possess three degrees of freedom that have been studied for their potential as qubits: the vertical degree of freedom, the electron spin and the orbital (lateral) motion (Fig. 1.4).

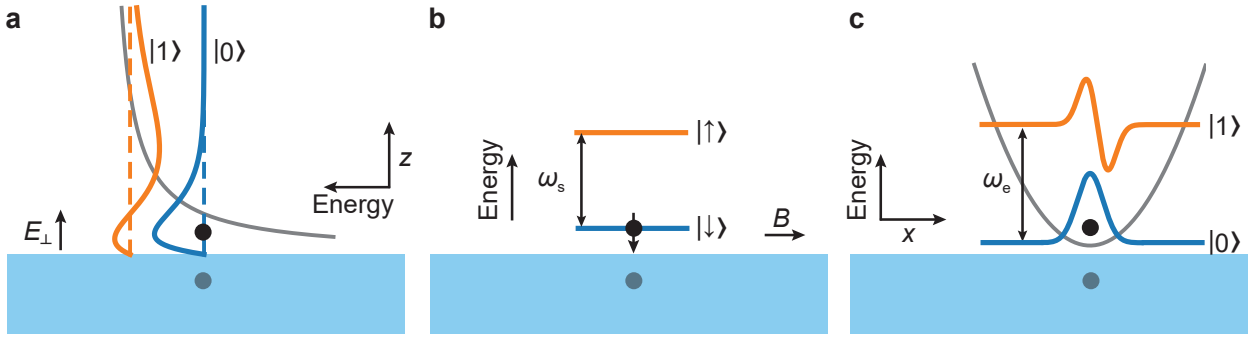

Figure 1.4: One electron on helium, three different qubits. For each type of qubit, the ground state and excited state are shown in blue and orange, respectively. (a) Electron-on-helium qubit composed of the vertical ground state $|0\rangle$ and first excited state $|1\rangle$. In the first excited state, the expected electron position is approx. 46 nm above the helium surface. (b) Electron-on-helium spin qubit. The splitting between the qubit states tunes with the applied B field. (c) The electron motional state forms a qubit when an electron is confined in an anharmonic electrostatic trap. The qubit frequency ω_e is set by the trap (gray) curvature.

The vertical ground and excited state are natural candidates for a quantum bit due to the

anharmonic hydrogenic excitation spectrum, given by Eq. (1.7). The transition energy of such a qubit is 119 GHz and tunes with voltage via a Stark shift. The lifetime of the vertical excited state is limited by coupling to ripplons on the liquid helium surface. Fortunately, this coupling is small, resulting in a rather long $T_2 \approx 10^{-4}$ s [8]. Even though this vertical qubit was proposed over two decades ago, little progress has been made due to the lack of experimental technology in this frequency range.

The electron spin is another straightforward qubit candidate, since its spectrum splits into two distinct eigenstates ($m_s = \pm\frac{1}{2}$) in the presence of a magnetic field, labeled as $|\uparrow\rangle$ and $|\downarrow\rangle$. The energy difference between these states is given by the Zeeman energy and can thus be tuned with the static magnetic field B:

$$\hbar\omega_s = E_\uparrow - E_\downarrow = g\mu_B B, \tag{1.22}$$

where $\mu_B = e\hbar/2m_e$ is the Bohr magneton and $g = 2.0023\ldots$ is the Landé g-factor for electrons. For an applied field of $B = 0.2$ T, the qubit transition frequency is $\omega_s/2\pi \approx 5$ GHz, which allows for qubit manipulation with conventional microwave equipment. The electron spin is unique, since it is extremely well isolated: its dominant dephasing mechanism is due to Johnson noise in trap electrodes which only limits dephasing to $T_2 \approx 1.5$ s [38].

Because the electron spin is so isolated, signals from single spins are hard to detect. One way to detect such small signals is by imprinting the signatures of the target spin onto an auxilary spin. However, achieving a reasonable spin-spin interaction rate requires very small inter-electron distances, which is only possible on very thin helium films. This is technically challenging, since any roughness in the trapping electrodes could result in unwanted electron traps. Instead of using an auxilary electron for spin manipulation and detection, one can also use the electron orbital state in conjunction with a magnetic field gradient, which is discussed in more detail in section 6.2. To date, no one has performed electron spin resonance with electrons on helium, so observing a coherent signal of a single electron spin on helium would

be a monumental result.

Analogously to the mechanical motion of a trapped ion, the lateral motion of a trapped electron in an anharmonic potential also constitutes a qubit (Fig. 1.4c) [28]. In this case, the qubit consists of the ground and first excited state of the electron motion in an electrostatic trap. This electrostatic trap is formed by submersed electrodes and is naturally anharmonic, such that the first excited state can be addressed without exciting higher motional states. The qubit frequency depends on the trap curvature, varies with voltage and is nominally in the GHz regime, allowing for integration with planar on-chip microwave resonators for fast manipulation and read-out of electron motion [28]. This thesis deals with the experimental implementation of such a qubit using circuit quantum electrodynamics, the field of physics that studies light-matter interactions using microwave photons.

1.2 Introduction to circuit quantum electrodynamics

1.2.1 The Jaynes-Cummings Hamiltonian

Cavity quantum electrodynamics (cavity QED) uses photons confined in optical cavities to study atoms (or other particles), which can couple to the electric field of photons inside the cavity [39]. Under these conditions, the quantum nature of photons as well as the atoms becomes important and experimentally accessible. This has sparked a huge advancement in the fields of quantum optics, quantum information processing and the understanding of fundamental quantum physics.

Circuit quantum electrodynamics (circuit QED) was developed as a variant of cavity QED [40], and studies the interaction between photons and matter at microwave frequencies (Fig. 1.5). Instead of optical cavities, microwave photons can be confined in superconducting microwave resonators. These photons are much less energetic than their optical counterparts, but can be confined in a much smaller volume than an optical photon, resulting in an increased coherent interaction rate with “atoms”.

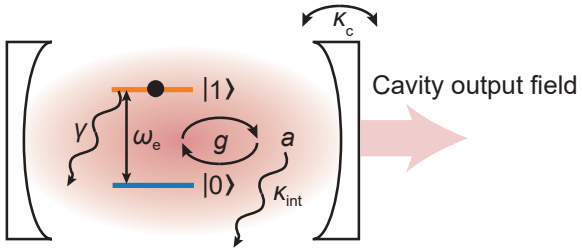

Figure 1.5: A cavity (circuit) QED system consists of an atom embedded in an optical (microwave) cavity. The intracavity field (denoted by a) leaks out at a rate $\kappa_c + \kappa_{\text{int}}$, where κ_c is the mirror transparency and κ_{int} encompasses photon absorption or photon emission into modes not captured by the detector. The intracavity field couples to the two-level system at a rate g, which in turn decays to the environment at rate γ.

Circuit QED is extremely versatile, since the microwave resonators used to confine the photons can be lithographically defined and the "atom" can be replaced by any two-level system that couples to light via a dipole coupling. This has enabled quantum computing and quantum optics experiments with electron spins in quantum dots [41–43], defect centers in solids [44, 45], electrons on helium [46], and many more exotic systems. However, circuit QED is probably most well known for its impact in the development of a superconducting quantum computer with the transmon qubit. A transmon qubit is a lithographically defined artificial atom which features a strong atom-photon coupling and a long coherence time. Currently, it has been adopted as one of the most promising systems for quantum computation.

No matter the type of "atom", in its simplest form each circuit QED system is described by the Jaynes-Cummings Hamiltonian, which consists of three parts:

$$H_{\text{JC}} = \hbar\omega_0 \left(a^\dagger a + \frac{1}{2} \right) + \frac{\hbar\omega_e}{2}\sigma_z + H_{\text{int}}. \tag{1.23}$$

The first part describes the microwave cavity with resonance frequency ω_0 and photon lowering operator a, the second part describes the two-level system with transition frequency ω_e and the last part describes the interaction between the cavity field and the two-level system. This interaction arises from the dipole energy $H_{\text{int}} = -\mathbf{d} \cdot \mathbf{E}$, where $\mathbf{d}$ is the electrical dipole moment and $\mathbf{E}$ is the microwave electric field at the location of the atom. The electric field

of single mode cavity scales with $(a + a^\dagger)$, which can be derived from second quantization of the harmonic oscillator [47]. In addition, $\mathbf{d}$ scales with the atomic raising and lowering operators $(\sigma_- + \sigma_+)$, resulting in

$$H_{\text{int}} = \hbar g \left(a + a^\dagger\right) (\sigma_- + \sigma_+) , \tag{1.24}$$

where we have grouped the prefactors into the coherent interaction rate g. We will see how to work out the coupling strength to electrons on helium in Section 1.3.1.

In the interaction picture the operators $a(t) = a(0)e^{-i\omega_0 t}$ and $a^\dagger(t) = a^\dagger(0)e^{i\omega_0 t}$ rotate rapidly at frequency ω_0, and $\sigma_\pm(t) = \sigma_\pm(t)e^{\pm i\omega_e t}$ rotate at frequency ω_e. Therefore,

$$H_{\text{int}} = \hbar g \left(a\sigma_- e^{-i(\omega_0+\omega_e)t} + a\sigma_+ e^{i(\omega_0-\omega_e)t} + a^\dagger\sigma_- e^{-i(\omega_0-\omega_e)t} + a^\dagger\sigma_+ e^{i(\omega_0+\omega_e)t}\right) \tag{1.25}$$

It is clear that in the so-called interaction picture the $a\sigma_-$ and $a^\dagger\sigma_+$ terms oscillate much faster than the other two terms. Since any dynamics in these terms averages out on the relevant timescale $1/(\omega_0 - \omega_e)$, we may safely drop these terms (i.e. rotating wave approximation), which leaves $a^\dagger\sigma_-$ and $a\sigma_+$. These terms describe the conversion of a cavity photon to an excitation of the two-level system and vice versa. Transforming back gives us the more familiar form of the Jaynes-Cummings Hamiltonian under the rotating wave approximation

$$H_{\text{JC}} = \hbar\omega_0 a^\dagger a + \frac{\hbar\omega_e}{2}\sigma_z + \hbar g \left(a^\dagger\sigma_- + a\sigma_+\right) . \tag{1.26}$$

Since the $a^\dagger\sigma_- + a\sigma_+$ term in H_{int} can cause transitions between the atom ground-excited states while emitting or absorbing a single cavity photon, it makes sense to express H_{JC} in the basis $\{|g, n+1\rangle, |e, n\rangle\}$, which yields

$$H_{\text{JC}} = \left(a^\dagger a + \frac{1}{2}\right)\hbar\omega_0 + \hbar \begin{pmatrix} -\frac{\Delta}{2} & g\sqrt{n+1} \\ g\sqrt{n+1} & \frac{\Delta}{2} \end{pmatrix} \tag{1.27}$$

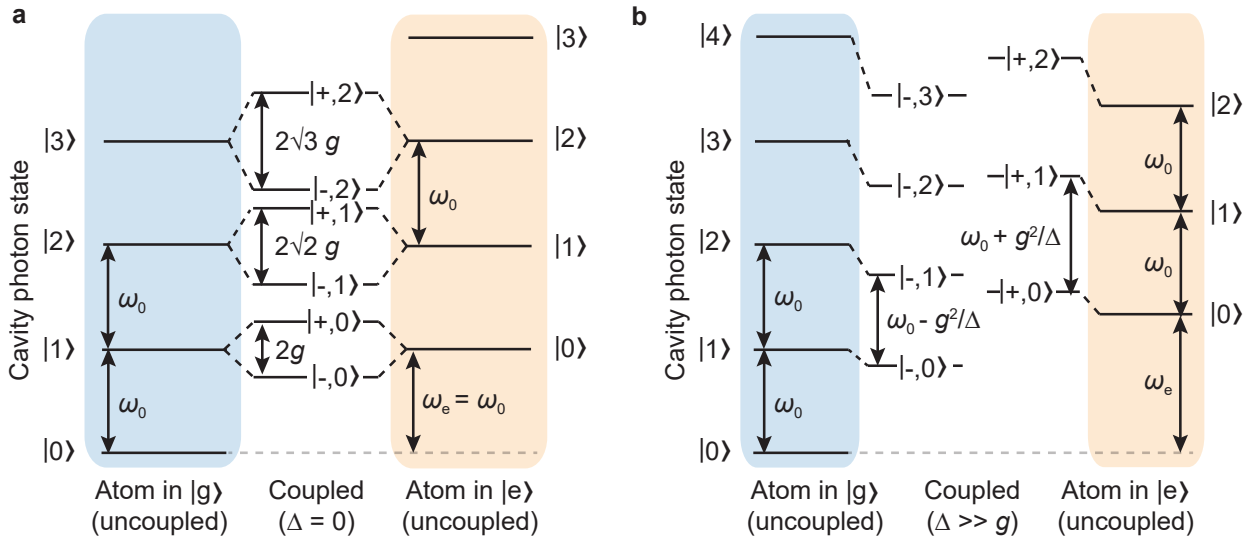

Figure 1.6: Spectrum of the Jaynes-Cummings Hamiltonian in two regimes. (a) In the resonant regime ($\Delta = 0$), the atom and cavity states fully hybridize to the dressed states $|\pm, n\rangle$, which are pairwise split by $2g\sqrt{n+1}$. (b) In the dispersive regime, where the atom stays far detuned from the cavity, the effect is a state-dependent cavity frequency shift. If the atom is in the ground (excited) state, the cavity frequency shift is pulled down (pushed up) by g^2/Δ. This feature forms the basis of non-destructive atom-state detection.

where $\Delta = \omega_0 - \omega_e$ is the cavity-atom detuning. In this form it is straightforward to calculate the eigenenergies for arbitrary g, Δ

$$E_n^{\pm} = \left(n + \frac{1}{2}\right)\hbar\omega_0 \pm \frac{1}{2}\sqrt{\Delta^2 + (2g\sqrt{n+1})^2} \tag{1.28}$$

The dynamics hidden inside H_{JC} depends sensitively on the energy scales of ω_0, ω_e and g. Therefore, before calculating the eigenstates, we distinguish two regimes based on the cavity-atom detuning $\Delta = \omega_0 - \omega_e$. For $\Delta = 0$ the energy to excite the atom is equal to the energy of a cavity photon, which causes the atom and cavity to fully hybridize as shown in Fig. 1.6a. On the other hand, for $\Delta \gg g$ the eigenstates and eigenenergies are only weakly modified, which is schematically depicted in Fig. 1.6b. We will now briefly highlight the main aspects of both regimes.

1.2.2 Resonant regime ($\Delta = 0$)

In the resonant case, the dressed states $|\pm, n\rangle$ correspond to coherent mixtures of cavity and photon states. As a result, an excitation in a dressed state spends an equal amount of time as a cavity photon and as atom excitation:

$$|+, n\rangle = \frac{1}{\sqrt{2}} \left(|g, n+1\rangle + |e, n\rangle \right) \tag{1.29}$$

$$|-, n\rangle = \frac{1}{\sqrt{2}} \left(|g, n+1\rangle - |e, n\rangle \right) \tag{1.30}$$

Setting $\Delta = 0$ in Eq. (1.28) gives us a simple spectrum corresponding to these eigenstates

$$E_n^{\pm} = \left(n + \frac{1}{2} \right) \hbar\omega_0 \pm \hbar g \sqrt{n+1}. \tag{1.31}$$

The $|+, n\rangle$ and $|-, n\rangle$ states are separated in frequency by $2g\sqrt{n+1}$, where $\Omega_0 = 2g$ is sometimes called the vacuum Rabi rate, because it is the rate at which energy is exchanged between an atom and a cavity populated with $n = 0$ photons. For an experimentalist, the splitting of the cavity peak in two distinguishable peaks separated by $2g\sqrt{n+1}$ is a hallmark of the Jaynes-Cummings Hamiltonian and provides a way to measure the coupling g.

1.2.3 Dispersive regime ($\Delta \gg g$)

In the dispersive regime the atom remains far detuned from the cavity, but still makes its imprint on cavity photons. Using perturbation theory one can show that H_{JC} is approximated by

$$H_{\mathrm{disp}} = \hbar \left(a^\dagger a + \frac{1}{2} \right) \left(\omega_0 + \frac{g^2}{\Delta} \sigma_z \right) + \frac{\hbar\omega_e}{2} \sigma_z. \tag{1.32}$$

The spectrum of this Hamiltonian shows that the cavity is weakly perturbed by the atom, changing the cavity frequency by g^2/Δ based on the state of the atom:

$$E_n^+ = n\hbar\left(\omega_0 + \frac{g^2}{\Delta}\right) + \frac{\omega_e}{2} \tag{1.33}$$

$$E_n^- = (n+1)\hbar\left(\omega_0 - \frac{g^2}{\Delta}\right) - \frac{\omega_e}{2} \tag{1.34}$$

E_n^+ and E_n^- are associated with an atom mostly in the excited and ground state, respectively. This can also be seen from the associated eigenstates, which are again only weakly perturbed from the uncoupled eigenstates $|g, n+1\rangle$ and $|e, n\rangle$

$$|+, n\rangle = \frac{g\sqrt{n+1}}{\Delta}|g, n+1\rangle + |e, n\rangle \tag{1.35}$$

$$|-, n\rangle = |g, n+1\rangle - \frac{g\sqrt{n+1}}{\Delta}|e, n\rangle \tag{1.36}$$

The fact that $|\pm, n\rangle$ are eigenstates of H_{disp} can be used to perform non-destructive atom read-out via the cavity. This is referred to as quantum non-demolition (QND) read-out and is widely used in today's version of the superconducting quantum computer.

1.2.4 Coupling to the environment: impact of decoherence

The physics we have discussed above is valid in the absence of a coupling to the environment, which one inevitably needs to transfer signals from the cavity to the measurement apparatus. If done improperly, unintended couplings to the environment can lead to decoherence and obscure the coherent effects. Common sources of decoherence in circuit QED can be split up two ways: those related to the microwave cavity and those related to the atom. The former are captured by the cavity decay rate $\kappa_{\text{tot}} = \kappa_c + \kappa_i$, which includes the effects of transparent input and output couplers (κ_c) and coupling to other microwave modes and absorption (κ_i). The atom's decoherence rate is $\gamma = \frac{\gamma_1}{2} + \gamma_\varphi$, which captures energy relaxation γ_1 and dephasing γ_φ.

The decoherence rate of the cavity and atom ought to be compared to the coherent interaction rate g. If $g \gg \gamma, \kappa_{\rm tot}$ the coupling rate dominates all loss rates in the system and coherent interactions involving single photons are observable[3]. In this strong coupling regime the characteristic dressed state splitting for $\Delta = 0$ is still intact. In contrast, if either $\kappa_{\rm tot}$ or γ exceeds g, coherent quantum effects are washed out quickly, including the dressed state splitting. The success of circuit QED with the superconducting transmon qubit has been propelled by extremely large coupling strengths $g/2\pi > 100$ MHz, combined with advancements in materials science that have pushed κ_i and γ to values below 10 kHz. In the next section we explore the potential of electrons on helium for integration with circuit QED and in particular, we discuss potential sources of decoherence that may prevent operation in the strong coupling regime.

1.3 Circuit quantum electrodynamics with the motional state of an electron on helium

A single electron can couple strongly to a single microwave photon, since the electron motional state has a small coupling to the helium substrate [9, 28] while we expect a relatively large coherent coupling g, due to a concentrated electric field mode and the large zero-point motion of a trapped electron. In this section we calculate the expected coupling strength and decoherence of a single electron on helium coupled to a microwave resonator.

1.3.1 Coupling to the lateral motion of a single electron on helium

A single electron on helium couples to a microwave resonator via the microwave electric field **E**. In the simplified LC-resonator shown in Fig. 1.7 all the electric field is concentrated in between the capacitor plates, and oscillates with frequency $\omega_0 = 1/\sqrt{LC}$. The electron

3. For any circuit QED system one can write down the cooperativity C to quantify the ratio of $\gamma, \kappa_{\rm tot}$ to g. For $C = g^2/(\kappa_{\rm tot}\gamma) \gg 1$, the system is usually in the strong coupling regime, whereas $C < 1$ represents an overdamped system.

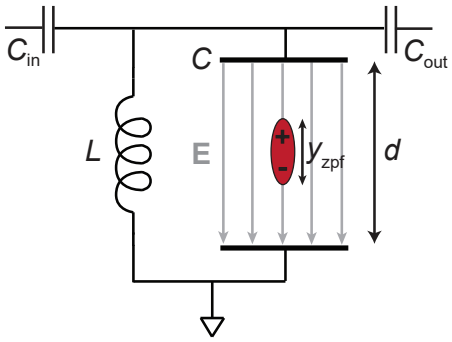

Figure 1.7: Schematic of the coupling mechanism of a single electron on helium to an LC microwave resonator. The microwave electric field E interacts with the oscillating electron represented by an electrical dipole (red). In the absence of a driving field, which can be applied through the coupling capacitor $C_{\rm in}$, the electron wavefunction has an extent (zero-point motion) of $y_{\rm zpf}$.

couples to the resonator, since it experiences a force $\mathbf{F}(t) = -e\mathbf{E}e^{i\omega_0 t}$, which drives an electron oscillation at frequency ω_0. We can also understand the origin of the electron-photon coupling from the viewpoint of the electron. In the absence of an electric driving field, the electron still fluctuates with amplitude $y_{\rm zpf}$, which changes the induced charge on the capacitor plates as the electron moves towards and away from the capacitor plates. This induced charge generates photons at the electron frequency ω_e.

To understand why the electron-photon coupling can be large even for a single electron on helium, we write the interaction energy as

$$H_{\rm int} = \hbar g = -\boldsymbol{d}\cdot\mathbf{E} = e y_{\rm zpf} E_y V_{\rm zpf}. \tag{1.37}$$

where $\boldsymbol{d} = -e y_{\rm zpf}\hat{\mathbf{y}}$ is the dipole moment, $y_{\rm zpf} = \sqrt{\hbar/2m_e\omega_e} \approx 30$ nm is the zero point motion of the electron in the $\hat{\mathbf{y}}$-direction, $E_{\rm y}$ is the electric field in the y-direction generated by 1 V potential difference across the capacitor and finally $V_{\rm zpf}$ is the amplitude of vacuum fluctuations across the capacitor. We see from Eq. (1.37) that g can be large, since the zero-point motion $y_{\rm zpf}$ is large due to the small electron mass m_e, and the electric field strength can be very concentrated in two-dimensional resonator geometries: $E_y \approx 1/d \approx 10^6$ V/m.

To estimate g, we determine $V_{\rm zpf}$ in Eq. (1.37) from the fact that on resonance half of

the cavity's zero point energy ($\hbar\omega_0/2$) is stored in the capacitor, such that

$$\frac{1}{4}\hbar\omega_0 = \frac{1}{2}\frac{1}{T}\int_0^T \mathrm{d}t\cos^2(\omega_0 t)\int \mathrm{d}^3 r\varepsilon E^2(r) = \frac{1}{4}CV_{\mathrm{zpf}}^2 = \frac{1}{2}CV_{\mathrm{rms}}^2. \tag{1.38}$$

This can be further simplified using the relations $\omega_0 = \sqrt{1/LC}$ and $Z = \sqrt{L/C}$, such that Eq. (1.38) yields $V_{\mathrm{rms}} = \omega_0\sqrt{\hbar Z/2}$. Therefore, the resonator impedance is an additional variable to enhance the coupling strength; by designing the resonator with a large inductance and small capacitance, one can achieve a larger coupling strength for the same resonance frequency. Plugging this in Eq. (1.37) gives

$$g/2\pi = \frac{1}{2}eE_y f_0\sqrt{\frac{Z}{m_e\omega_e}}. \tag{1.39}$$

For typical values of $E_y \approx 10^6$ V/m, $Z \approx 50\ \Omega$ and $f_0 = 6$ GHz we find $g/2\pi \approx 18$ MHz, which can be enhanced even further with a high-impedance resonator design [43, 48, 49].

1.3.2 Sources of decoherence for an electron-on-helium qubit

Microwave emission and absorption in two-dimensional microwave cavities has been studied extensively to the point where microwave cavities can routinely achieve internal quality factors $Q_i = \omega_0/\kappa_i$ over one million. Therefore, the total cavity loss rate $\kappa_{\mathrm{tot}} \approx \kappa_c \approx 2\pi \times 1$ MHz is set by the designed transparency of the output mirror (i.e. C_{out} in Fig. 1.7). The requirement $g > \kappa_{\mathrm{tot}}$ is therefore easily satisfied for circuit QED with an electron on helium. To satisfy the other condition for strong coupling ($g > \gamma$), we identify and quantify decoherence channels for a single electron on helium.

The dominant decay processes of an electron-on-helium orbital state are due to emission of ripplons on the surface of liquid helium and phonons inside the bulk liquid helium, as depicted in Fig. 1.8. The matrix elements that describe these processes for the vertical states are well-documented in Ref. [9], and form a good starting point for calculating similar

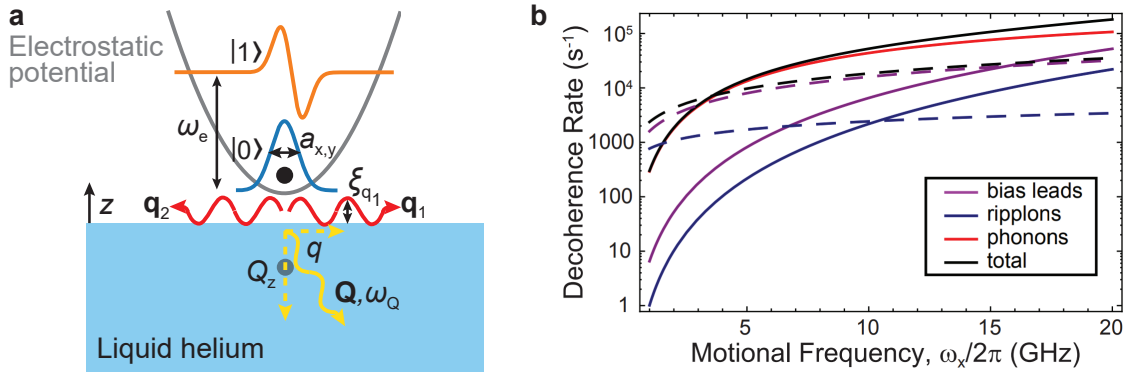

Figure 1.8: (a) Two decay processes of the electron-on-helium orbital state. An electron in its excited orbital state can decay via phonons or ripplons. The dominant phonon and ripplon decay processes are sketched in red and yellow, respectively. The dominant ripplon process is one where two ripplons with nearly opposite momentum each carry half the excitation of the motion $\hbar\omega_e$. The dominant phonon decay occurs due to modulation of the dielectric constant of the bulk helium. A phonon with total wavenumber $\mathbf{Q}$ and energy $\hbar\omega_Q$ is emitted nearly perpendicular to the surface. (b) Summary of decay $\gamma_1/2$ (solid lines) and dephasing γ_φ (dashed lines) processes due to phonons (red) and ripplons (blue) as function of the electron orbital frequency $\omega_e/2\pi$. Taken from Ref. [28].

rates for the motional state[4] We summarize the results of these calculations [28] below and in Fig. 1.8b.

Decay via ripplons

A single electron couples to helium surface waves (ripplons), since a curved surface (i) deforms the wavefunction of the vertical state (the vertical wavefunctions must remain zero at the helium interface) and (ii) changes the polarization energy [9]. A single ripplon can only interact with an electron if its wavelength $2\pi/q$ is approximately the electron localization length $a_x = (\hbar/m_e\omega_e)^{1/2}$. For longer wavelengths $q \gg a_x^{-1}$, the matrix element in Fermi's

4. Most of the assumptions made in Ref. [9] still hold, but instead of calculating transitions between different vertical states, we assume that the electron remains in the vertical ground state. For example, the matrix element $\langle 1_z|V_q|2_z\rangle$ becomes $\langle 1_z|V_q|1_z\rangle$, where $|1_z\rangle$ represents the vertical ground state labeled as $\chi_1(z)$ in Fig. 1.1.

golden rule decays exponentially with $q\,a_{x,y}$:

$$\Gamma_1^{(1r)} \propto \sum_q |\langle 0|e^{i\mathbf{q}\cdot\mathbf{r}}|1\rangle|^2 \propto e^{-(q^2a_x^2+q^2a_y^2)}. \tag{1.40}$$

For an electron-on-helium with $\omega_e/2\pi \approx 5$ GHz, the ripplon wavenumber $q \approx 10a_x^{-1}$, so decay via single ripplons does not play a significant role.

The dominant ripplon process emits two ripplons with nearly equal but opposite momenta $\mathbf{q}_1 \approx -\mathbf{q}_2$ (see Fig. 1.8a), which follows from the first term in Fermi's golden rule

$$\Gamma_1^{(2r)} = \frac{2\pi}{\hbar}\sum_{q_1,q_2} \underbrace{|\langle 0|\xi_{\mathbf{q}_1}\xi_{\mathbf{q}_2}e^{i(\mathbf{q}_1+\mathbf{q}_2)\cdot\mathbf{r}}|1\rangle|^2}_{\text{Two-ripplon emission}} \underbrace{\langle 1_z|V_{\mathbf{q}_1,\mathbf{q}_2}|1_z\rangle|^2}_{\text{Coupling matrix element}} \tag{1.41}$$
$$\underbrace{\delta(\hbar\omega_e - \hbar\omega_{\mathbf{q}_1} - \hbar\omega_{\mathbf{q}_2})}_{\text{Energy conservation}} \underbrace{\big(1+\bar{n}(\omega_{\mathbf{q}_1})+\bar{n}(\omega_{\mathbf{q}_2})\big)}_{\text{Thermal ripplon density of states}}$$

From similar arguments as in Eq. (1.40), this term peaks sharply around $\mathbf{q}_1 + \mathbf{q}_2 \approx 0$, such that two ripplons must be emitted in opposite directions and each carry $\hbar\omega_{\mathbf{q}_1} = \hbar\omega_{\mathbf{q}_2} = \omega_e/2$ of energy. The other terms in $\Gamma_1^{(2r)}$ represent energy conservation and reflect the density of states at ripplon frequency $\omega_{\mathbf{q}_{1,2}}$. After evaluating the integrals the decay rate amounts to $\Gamma_1^{(2r)} = 4.5 \times 10^2$ Hz at $\omega_e/2\pi = 5$ GHz.

Decay via phonons

An excitation of the orbital state can decay into a phonon inside the helium, either via the electron's coupling to surface deformations or via the modulation of the image charge. The former process involves similar coupling terms as single ripplon decay, and evaluates to approximately $\Gamma_1^{(\mathrm{ph,s})} = 1.8$ kHz. The modulation of the image charge causes a modulation of the helium density ρ and in turn causes a modulation of the dielectric constant $\delta\varepsilon_{\mathrm{He}} \approx (\varepsilon_{\mathrm{He}} - 1)\delta\rho/\rho$. Even though $\varepsilon_{\mathrm{He}} = 1.056$ is small, this process has the dominant phonon decay rate.

Phonons travel relatively slowly in liquid helium, with a speed of $c = 2.4 \times 10^2$ m/s. Therefore, the phonon wavenumber $Q = \omega_e/c$ is almost ten times larger than the in-plane momentum $q \approx a_x^{-1}$, which follows from momentum conservation. However, unlike ripplons phonons are not constrained to the surface. Therefore, phonons are emitted almost perpendicular to the surface as shown by the yellow arrow in Fig. 1.8a. The decay rate is given by

$$\Gamma_1^{(\mathrm{ph,m})} = \frac{2\pi}{\hbar} \sum_Q \underbrace{|\langle 0|\phi_{\mathbf{Q}} e^{i\mathbf{q}\cdot\mathbf{r}}|1\rangle|^2}_{\text{Single phonon emission}} \; |V_{\mathbf{Q}}|^2 \; \underbrace{\delta(\hbar\omega_e - \hbar\omega_Q)}_{\text{Energy conservation}} \;, \tag{1.42}$$

where $V_{\mathbf{Q}}$ is the expectation value of the electron-phonon coupling for the vertical ground state $|1_z\rangle$ and $\phi_{\mathbf{Q}} = (\hbar c/\rho V Q)^{1/2}$ is the phonon zero-point amplitude. This rate exceeds the contribution from phonon-induced surface displacement and evaluates to $\Gamma_1^{(\mathrm{ph,m})} = 2.7 \times 10^4$ Hz at $\omega_e/2\pi = 5$ GHz.

Electron dephasing

The electron dephases due to any process that changes the orbital frequency ω_e, but Ref. [28] predicts voltage noise on the bias electrodes as the main source of dephasing. The orbital frequency tunes with voltage according to $\omega_e \propto \sqrt{V}$, such that small changes in V cause a frequency shift

$$\Delta\omega = -\omega_e \frac{\Delta V}{2V}. \tag{1.43}$$

Johnson noise, with spectral density $S_V = \langle \Delta V^2 \rangle / \Delta f = k_B T \mathrm{Re}(Z)$, is very small at $T = 20$ mK and results in a negligible contribution to the linewidth:

$$\Gamma_\varphi^{(\mathrm{J})} = \left(\frac{\partial \omega_e}{\partial V}\right)^2 S_V = \frac{\omega^2 k_B T \mathrm{Re}(Z)}{4V_e^2} < 90\,\mathrm{Hz} \tag{1.44}$$

Besides Johnson noise, $1/f$-noise is another common noise source, originating from trapped charge carriers inside the substrate, for example. It can be estimated from typical values

measured in other experiments ($S_q(1\text{Hz}) \approx 10^{-4}$ e/$\sqrt{\text{Hz}}$) [28, 50] and leads to an estimated linewidth of $\Gamma_\varphi^{(1/f)} = 8 \times 10^3$ Hz.

Summary

The total expected decay rate for an electron on helium $\gamma_1 \approx \Gamma_1^{(2r)} + \Gamma_1^{(\text{ph,s})} + \Gamma_1^{(\text{ph,m})}$ is dominated by the phonon contribution $\Gamma_1^{(\text{ph,m})}$ (see Fig. 1.8b), and much smaller than the value of $g/2\pi = 18$ MHz we calculated in Section 1.3.1. The theoretical dephasing rate $\gamma_\varphi \approx \Gamma_\varphi^{(1/f)}$ seems limited by $1/f$-noise. From these estimates, we can conclude that circuit QED with electrons on helium in the strong coupling regime is possible.

1.3.3 Cavity input-output theory for a single electron on helium

We have already seen that in the resonant strong coupling regime, the spectrum of a cavity coupled to an electron splits into dressed states separated by $2g\sqrt{n+1}$. Experimentally, we reach the resonant regime by adjusting the electron frequency ω_e while monitoring the transmission through a two-sided microwave cavity. If we understand the cavity response for various ω_e, we may be able to deduce important parameters such as g, κ_{tot} and γ, even in the weak coupling regime. The input-output formalism of quantum optics [51] provides a powerful description of a cavity subject to a drive tone. Below, we follow the approach of Refs. [52, 53] and show how we deduce circuit QED parameters from the spectrum of the cavity output field.

The Hamiltonian of a resonator coupled to a two-level system, in the frame rotating with a drive tone at frequency ω_d is

$$H_d/\hbar = (\omega_0 - \omega_d)a^\dagger a + (\omega_e - \omega_d)\frac{\sigma_z}{2} + g(\sigma_- a^\dagger + \sigma_+ a) + \epsilon(a + a^\dagger), \tag{1.45}$$

where ω_0 is the cavity frequency, ω_e is the electron frequency, $\sigma_{+,-}$ are the electron raising and lowering operators and ϵ is the drive strength expressed in units of s^{-1}. The unitary

dynamics of the cavity photons and trapped electron is governed by the Heisenberg equations for a and σ_-, respectively. For the operator a, this equation yields

$$\dot{a} = \frac{i}{\hbar}[H_d, a] = i(\omega_0 - \omega_d)[a^\dagger a, a] + i\left(g\sigma_- + \epsilon\right)[a^\dagger, a]. \tag{1.46}$$

Using the bosonic commutation relations $[a, a^\dagger] = 1$, we find $[a^\dagger a, a] = -a$, such that

$$\dot{a} = -i(\omega_0 - \omega_d)a + -i\left(g\sigma_- + \epsilon\right) = -i\Delta_{cd}a - ig\sigma_- - i\epsilon, \tag{1.47}$$

where $\Delta_{cd} = \omega_0 - \omega_d$ is the cavity-drive detuning. We can now follow the same procedure for the electron lowering operator σ_-:

$$\dot{\sigma}_- = \frac{i}{2}(\omega_e - \omega_d)[\sigma_z, \sigma_-] + ig[\sigma_+, \sigma_-]a, \tag{1.48}$$

where we must use the proper commutators for the Pauli matrices $[\sigma_z, \sigma_-] = -2\sigma_-$ and $[\sigma_+, \sigma_-] = \frac{i}{2}[\sigma_y, \sigma_x] = \sigma_z$. With the electron-drive detuning defined as $\Delta = \omega_e - \omega_d$ the equation of motion for σ_- reads

$$\dot{\sigma}_- = i\Delta\sigma_- + ig\sigma_z a. \tag{1.49}$$

We can now add dissipation to both the cavity and electron. Loss from the cavity happens at rate $\kappa_{\text{tot}} = \kappa_1 + \kappa_2 + \kappa_{\text{int}}$, where κ_1 and κ_2 represent leakage through the imperfect mirrors of the cavity, and κ_{int} covers microwave absorption inside the cavity. Additionally, we may add electron loss using the term $-\gamma\sigma_-$, such that Eqs. (1.47) and (1.49) become

$$\dot{a} = -\left(\frac{\kappa_{\text{tot}}}{2} + i\Delta_{cd}\right)a - ig\sigma_- - i\epsilon \tag{1.50}$$

$$\dot{\sigma}_- = -\left(\gamma + i\Delta\right)\sigma_- + ig\sigma_z a \tag{1.51}$$

An experimentalist can only observe expectation values of operators, and let us for now

neglect fast transients in these expectation values. The steady-state equations for the cavity field $\langle a \rangle$ and electron lowering operator $\langle \sigma_- \rangle$ are

$$\left(\frac{\kappa_{\text{tot}}}{2} + i\Delta_{cd}\right)\langle a \rangle - ig\langle \sigma_- \rangle - i\epsilon = 0 \tag{1.52}$$

$$-\left(\gamma + i\Delta\right)\langle \sigma_- \rangle + ig\langle \sigma_z a \rangle = 0 \tag{1.53}$$

These equations are mostly linear, except for the correlator $\langle \sigma_z a \rangle$. For a classical drive with many photons ($\langle a \rangle \gg 1$), quantum correlations between photon and electron can be safely ignored [53] such that we can approximate this correlator as $\langle \sigma_z a \rangle \approx \langle \sigma_z \rangle \langle a \rangle$. Solving for the intra-cavity field $\langle a \rangle$ gives

$$\langle a(\omega_d) \rangle = \frac{-i\epsilon}{i\Delta_{cd} + \kappa_{\text{tot}}/2 - g^2\langle \sigma_z \rangle / \left(\gamma + i\Delta\right)} \tag{1.54}$$

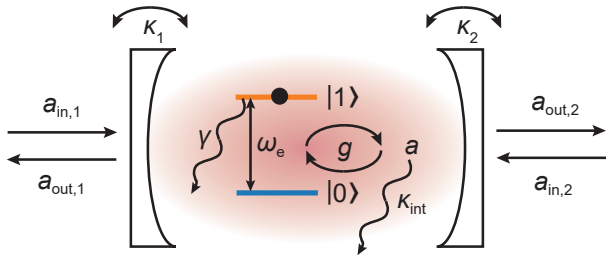

Figure 1.9: Input-output theory for a cavity coupled to a single electron. Schematic of the cavity with inputs $a_{\text{in},1}$, $a_{\text{in},2}$ and output fields $a_{\text{out},1}$ and $a_{\text{out},2}$. The intra-cavity field is denoted with a and depends on the state of the electron and the input and output fields.

Eq. (1.54) gives a description of the field amplitude inside the cavity with a coherent microwave drive ϵ, which can be used to calculate the number of intra-cavity photons n_{ph}, for example. However, the only way to probe the intra-cavity field is via reflection or transmission of external probe fields. Using input-output theory we define an expression for the transmission through a two-sided cavity (schematically depicted in Fig. 1.9):

$$S_{21}(\omega_d) = \frac{a_{\text{out},2}(\omega_d)}{a_{\text{in},1}(\omega_d)}, \tag{1.55}$$

where $a_{\text{out},2}(\omega_d)$ is the field amplitude at port 2 (output) of the cavity and $a_{\text{in},1}(\omega_d)$ is the input field amplitude at port 1 of the cavity. Input-output theory gives us the relations between the input, output and the intra-cavity field at both ports

$$a_{\text{out},2}(\omega_d) = \sqrt{\kappa_2}\langle a(\omega_d)\rangle \tag{1.56}$$

$$a_{\text{in},1}(\omega_d) + a_{\text{out},1}(\omega_d) = \sqrt{\kappa_1}\langle a(\omega_d)\rangle, \tag{1.57}$$

which are valid in the absence of a cavity drive at port 2 ($a_{\text{in},2}(\omega_d) = 0$). Finally, using $\epsilon = i\sqrt{\kappa_1}a_{\text{in},1}(\omega_d)$, we arrive at the expression for the transmission through the cavity:

$$S_{21} = \frac{\sqrt{\kappa_1\kappa_2}}{i(\omega_0 - \omega_d) + \kappa_{\text{tot}}/2 + ig^2\langle\sigma_z\rangle/\left(\Delta - i\gamma\right)} = \frac{\sqrt{\kappa_1\kappa_2}}{i(\omega_0 - \omega_d) + \kappa_{\text{tot}}/2 + i\chi(\omega_e)}. \tag{1.58}$$

$\chi(\omega_e)$ is known as the susceptibility and describes the electron interaction with the resonator, through the coupling strength g and linewidth γ. The top row of Fig. 1.10 depicts three cavity transmission spectra as function of the electron frequency $f_e = \omega_e/2\pi$, and shows that if the electron is far off-resonant $\chi(\omega_e) = 0$, and the transmission reduces to the familiar Lorentzian cavity response

$$|S_{21}|^2 = \frac{\kappa_1\kappa_2}{(\omega_0 - \omega_d)^2 + \left(\kappa_{\text{tot}}/2\right)^2}. \tag{1.59}$$

If the electron is resonant with the cavity ($f_e = f_0$), the transmission depends strongly on the coupling strength and electron linewidth. In the strong coupling regime, $g > \gamma, \kappa_{\text{tot}}$, the transmission $|S_{21}|$ shows two peaks separated by twice the coupling strength, as expected from section 1.2.2. In the opposite case, $\gamma > g, \kappa_{\text{tot}}$, the electron still changes the transmission spectrum significantly, as shown by the Lorentzian of reduced peak amplitude, but the characteristic double peak splitting has disappeared.

The double peak splitting shown in Fig. 1.10 is a tell-tale sign of strong electron-photon coupling, and it has been used to claim strong coupling of photons to transmon qubits [54],

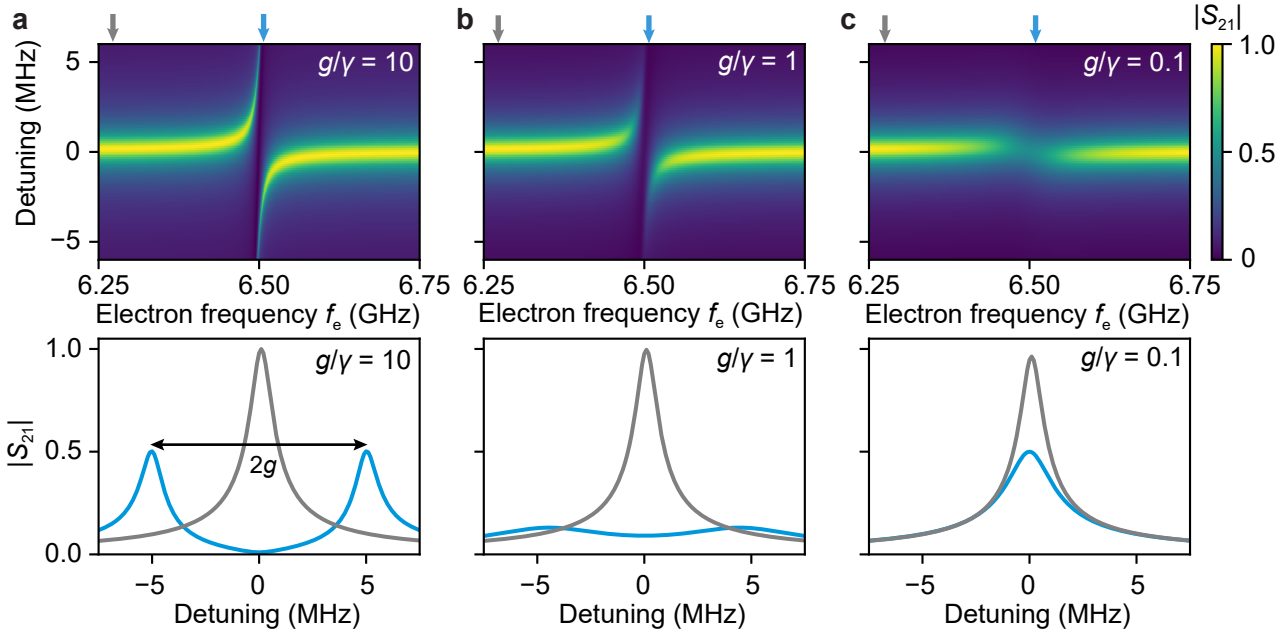

Figure 1.10: Simulated resonator transmission spectra as function of the electron frequency for different cavity QED parameters g/γ. The bottom row shows spectra on resonance ($f_e \approx f_0 = 6.5$ GHz blue) and off resonance ($f_e \ll f_0$, gray). For all curves the resonator transmission $|S_{21}|$ changes significantly when the electron frequency f_e approaches the resonance frequency. The other cavity QED parameters were chosen according to our best estimates for a single electron on helium: $g/2\pi = 5.0$ MHz and $\kappa_{\text{tot}}/2\pi = 0.5$ MHz. In the different columns we explore the effect of increasing decoherence on the resonator spectra, where in (a) $\gamma/2\pi = 0.5$ MHz, (b) $\gamma/2\pi = 5$ MHz and (c) $\gamma/2\pi = 50$ MHz.

electrons in a double quantum dot [49, 55], and more recently also an ensemble of electrons on helium [56]. Observation of this double peak splitting for the orbital state of a single electron on helium is one of the outstanding goals for the field of electrons on helium, and for the experiments presented in this thesis.

1.4 Goal of this thesis

The previous sections have described the remarkable properties of electrons on helium, and shown their potential as building blocks of an electron-on-helium quantum computer. The motion of electrons parallel to the helium surface shows particular promise, since its frequency is in the microwave regime and it can couple strongly to a microwave resonator, forming a circuit QED system in the strong coupling regime. In the strong coupling regime, coherent manipulation of the electron motion becomes possible and existing techniques developed for superconducting quantum computers can be applied to an electron-on-helium qubit.

A circuit QED system with few electrons on helium is also a great platform to study the quantized motion of Wigner molecules. Measurement of the mode spectrum of Wigner molecules may deepen our understanding of their internal structure and can be compared against many theoretical models. Finally, such a system may shed light on the Wigner molecule melting transition and the role of quantum fluctuations.

The goal of this thesis is to construct a circuit QED platform with the orbital state of few electrons on helium, that allows us to address an orbital state electron-on-helium qubit and explore strongly correlated electron physics. In order to do this, we must be able to confine single electrons in an electrostatic trap and couple their motion to a microwave resonator. In Chapter 2, we present the design of an electron-on-helium quantum dot, integrated with a superconducting microwave resonator. This device is designed to work at temperatures near absolute zero, where the quantum effects of the electron, single photons and the liquid helium should be visible. In Chapter 3 we discuss the experimental setup needed to supply superfluid helium to the sample cell, and the equipment that is used to perform low-noise

microwave measurements to detect the electron motion.

Our first measurements of Wigner molecules and of a single electron are presented in Chapter 4, where we load the dot with single electron precision and observe Wigner molecule spectra. With a single electron in the dot, we carefully characterize our circuit QED system to retrieve the coupling strength and electron linewidth. As will become clear, these measurements beg for a more thorough understanding and control of the helium substrate, which we attempt in Chapter 5. We conclude this thesis with an outlook that discusses several paths to reach the strong coupling regime with the electron orbital state, which should leave the reader with an optimistic view of the future of circuit QED with electrons on helium.

CHAPTER 2

DESIGN OF AN ELECTRON-ON-HELIUM DOT

2.1 General strategy for trapping a single electron

Controlling the quantized states of a single electron on helium requires an electrostatic island (i.e. dot) to reliably isolate and trap a single electron. Experimentally, electrons are produced by thermal emission from a tungsten filament, but since this is a violent process which releases many electrons, it is difficult to charge the dot with a single electron via thermal emission. After thermal emission we usually end up with a large electron ensemble containing thousands or millions of electrons. To isolate single electrons from such an ensemble we draw inspiration from semiconducting quantum dots, where appropriately shaped electrodes create electron depletion regions which serve as quantum dots that allow for single electron trapping.

In our approach, we choose to store the electron ensemble on top of a microwave cavity. While electrons on helium can be trapped on top of any electrode with a DC voltage, storing an ensemble above the microwave resonator allows us to detect their presence, retrieve the number of electrons in the ensemble, the collective electron motion frequency and the ensemble coupling from the measured resonance frequency shift [57]. Therefore, our resonator will serve two roles, as electron detector and as a home to the electron reservoir.

This chapter first deals with the design of the microwave resonator (section 2.2), which determines the microwave properties (e.g. resonance frequency, characteristic impedance) as well as the behavior of the electron reservoir. From there, we discuss the design of our electron-on-helium dot (section 2.3); an electrostatic island that can only hold a few electrons and where we hope to observe the Wigner molecule physics of chapter 1. Finally, we discuss the integration of this dot with the microwave resonator, which allows us to detect the microwave response of Wigner molecules.

2.2 Design of the resonator

The microwave resonator is an indispensable part of circuit QED, and in our system it serves both as an electron detector and as home to an electron-on-helium reservoir. Resonator design plays an important role in the sensitivity of our electron detector and determines the behavior of the electron reservoir. Maximizing the electron sensitivity, requires a large characteristic impedance, strong transverse microwave electric field and a high resonator quality factor. In addition, trapping an electron reservoir above the microwave resonator requires a DC bias voltage on the resonator center pin. Fulfilling this requirement while maintaining a high resonator quality factor is a challenge.

In this Section, we introduce a resonator design with two center pins capable of detecting single electrons and a single row of electrons. We derive the most important properties of such a resonator and consider the behavior of the reservoir electrons based on the electrostatic potential above the resonator.

2.2.1 Resonator microwave properties

To couple to the orbital electron state we use a superconducting microwave resonator consisting of two center pins surrounded by a ground plane. This geometry, also known as a coplanar stripline geometry (Fig. 2.1) supports two types of microwave modes. For the mode of interest, the pins carry an equal but opposite microwave potential at any point along the cross section. Therefore, the microwave electric field is concentrated in between the center pins, such that in principle it can couple strongly to the lateral motion of a single electron or a single row of electrons floating above the resonator.

The resonator center pins are situated approximately 1.2 µm below the ground plane, at the bottom of a 3.5 µm-wide channel. The micro-channel stabilizes the liquid helium surface due to surface tension, and allows for storing higher electron density reservoirs [58]. Without this channel, the electron reservoir would be much more sensitive to external vibrations, so

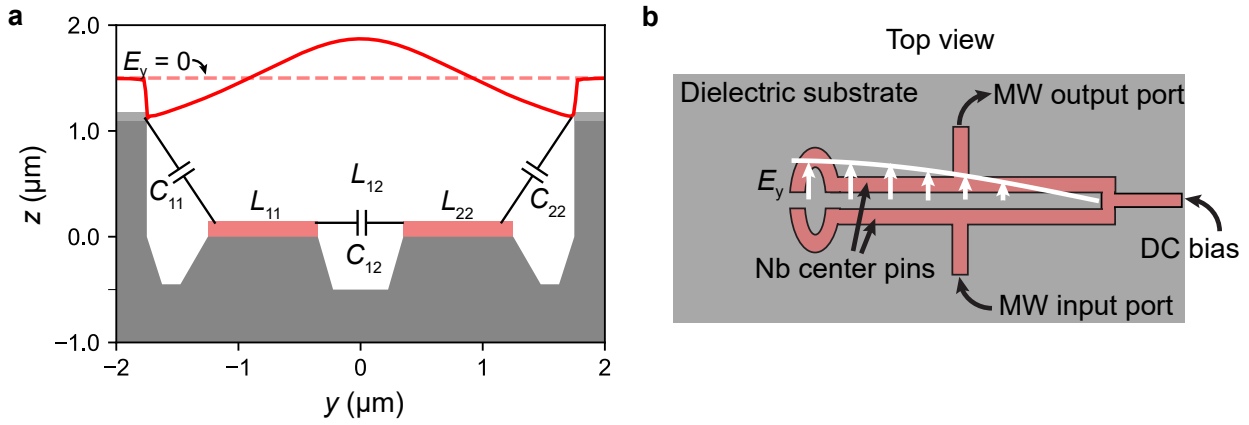

Figure 2.1: (a) Schematic representation of the capacitances C_{ij} and inductances L_{ij} involved in a differential pair with two Nb center pins (red) and a ground plane (gray) on a Si substrate (dark gray). The microwave electric field E_y (red) is evaluated at the helium filling height $z = 1.2$ μm and a dashed line indicates $E_y = 0$. (b) Top view of the microwave resonator design, showing the two center pins and the transverse microwave electric field E_y of the differential mode. A DC bias voltage is applied at the location of a voltage node ($E_y = 0$), such that photon loss through the DC bias port is minimal.

it is a crucial feature of our design.

The most essential microwave properties, e.g. the impedance Z and resonance frequency f_0, can be extracted from the capacitances and inductances from Fig. 2.1a. The inductances and capacitances can be written in a matrix as follows:

$$\mathcal{L} = \begin{pmatrix} L_{11} & L_{12} \\ L_{21} & L_{22} \end{pmatrix} \quad \text{and} \quad \mathcal{C} = \begin{pmatrix} C_{11} & C_{12} \\ C_{21} & C_{22} \end{pmatrix}, \tag{2.1}$$

where diagonal elements represent self-inductance and capacitance to ground, and off-diagonal elements represent mutual inductance and capacitance. Given our model geometry, each of the entries can be simulated using a finite element simulation package (e.g. Ansys Electronics Desktop) by adding a positive excitation to the left pin and an equally negative excitation to the right pin. We obtain the following values: $L_{11} = 515$ nH/m, $L_{12} = 199$ nH/m, $C_{11} = 103$ pF/m and $C_{12} = 166$ pF/m. The impedance of the microwave differential mode

is given by

$$Z_{\text{diff}} = 2\sqrt{\frac{L_{11} - L_{12}}{C_{11} + |C_{12}|}}. \tag{2.2}$$

Without kinetic inductance we estimate the characteristic impedance $Z_{\text{diff}} \approx 90\,\Omega$. Additionally, we find an expression for the expected resonance frequency for the quarter wavelength differential mode:

$$f_0^{\text{diff}} = \frac{1}{4\ell} \frac{1}{\sqrt{(L_{11} - L_{12})(C_{11} + |C_{12}|)}}, \tag{2.3}$$

where ℓ is the length of the resonator measured from the tip to the point where the two center pins meet.

The other supported mode in a coplanar stripline geometry is a common mode, where the center pins carry an equal microwave potential. The microwave properties of the common mode are as follows

$$Z_{\text{comm}} = \sqrt{\frac{L_{11} + L_{12}}{C_{11} - |C_{12}|}} \tag{2.4}$$

$$f_0^{\text{comm}} = \frac{1}{4\ell} \frac{1}{\sqrt{(L_{11} + L_{12})(C_{11} - |C_{12}|)}} \tag{2.5}$$

For the common mode, the microwave electric field approximately cancels between the center pins, making it not suitable for coupling to single electrons. Typically, the resonance frequency f_0^{diff} is sufficiently different from f_0^{comm}, such that we can safely ignore the common mode, and Eqs. (2.3) and (2.5) provide a way to distinguish the common and differential modes in our experiment.

Trapping an electron ensemble above the resonator requires a DC bias voltage. Connecting a DC bias lead to the center pins of the resonator introduces a source of loss for intracavity photons, since the impedance of the bias leads is small ($Z \approx 50\ \Omega$). To minimize this loss and maintain a high resonator quality factor, we attach the bias lead at a voltage

node, as shown in Fig. 2.1b. Our design allows for loaded quality factors exceeding 2×10^4, which demonstrates the low photon loss rate through the DC bias port.

2.2.2 Considerations for the electron reservoir

Electrons floating above the resonator induce image charges in the resonator center pins below the helium surface and as such, the resonator and reservoir can be thought of as a parallel plate capacitor. The capacitance is given by

$$C = \frac{Q}{V_{\text{res}}} = \frac{Ne}{V_{\text{res}}}, \tag{2.6}$$

where V_{res} is the applied bias voltage to the resonator center pin and N is the number of reservoir electrons. If the electrons float a distance t_{He} above the resonator, we have the following equality

$$C = \frac{Ne}{V_{\text{res}}} = \frac{\varepsilon_0 \varepsilon_{\text{He}} A}{t_{\text{He}}}. \tag{2.7}$$

Eq. (2.7) shows that the electron density $n_s = N/A$ varies smoothly with the applied voltage according to

$$n_s = \frac{\varepsilon_0 \varepsilon_{\text{He}} V_{\text{res}}}{e t_{\text{He}}}. \tag{2.8}$$

The parallel plate capacitor model of the electron reservoir provides a simple estimate of the reservoir electron density as function of the resonator voltage. However, approximating the electron density as a continuous variable neglects that electrons are discrete particles, which becomes important for electrons in and near the dot. A more sophisticated model, also required to accurately describe the electron interaction with the cavity, takes into account the electrostatic potential generated by the DC voltage on the resonator center pins. At a distance t_{He} above the center pins it takes on the form

$$V(x, y) = (\alpha_0 + \alpha_1 y^2 + \alpha_2 y^4) V_{\text{res}}, \tag{2.9}$$

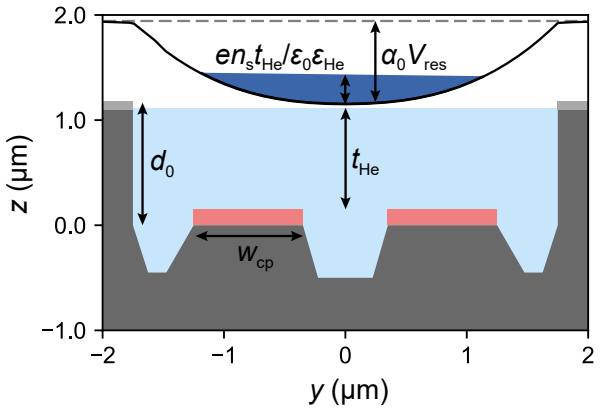

Figure 2.2: The electrostatic potential (black) produced by two electrodes on the bottom of a micro-channel (red) can trap an electron reservoir (dark blue). The maximum electron density depends on the trap depth $\alpha_0 V_{\text{res}}$.

where the dimensionless constant α_0 determines the trap depth, α_1 determines the trap curvature (units: m^{-2}) and α_2 contains an anharmonic component (units: m^{-4}). The relative magnitude and sign of α_2 compared to α_1, depend on the parameters d_0 and w_{cp} (Fig. 2.2), determine if the electrostatic potential has a double or single well and greatly affect how electrons spread across the channel. For the design shown in Fig. 2.2, α_2 and α_1 have the same sign, the potential has a single minimum and therefore, electrons can arrange into a single file along the channel at low electron densities (Fig. 2.3c). This facilitates the process of isolating electrons from the reservoir [59].

Reservoir electrons cause a frequency shift that depends on the frequency of the collective electron motion parallel to the helium surface. The eigenfrequencies of the ensemble depend on the equilibrium positions of the electrons and the potential curvature. We can find the equilibrium positions by minimizing the total energy of the electron ensemble

$$H = \sum_i \frac{p_i^2}{2m_e} + \sum_i eV(x_i, y_i) + \sum_{i<j} \frac{e^2}{4\pi\varepsilon_0 |\mathbf{r}_i - \mathbf{r}_j|}, \tag{2.10}$$

where the sum runs over the electrons in the reservoir. This minimization is typically performed by molecular dynamics simulations, a method that solves Newton's equations of

motion at finite temperature. By repeatedly minimizing H for decreasing temperature (a process called annealing) molecular dynamics finds a close approximation to the true ground state of the electron ensemble. A poor man's version neglects the kinetic component in Eq. (2.10) and to first order gives similar results at $T = 0$ K. The advantage is that the total energy can now be minimized rather quickly since the gradients can be calculated analytically. A result of the minimization procedure implemented in Python is shown in Fig. 2.3b.

With the electron positions at hand, the collective mode frequencies can be calculated via the eigenvalue equation

$$\mathcal{M}^{-1}\mathcal{K}|\eta_i\rangle = \omega_i^2|\eta_i\rangle, \tag{2.11}$$

where $\mathcal{M}$ and $\mathcal{K}$ are the mass and kinetic energy matrix and $\omega_i/2\pi$ is the eigenfrequency corresponding to eigenmode $|\eta_i\rangle$ [57]. These equations contain the electron positions, the curvature of the electrostatic trap (α_1) as well as the charge on the resonator, and fully describe the interaction between the resonator and ensemble in a non-perturbative fashion.

The minimum eigenfrequency $\omega_{i,\mathrm{min}}$ corresponds to the mode where all electrons move in concert, and is given by

$$\omega_{i,\mathrm{min}} = \sqrt{\frac{2e\alpha_1 V_{\mathrm{res}}}{m_e}}. \tag{2.12}$$

Other modes contain electron interaction terms involving $\sum_{i<j} e^2/4\pi\varepsilon_0|\mathbf{r}_i - \mathbf{r}_j|$ which act as an increased spring constant and therefore have higher mode frequencies.

The electrostatic potential produced by the resonator center pins should be designed such that the minimum collective mode frequency $\omega_{i,\mathrm{min}}$ greatly exceeds the microwave resonator frequency ω_0. Otherwise, if $\omega_{i,\mathrm{min}} \approx \omega_0$, a single trapped electron can decay via the electron reservoir mode, thereby increasing the electron linewidth γ. This phenomenon is also known as the Purcell effect. If the reservoir remains sufficiently far detuned from the resonance frequency f_0, we can consider the electron motion in the dot and reservoir separately, which simplifies modeling. Additionally, according to section 1.2.3 we can write down a simple,

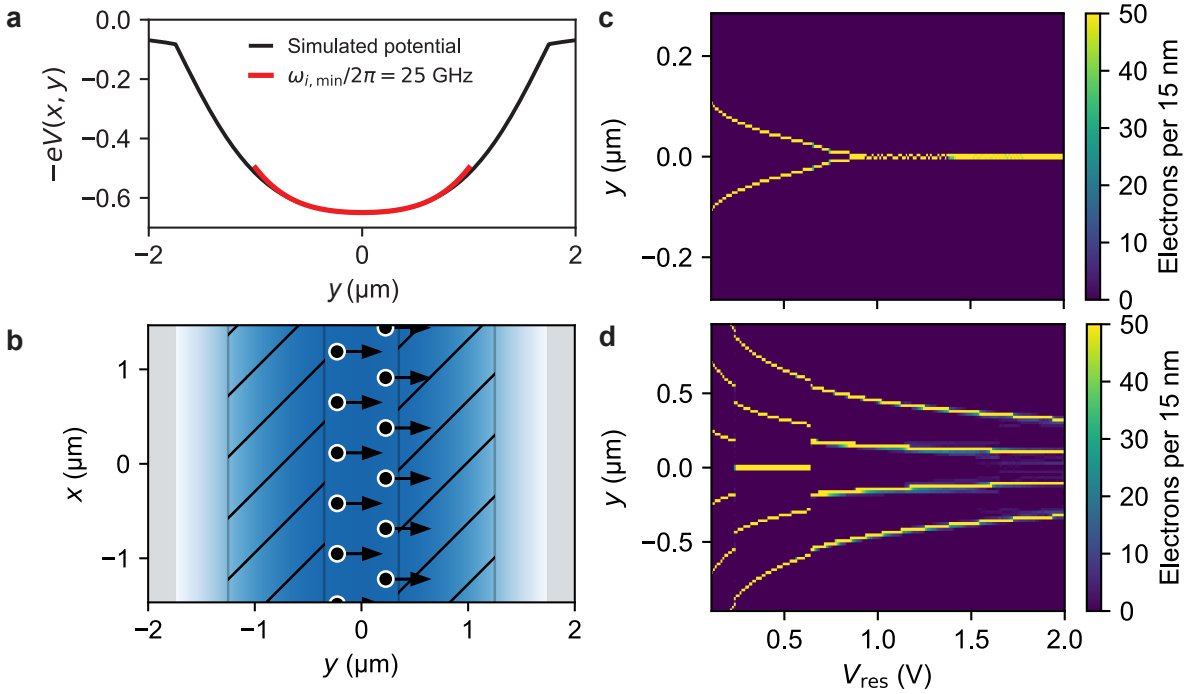

Figure 2.3: (a) Simulated electrostatic potential evaluated $t_{\mathrm{He}} = 1.1$ μm above the center pins. The voltage at the center pins was $V_{\mathrm{res}} = 1.0$ V and the curvature of the potential gives rise to a minimum ensemble frequency of $\omega_{i,\mathrm{min}}/2\pi = 25$ GHz, which is expected to scale with $\sqrt{V_{\mathrm{res}}}$. (b) Result of the reservoir electron minimization for a small number of electrons N and low V_{res}. Electrons (black dots) are located in the center of the micro-channel, near the minimum of the electrostatic potential (shades of blue). For the eigenmode $|\eta_i\rangle$ that couples strongest to the cavity, all electrons oscillate in concert, as depicted by the black arrows. (c)-(d) Electron histograms for the reservoir electron positions across the channel, for two different number of electrons N. (c) Number of electrons: 120 electrons / 40 μm resonator length (d) 600 electrons / 40 μm resonator length. Both histograms show that at large V_{res} the ensemble is more confined, resulting in fewer electron rows along the micro-channel. As the voltage decreases, the ensemble spreads across the channel and it becomes energetically more favorable to arrange into multiple rows. These simulations are consistent with earlier work [57, 60].

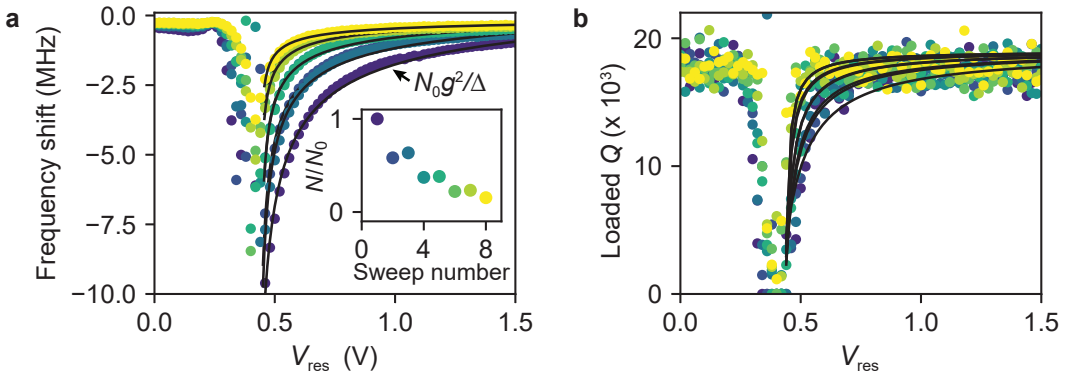

Figure 2.4: Measurements of the cavity resonance frequency shift due to an electron reservoir with varying number of electrons N. N decreases by repeatedly sweeping V_{res} to -1.5 V. (a) The cavity frequency shift follows the approximated form of Eq. (2.13) and decreases in magnitude as electrons leave the reservoir after each sweep to $V_{\mathrm{res}} = -1.5$ V (inset). (b) The cavity quality factor decreases rapidly as the ensemble mode frequency approaches the microwave resonance frequency. This behavior is also in accordance with a model that predicts $Q^{-1} = Q_L^{-1} + \kappa_\gamma/f_0$, where $Q_L \approx 2 \times 10^4$ is the loaded quality factor in the absence of electrons and κ_γ is given by Eq. (2.14).

approximate expression for the cavity frequency shift due to the electron ensemble :

$$\Delta f_0 \approx \frac{Ng^2}{\omega_{\mathrm{ens}} - \omega_0}, \tag{2.13}$$

where g and ω_{ens} are the eigenfrequency and coupling strength of the mode that couples strongest to the cavity.

Fig. 2.4a confirms that the measured cavity frequency shift is proportional to the number of electrons in the reservoir N, and shows that N can be controlled by repeatedly sweeping the resonator bias voltage negative. The dip in quality factor at $V_{\mathrm{res}} \approx 0.4$ V (Fig. 2.4b) occurs due to a broadening of the linewidth as ω_{ens} approaches ω_0

$$\kappa_\gamma = \frac{Ng^2}{(\omega_{\mathrm{ens}} - \omega_0)^2}\kappa, \tag{2.14}$$

and restricts the usable bias voltage to values larger than $V_{\mathrm{res}} > 0.6$ V. To summarize, Fig. 2.4 demonstrates that the coplanar stripline resonator can harbor an electron reservoir with variable electron density, and for voltages above $V_{\mathrm{res}} > 0.6$ the ensemble mode frequency

stays sufficiently far detuned from the resonator to avoid a negative impact on the single electron coherence time.

2.3 Design of the dot

The dot's main purpose is to trap a small number of electrons and isolate them from the electron reservoir on top of the resonator. This requires a number of additional electrodes to carefully craft the electrostatic potential.

We show a dot design that allows for trapping of single electrons and Wigner molecules in Fig. 2.5. The dot's electrostatic potential in the oblong-shaped region is determined by the voltages on the resonator guard, trap guard, resonator and trap electrodes. A negative voltage on either the resonator guard or trap guard raises a barrier around the dot. Therefore, the primary function of these electrodes is to control electron transport to and from the dot, and to contain electrons in the dot. The other two electrodes (resonator and trap electrode) control the trap frequency and the minimum value of the electrostatic potential in and around the dot.

2.3.1 Trap depth

To trap a single electron, the trap depth, defined as the energy difference between the smallest energy barrier and the potential minimum, must be larger than other classical disturbances or electron energies. Since a single electron minimizes its energy when it is located at the potential minimum, the barrier should be larger than thermal excitations ($k_B T \approx 2$ µeV), Johnson noise on the electrodes ($\sqrt{k_B T Z \Delta f} < 1$ µeV) and the electron's zero-point motion ($\hbar\omega_e/2 \approx 25$ µeV). Therefore, the electrostatic trap must be at least 100 µeV deep to confine a single electron.

With more than one electron in the dot, the largest energy scale is set by the Coulomb interaction and reaches $e^2/4\pi\varepsilon_0 r \approx 0.7$ meV for two electrons with $r = 0.2$ µm. Larger

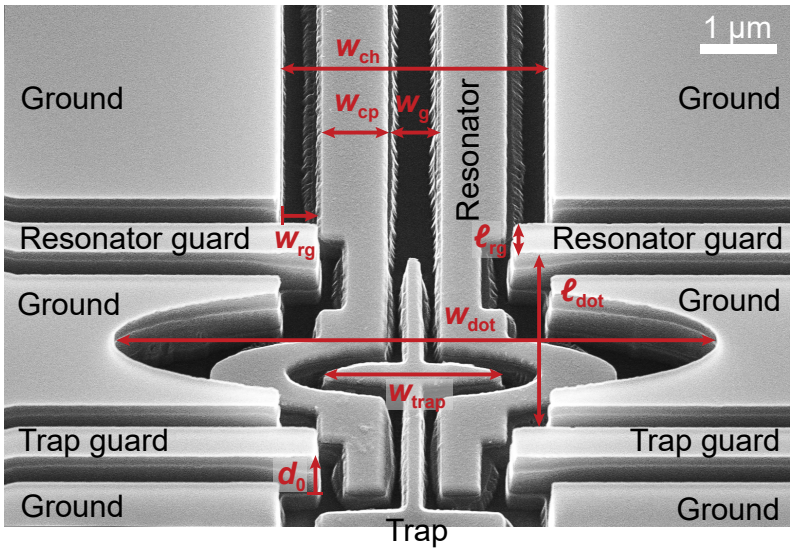

Figure 2.5: Tilted angle scanning electron micrograph of the dot with the relevant dimensions shown in red. A single electron can be trapped in the center of the dot, which consists of the oblong-shaped region, bounded by the resonator guards, trap guards and ground plane. The dot is fabricated by micro-machining a silicon substrate (black, details about the process in Appendix A) and by depositing superconducting electrodes (gray). The resonator electrode dimensions are $w_{\rm ch} = 3.5$ μm, $w_{\rm cp} = 0.9$ μm, $d_0 = 1.2$ μm and $w_g = 0.5$ μm. The dot dimensions are $w_{\rm rg} = 0.3$ μm, $\ell_{\rm rg} = 0.4$ μm, $(w_{\rm dot}, \ell_{\rm dot}) = (2, 8)$ μm and $w_{\rm trap} = 2.25$ μm.

Wigner molecules have even larger energies and require correspondingly deeper traps, which can be generated by larger electrode voltages.

It is important that the potential inside the dot is smooth on the scale of the zero-point energy, since a rough electrostatic potential with unpredictable minima could trap electrons in unwanted locations and could significantly distort the electron-cavity response. Pinning sites can originate from lithographic imperfections in the electrodes and from unwanted trapped charges in the silicon substrate. We do not expect these charge traps for our electron-on-helium dot, since (i) the fabricated electrodes look smooth and should therefore give rise to a smooth potential (ii) electrons float at least 1 μm from the nearest electrodes such that fabrication imperfections are further attenuated, and (iii) we have minimized the surface area of exposed Si by covering it with a superconductor.

The trap depth also plays a role in the lifetime of trapped electrons, here defined as the time electrons are confined within the dot. Electrons on helium can be contained almost

indefinitely inside our dot, since the quantum tunneling rate of electrons through the barrier is negligible. This can be seen from the spatial wavefunction decay

$$\exp\left(-\frac{\ell_{\mathrm{rg}}}{\sqrt{\hbar^2/2m_e(U_0-E)}}\right), \tag{2.15}$$

where $\ell_{\mathrm{rg}} = 0.4$ µm is the barrier length and $U_0 \approx 5$ meV is a typical trap depth. Since $\sqrt{\hbar^2/2m_e U_0} \approx 3$ nm, the tunneling length is very small compared to the barrier length ℓ_{rg} and tunneling can be ignored.

2.3.2 Trap frequency

For a single electron, the orbital frequency is exclusively set by the curvature of the electrostatic potential. In the center of the dot the electrostatic potential can be approximated by

$$V(x,y) = \alpha_0 + \alpha_1 y^2 + \alpha_2 y^4 + \beta_1 x^2, \tag{2.16}$$

and α_0, α_1 and α_2 all vary linearly with the resonator and trap voltage:

$$\alpha_i = \alpha_i^{\mathrm{res}} V_{\mathrm{res}} + \alpha_i^{\mathrm{trap}} V_{\mathrm{trap}} \tag{2.17}$$

Having two electrodes to control the electrostatic potential is advantageous compared with a single electrode, because with the two-electrode design of Fig. 2.6 the trap depth and trap curvature can be set independently. This is not possible with a single electrode and as a consequence, the voltage for which a single electron is on resonance with the resonator often coincides with a very small trap depth. For our design, the electron frequency in the y-direction depends on both the resonator and trap curvatures:

$$f_e^y = \frac{1}{2\pi}\sqrt{\frac{2e\left(\alpha_1^{\mathrm{res}} V_{\mathrm{res}} + \alpha_1^{\mathrm{trap}} V_{\mathrm{trap}}\right)}{m_e}}, \tag{2.18}$$

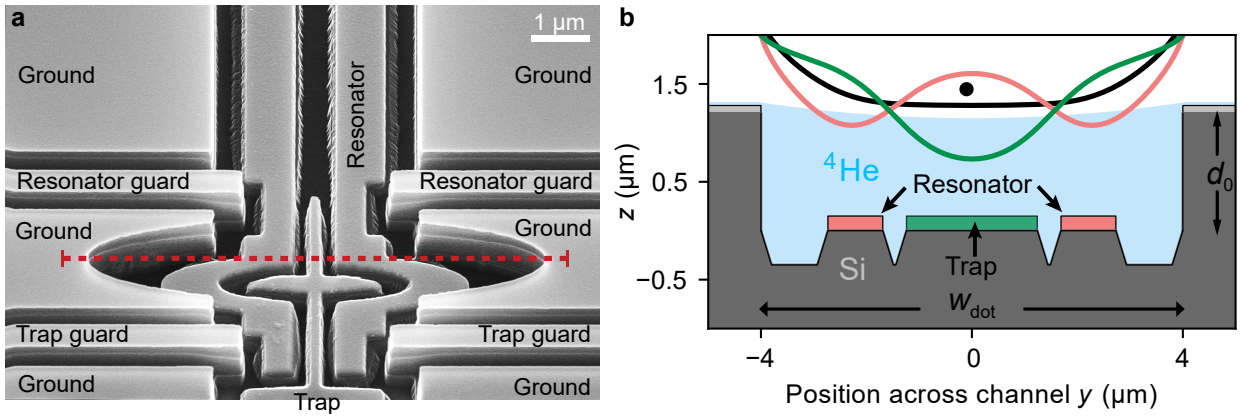

Figure 2.6: Contributions of the trap (green) and resonator (red) electrodes to the electrostatic potential, evaluated at the dashed line shown in (a). (b) The electrostatic potential shown in red (green) is obtained by finite element modeling with $V_{\mathrm{res}} = 1$ V ($V_{\mathrm{trap}} = 1$ V), while the other electrode is kept at ground. The curvatures of both potentials at the expected electron position (black dot) have opposite sign, allowing us to bring the electron frequency into resonance with the microwave resonator, while maintaining a large trap depth. The black curve is the sum of both potentials and represents a realistic potential for when $f_e \approx f_0$.

and due to the electrode geometry of Fig. 2.6, the resonator curvature α_1^{res} is negative whereas the trap curvature α_1^{trap} and $\alpha_0^{\mathrm{res}}, \alpha_0^{\mathrm{trap}}$ are all positive. Therefore, for a given resonator voltage V_{res}^* we can always find a trap voltage V_{trap}^* such that $f_e^y = f_0$. Since the trap depth only increases for larger V_{res}^* and V_{trap}^* a single electron in such a dot can be resonant at much larger trap depths, allowing for a more stable single electron trap.

We choose the shape of the dot such that the electron is more likely to oscillate in the y-direction where it couples with the resonator. Motion in the x-direction can be excited by unforeseen xy-coupling terms in Eq. (2.16), but is unlikely if the frequency in the x-direction is far off-resonant from f_e^y. Because the width of the dot ($w_{\mathrm{dot}} = 8$ μm) is much larger than the length of the dot ($\ell_{\mathrm{dot}} = 2$ μm), the motional frequency $f_e^x = 1/2\pi\sqrt{2e\beta_1/m_e}$ is typically twice as large as f_e^y. The electron is therefore much more likely to oscillate in the y-direction.

In Fig. 2.7, we show quantitatively that this dot provides an appropriate electrostatic trap with a trap frequency that is adjustable with voltage. Numerical simulations of the trap depth and trap frequency show that over a large range of V_{trap} and V_{rg}, the trap depth is more than 10 meV and the electron frequency can be tuned into resonance with the

resonator. In addition, these simulations confirm that the trap frequency in the x-direction remains far detuned from f_e^y at the resonance condition. In the next section we discuss the final figure of merit for the dot: the anharmonicity.

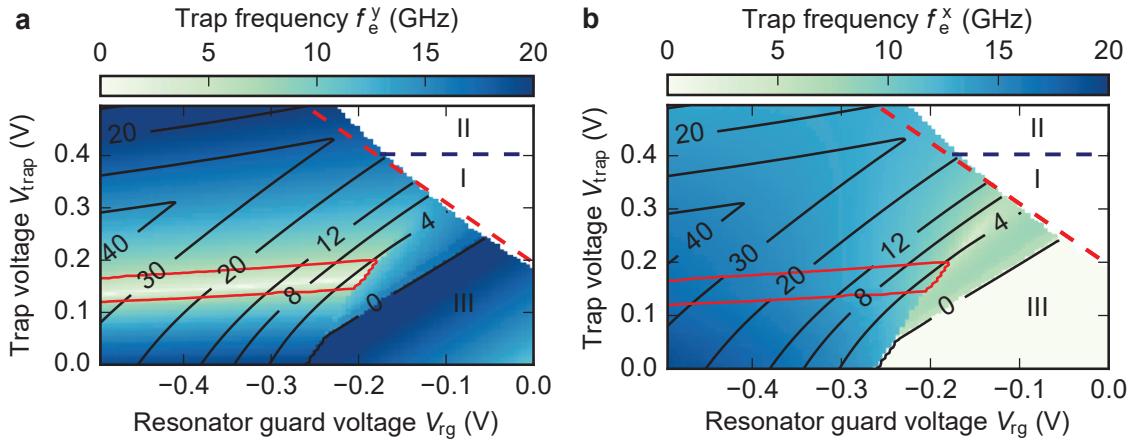

Figure 2.7: Summary of the trap depth and trap frequency for $V_{\text{res}} = 0.6$ V. (a) In color, we show the trap frequency in the y-direction as function of the resonator guard and trap voltage. The solid red contour shows for which voltages the electron will be resonant with the resonator if $f_0 = 6.5$ GHz. The white region indicates that the barrier height is too small to separate the electron reservoir from electrons in the dot. This region is divided in two subregions, I and II. In region II the electron reservoir is unstable, since electrons can flow from the resonator electrode towards the trap electrode. In region I, the reservoir can be contained on top of the resonator without issue. The trap depth (in meV) decreases for smaller V_{trap} and more positive V_{rg}, as shown by the solid black contours. Since, in region III the trap depth is too small to trap electrons inside the dot, trapping electrons is only possible in the colored area with a positive trap depth. (b) Same as in (a), except here we plot the trap frequency in the x-direction. At the resonance condition ($f_e^y = f_0$), $f_e^x \approx 2f_e^y$ such that the electron is much more likely to oscillate in the y-direction.

2.3.3 Trap anharmonicity

To selectively address the ground and first excited motional states without populating higher energy levels, the electrostatic potential must contain an anharmonic y^4 term. A large anharmonicity is desirable, since one can quickly inverse the population of the qubit without populating higher energy levels. For superconducting qubits the anharmonicity typically exceeds 100 MHz, such that qubit inversion within 10 ns is possible [61]. To quantify the amount of anharmonicity for our electron-on-helium dot, we define it as the energy difference

between the $1 \to 2$ and $0 \to 1$ transition, which can be estimated by treating the y^4 term as a perturbation to the harmonic oscillator Hamiltonian in second quantized form[1]:

$$\hbar\alpha = \left(\tilde{E}_2 - \tilde{E}_1\right) - \left(\tilde{E}_1 - \tilde{E}_0\right). \tag{2.19}$$

$\tilde{E}_n = E_n + \alpha_2\langle n|(a+a^\dagger)^4|n\rangle$ are the perturbed eigenenergies. After the commutator algebra from the $(a + a^\dagger)^4$ term, we arrive at

$$\langle n|(a + a^\dagger)^4|n\rangle = \frac{3\hbar^2}{4m_e^2\omega_e^2}(2n^2 + 2n + 1) \tag{2.20}$$

Plugging this into Eq. (2.19) gives

$$\frac{\alpha}{2\pi} = \frac{1}{2\pi}\frac{3e\alpha_2\hbar}{m_e^2\omega_e^2} \tag{2.21}$$

For simulated values of α_2 we obtain $\alpha/2\pi \approx 85$ MHz, on par with typical values for superconducting transmon qubits.

2.4 Integration of the dot with the resonator

The resonator serves as the electron detector and must therefore be integrated with the electron-on-helium dot. Successful integration means that the dot can be loaded from the electron reservoir above the resonator, and the electron motion inside the dot couples to the resonator. In addition, a successful integration minimizes decoherence due to electron decay into the DC bias electrodes and due to capacitive coupling between resonator and bias electrodes.

1. We can obtain a more direct estimate of the anharmonicity by solving the full Schrödinger equation of a single electron in the anharmonic potential. These calculations typically agree well with the estimate from perturbation theory.

2.4.1 Loading the dot from the reservoir

Electron transport from the reservoir to the dot occurs when the chemical potential of the reservoir exceeds the electrostatic barrier between the resonator and the dot. To change the barrier height independently of the reservoir's chemical potential, we use the resonator guard electrodes. The barrier height can be controlled with applied voltage and also depends on how far the resonator guard electrodes extend towards the center of the channel (w_{rg} in Fig. 2.5). With the electrodes slightly protruding into the channel there is a barrier even at $V_{\mathrm{rg}} = 0$ V, which helps to keep trapped electrons inside the dot. However, it also bars electron transport at low electron densities and if the electrodes extend too far inwards, it could block electron transport altogether.

To isolate single electrons from the reservoir, the length of the resonator guard electrode ℓ_{rg} must be smaller than the average electron spacing in the reservoir r. If $\ell_{\mathrm{rg}} \gg r$ the resonator guard electrode affects the electrostatic potential on a scale that is larger than the inter-electron spacing, which makes isolating individual electrons difficult. The electron spacing can be estimated from the reservoir electron density n_s

$$r = \frac{1}{\sqrt{\pi n_s}} \approx \sqrt{\frac{e t_{\mathrm{He}}}{\pi \varepsilon_0 \varepsilon_{\mathrm{He}} V_{\mathrm{res}}}}, \tag{2.22}$$

which varies only weakly with V_{res} and for a typical reservoir density of $n_s \approx 6 \times 10^{12}$ m^{-2} amounts to $r \approx 0.23$ µm. Electrodes with this dimension are easily fabricated using electron beam lithography.

The reservoir chemical potential $-eV_e$ depends on the bias voltage and the number of electrons in the reservoir and is given by $-eV_e = -eV_{\mathrm{res}} + e^2 n_s t_{\mathrm{He}}/\varepsilon_0 \varepsilon_{\mathrm{He}}$ [18]. If the chemical potential exceeds the barrier $-eV_b$ electrons can enter the dot (Fig. 2.8b). The barrier is mostly controlled by the resonator, resonator guard and trap electrodes, since those electrodes have a large relative contribution C_i/C_Σ at the location of the barrier (Fig. 2.8a).

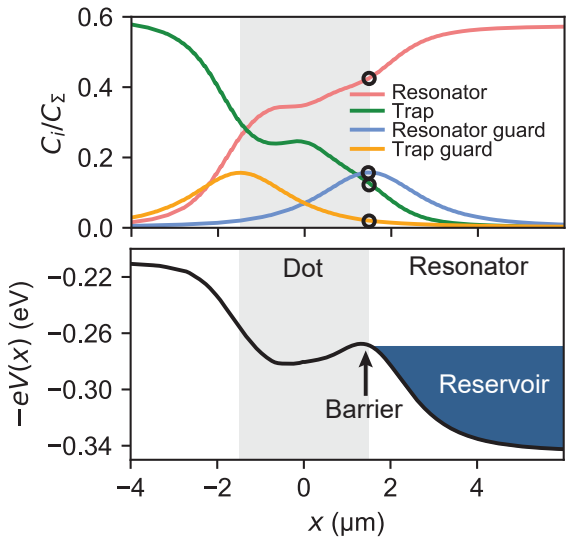

Figure 2.8: Electrode lever arms (top) and electrostatic potential (bottom) along the center of the channel near the dot for $V_{\text{res}} = 0.6$ V, $V_{\text{trap}} = 0.35$ V and $V_{\text{rg}} = -0.2$ V. The shaded region ($-1.5 < x < 1.5$ μm) represents the dot. The barrier between the dot and resonator controls electron transport from the reservoir to the dot. Its height can be most effectively controlled by the resonator, resonator guard and trap electrodes, since those electrodes have the largest lever arm C_i/C_Σ at the location of the barrier (black circles in the top figure). Note that the resonator guard and trap guard have symmetric lever arms around $x = 0$, due to the symmetric dot design.

We may therefore write

$$V_b \approx \left(\frac{C_{\text{res}}}{C_\Sigma}\right) V_{\text{res}} + \left(\frac{C_{\text{trap}}}{C_\Sigma}\right) V_{\text{trap}} + \left(\frac{C_{\text{rg}}}{C_\Sigma}\right) V_{\text{rg}}, \tag{2.23}$$

where $C_\Sigma = C_{\text{res}} + C_{\text{trap}} + C_{\text{rg}} + C_{\text{gnd}}$ is the total capacitance of the barrier. Therefore, loading of the dot is possible for those V_{rg}, V_{trap} that satisfy

$$\left(\frac{C_{\text{trap}}}{C_\Sigma}\right) V_{\text{trap}} + \left(\frac{C_{\text{rg}}}{C_\Sigma}\right) V_{\text{rg}} > V_{\text{res}} \left(1 - \frac{C_{\text{res}}}{C_\Sigma}\right) - \frac{e n_s t_{\text{He}}}{\varepsilon_0 \varepsilon_{\text{He}}} \tag{2.24}$$

The boundary of this region is represented by a straight line in V_{rg}, V_{trap}-space that depends on the electron density. We will see the return of this straight line in chapter 4.

2.4.2 Single electron coupling strength

In Section 1.3.1 we have already seen that the single-electron photon coupling strength can be large, due to a large zero-point motion and a concentrated microwave electric field E_y. However, E_y depends strongly on the resonator geometry and how the dot is integrated with the resonator. The most accurate way to evaluate the single-electron coupling strength for our dot is to calculate the wavefunctions by solving the Schrödinger equation of an electron in an electrostatic potential. In addition, the eigenenergies of this Hamiltonian yield the anharmonicity, such that we can verify the estimates from perturbation theory in section 2.3.3.

The Schrödinger equation in two dimensions, discretized on a Cartesian lattice with point spacing $\Delta x, \Delta y$, reads

$$\begin{aligned} -\frac{\psi_n(x_k-\Delta x,y_k)-2\psi_n(x_k,y_k)+\psi_n(x_k+\Delta x,y_k)}{\Delta x^2}+ \\ -\frac{\psi_n(x_k,y_k-\Delta y)-2\psi_n(x_k,y_k)+\psi_n(x_k,y_k+\Delta y)}{\Delta y^2}+ \\ \frac{2m_e}{\hbar^2}eV(x_k,y_k)\psi_n(x_k,y_k)=\frac{2m_e}{\hbar^2}E_n\psi_n(x_k,y_k) \end{aligned} \tag{2.25}$$

$\psi_n(x_k, y_k)$ are the two-dimensional wave functions and $E_n = \hbar\omega_n$ are the eigenenergies. The electrostatic potential $V(x_k, y_k)$ is obtained by solving Poisson's equation using the finite element method. Next, we export the potential values near the dot, at height t_{He} from the bottom of the channel and cast the values to a regular Cartesian grid using linear interpolation (Fig. 2.9b). We then diagonalize Eq. (2.25) to find the eigenmodes and mode frequencies.

In Fig. 2.9a we plot the transition frequencies from the ground state and show that the transition frequency of the first excited state varies from $0 - 10$ GHz by varying V_{trap}. If our microwave resonator has a resonance frequency $f_0 = 6.5$ GHz, a single electron would be resonant with the microwave mode for $V_{\mathrm{trap}} \approx 0.18$ V. All higher frequency transitions correspond with higher excited states, which we label according to their dominant direction

of motion. For example, $\psi_1(x,y) = |1_y\rangle$ is the first excited state which predominantly oscillates in the y-direction. These eigenmodes (Fig. 2.9c-f) closely resemble the eigenmodes of a harmonic oscillator with different trap curvatures in the x and y directions.

The color of each line in Fig. 2.9a reflects the coupling strength of each transition, which is calculated from the differential mode amplitude $V_{\mathrm{RF}}(x,y)$ and the ground and excited state wavefunctions $\psi_n = |n\rangle$. Mathematically it takes on the form

$$g_{0n}/2\pi = \frac{e}{2\pi}\iint \langle 0| \left(x\frac{\partial V_{\mathrm{RF}}}{\partial x} + y\frac{\partial V_{\mathrm{RF}}}{\partial y}\right) |n\rangle dx\, dy \tag{2.26}$$

$$= \frac{e}{2\pi}\sum_{j,k} \psi_0^\dagger(x_j,y_k)\left(x_j E_x(x_j,y_k) + y_k E_y(x_j,y_k)\right)\psi_n(x_j,y_k) \tag{2.27}$$

It is clear that the ground state $|0\rangle$ couples strongest to the first excited state in the y-direction (i.e. $|1_y\rangle$) and the coupling strength reaches several MHz. Direct transitions from the ground state to other states are either forbidden by symmetry (e.g. $|0\rangle \Longleftrightarrow |2_y\rangle$) or extremely weakly coupled due to vanishing E_x (e.g. $|0\rangle \Longleftrightarrow |1_x\rangle$).

Although the eigenmodes look like those of a harmonic oscillator, closer inspection of the transition frequencies reveals that the frequency spacing is non-uniform. In Fig. 2.9g we plot the anharmonicity, defined as the difference between $f_{|1_y\rangle\rightarrow|2_y\rangle}$ and $f_{|0\rangle\rightarrow|1_y\rangle}$. At the crossing ($V_{\mathrm{trap}} \approx 0.18$ V) the anharmonicity exceeds 0.1 GHz, which is close to the estimate from section 2.3.3 ($\alpha/2\pi \approx 85$ MHz). This large anharmonicity is due to a significant y^4 term in the electrostatic potential and indicates that the electron can be approximated as a two-level system.

The coupling strength of this design is slightly smaller than our naive estimate in section 1.3.1 ($g/2\pi \approx 18$ MHz), because the transverse microwave field is smaller than 10^6 V/m. To increase the coupling strength in future designs, we can increase w_{cp} or decrease w_{trap} or d_0. However, this affects the crossing voltage V^*_{trap} and we must be careful that electrons can remain in the dot at this new crossing voltage. One can also increase the coupling strength with a larger resonator impedance Z, e.g. through the use of thinner superconducting films

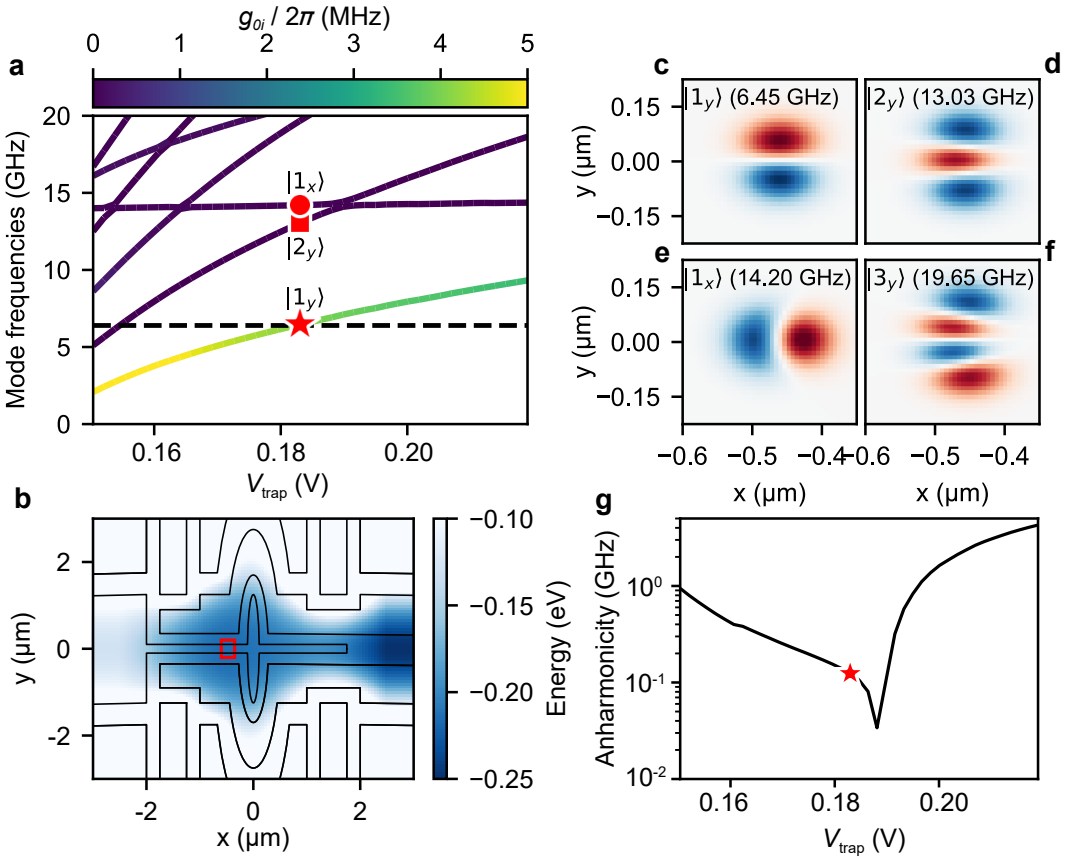

Figure 2.9: Quantum mechanical calculation of a single electron on helium (a) Transition frequencies for a single electron in the ground state, calculated by solving the Schrödinger equation in a two-dimensional electrostatic potential. The color of each line reflects the coupling strength g_{0n} for each state. The resonator frequency is shown as a black dashed line. (b) Simulated electrostatic potential at $z = 1.15$ µm and $V_{\text{trap}} = 0.184$ V. A red rectangle shows the extent of the single-electron wavefunctions shown in (c)-(f). (c)-(f) Wave functions of the excited states of a single electron near the crossing voltage $V_{\text{trap}} = 0.184$ V. The red and blue regions are non-zero wave function amplitudes of opposite sign. (g) Inferred anharmonicity of a single electron as function of trap voltage. A red star marks the anharmonicity at the crossing voltage.

or high-kinetic inductance superconductors [48] (see section 6.1.1).

2.4.3 Minimizing microwave loss through DC electrodes

In the dot area, the resonator is surrounded by bias electrodes which are only a few microns away. As a result, capacitive coupling between the resonator and electrodes forms an unwanted loss channel for resonator photons, broadening the cavity linewidth κ_{int}. This poses a threat to circuit QED with an electron on helium in the strong coupling regime, especially when the unwanted capacitance is large. To better understand how much capacitive coupling we can tolerate, we have simulated the effect of this parasitic capacitance using the ABCD matrix formalism [62].

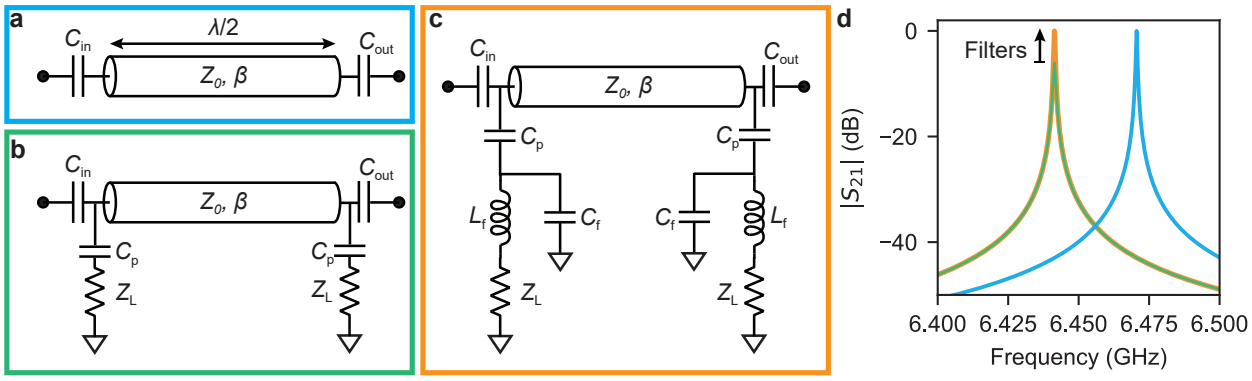

Figure 2.10: Suppression of microwave radiation through DC bias electrodes. (a)-(c) Circuit models of increasing complexity used to simulate the effect of impedance engineering of the bias electrodes. The parasitic capacitance C_p describes the unwanted coupling of microwave radiation from the resonator (depicted as a lossless transmission line) to the DC bias electrodes. With an LC-filter this radiation can be suppressed, as shown in (c). (d) Simulated transmission spectra for the circuit models depicted in (a)-(c). Compared to the isolated resonator (blue) the addition of parasitic capacitance results in a decrease in resonator Q, visible as a decreased peak transmission. The resonator transmission can be recovered by adding LC filters (orange). For this simulation $C_{\text{in}} = C_{\text{out}}$ =3.5 fF, $C_{\text{p}} = C_{\text{in}}$, L_f = 2.5 nH, $C_f = 4$ pF, $Z_L = 50\,\Omega$ and the designed resonance frequency was $f_0 = 6.5$ GHz.

For simplicity, we model the microwave resonator as a lossless transmission line of length $\ell = \lambda/2$, as shown in Fig. 2.10a. Similar to the differential coplanar stripline resonator, the voltage eigenmodes of this resonator have antinodes at the tip(s) of the resonator and therefore correctly model the physics of our coplanar stripline resonator. Upon addition of

the bias electrodes, resonator photons can decay to the bias leads via the capacitance C_p, which is connected to a low impedance ($Z_L = 50\ \Omega$) environment (Fig. 2.10b). The input impedance of the bias line as seen by resonator photons is

$$Z_{\text{eff}} = Z_L + \frac{1}{i\omega C_p}. \tag{2.28}$$

To model the transmission through this resonator we construct the ABCD matrix of the total system:

$$\begin{pmatrix} A & B \\ C & D \end{pmatrix} = \begin{pmatrix} 1 & \frac{1}{i\omega C_{\text{in}}} \\ 0 & 1 \end{pmatrix} \begin{pmatrix} 1 & 0 \\ \frac{1}{Z_{\text{eff}}} & 1 \end{pmatrix} \begin{pmatrix} \cos(\beta\ell) & iZ_0 \sin(\beta\ell) \\ \frac{i}{Z_0}\sin(\beta\ell) & \cos(\beta\ell) \end{pmatrix} \begin{pmatrix} 1 & 0 \\ \frac{1}{Z_{\text{eff}}} & 1 \end{pmatrix} \begin{pmatrix} 1 & \frac{1}{i\omega C_{\text{out}}} \\ 0 & 1 \end{pmatrix}, \tag{2.29}$$

where $\beta = \omega/c$ is the wave number. The resulting transmission spectrum $|S_{21}|$ for a pessimistic scenario $C_p = C_{\text{in}}$ is depicted in Fig. 2.10d and shows a reduction in peak amplitude due to a decrease in internal Q. Since the internal quality factor scales as $1/(\omega_0 Z_L C_p)^2$, it is important to keep C_p as small as possible during the design of the dot, for example by keeping the electrodes away from the resonator or by keeping the surface area small.

By carefully engineering the impedance of the bias electrodes, it is possible to suppress microwave leakage and thus restore the resonator internal Q, even when C_p is large. To illustrate this concept we add an LC filter to each bias electrode, a technique that has been very successful in achieving strong coupling with semiconductor double quantum dot devices [55, 63, 64]. In these devices suppression of microwave radiation through the bias electrodes is extremely important, since the bias electrodes are only 10-100 nm separated from the resonator center pin.

By adding the LC filter (Fig. 2.10c), the input impedance of the bias electrode becomes

$$Z_{\text{eff}} = \frac{1}{i\omega C_p} + \frac{1}{i\omega C_f + \frac{1}{i\omega L_f + Z_L}}, \tag{2.30}$$

where C_f and L_f are the capacitance and inductance of the filter, respectively. The resulting transmission spectrum has unit transmission on resonance, indicating that the internal quality factor is at least as large as the coupling quality factor. Therefore, by adding LC filters, one can very effectively suppress radiation from the resonator to the bias electrodes, even when the parasitic capacitance C_p is large.

We have designed and fabricated an on-chip LC-filter consisting of a two-dimensional coil in series with an interdigitated capacitor (Fig. 2.11a). To verify its performance, we measure the microwave transmission through the series network (Fig. 2.11b), and find that the filter attenuates transmitted signals by 18 dB at the microwave resonance frequency $f_0 = 6.5$ GHz. Therefore, the filter acts as a microwave mirror and, when attached to bias electrodes as in Fig. 2.11a, should prevent microwave leakage into each bias electrode.

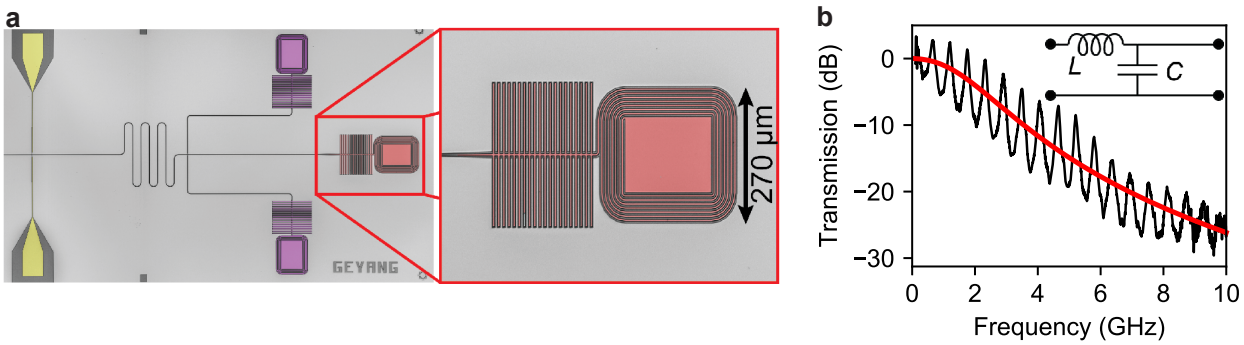

Figure 2.11: (a) Each bias electrode is equipped with an LC-filter, which consists of a two-dimensional coil and interdigitated capacitor to ground. A close-up shows the relatively small footprint of this filter. (b) Measured microwave transmission through the filter. The solid red line shows the modeled transmission, derived from the circuit shown in the inset with $L = 2.5$ nH and $C = 4$ pF. The oscillations in the measured transmission are likely due to an impedance mismatch between the filter and the transmission line. At the microwave resonance frequency, the transmission is attenuated by 18 dB.

2.4.4 Minimizing electron decoherence

The symmetric design of the dot ensures the potential minimum is in the center of the microchannel and plays an important role in the linewidth of a single electron. An electron in the center of the channel can radiate into the bias electrodes via a differential mode, where the

induced charge on a pair of electrodes is equal and opposite (Fig. 2.12a). We estimate the increase in electron linewidth due to radiation into the bias electrodes by comparing it with the estimated coupling to the resonator ($E_y^{\text{diff}} \approx 2 \times 10^5$ V/m and $g/2\pi \approx 5$ MHz). Fig. 2.12c shows that the coupling to other bias electrodes is much weaker than the coupling to the microwave resonator. Therefore, any microwave emission into the bias electrodes occurs at a rate slower than $g/2\pi$, and should not pose a threat to reaching the strong coupling regime.

Fabrication imperfections or trapped charges may shift the electron away from the center of the channel. In that case, the electron may also radiate into a common mode of the electrodes, where the induced charge on a pair is equal (Fig. 2.12a). Fig. 2.12b shows that the trap electrode is the dominant pathway for decay. However, a pessimistic 100 nm offset only yields a decay rate of a fraction of g. In addition, these estimates do not take into account the LC-filters described in section 2.4.3, which should act as microwave mirrors and prevent this type of leakage. Therefore, we conclude that a well designed symmetric trap is important, but should not prevent circuit QED with electrons on helium in the strong coupling regime.

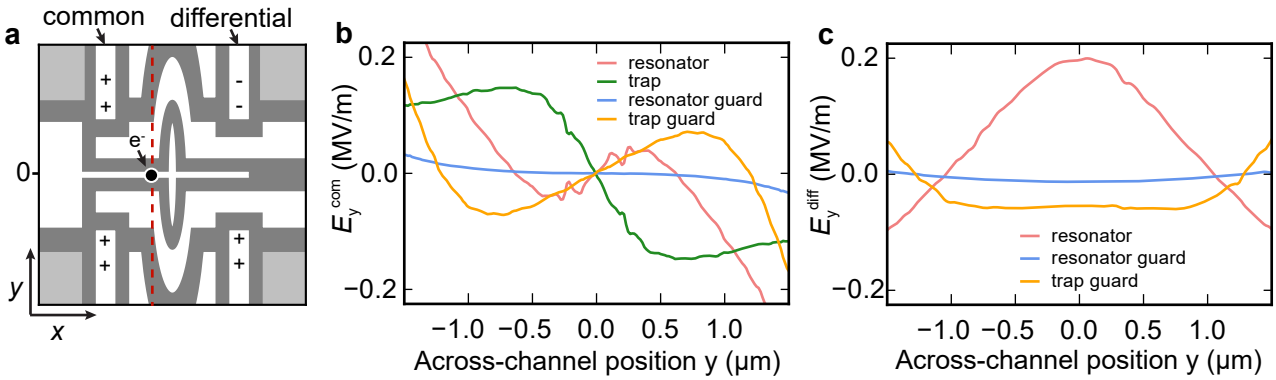

Figure 2.12: (a) Schematic of the electrode geometry in the dot area, showing the expected electron position and an example of charge distributions on the trap guard and resonator guard which correspond to common and differential microwave leakage, respectively. (b) Common mode E_y simulated at the red dashed line in (a). The values of E_y at the electron position provide an estimate for microwave leakage through each respective electrode. (c) Same as in (b), but for the differential mode. Note that the trap electrode does not support a differential mode.

CHAPTER 3

EXPERIMENTAL SETUP

Strongly correlated electron physics and quantum mechanical effects in circuit QED are only visible at very low temperatures, when the interaction energy and electron zero-point energy dominate over the thermal energy. Therefore, all experiments presented in this thesis are performed in a dilution refrigerator (Oxford Triton 200), a device with a minimum operating temperature of only 20 mK.

The four components of circuit QED with electrons on helium (i.e. the microwave resonator, DC electrodes, liquid helium and electrons) must behave harmoniously at the mixing chamber plate of the refrigerator. In this chapter, we describe how we interface these components, without destroying the resonator Q or losing the liquid helium, for example. First, we describe how to supply the liquid helium to our sample cell and how to contain the helium inside the micro-channels (section 3.1). The sample cell (section 3.2) also provides a quiet microwave environment, essential for sensitive microwave measurements. A good explanation of the required microwave equipment can be found in most circuit QED theses (e.g. Ref. [40]), so we only provide a concise description of the microwave setup in section 3.5. Finally, in section 3.6 we show how we filter the bias electrodes to prevent electron dephasing due to voltage noise.

3.1 Superfluid helium supply and thermalization

Liquid helium, which eventually fills the on-chip micro-channels, is supplied from a high-purity ^{4}He gas cylinder at room temperature. This cylinder is connected to a helium manifold, which can repeatedly deliver controlled amounts of helium gas to the sample box inside the dilution refrigerator.

The helium manifold has four ports controlled by solenoid valves, as depicted in the schematic of Fig. 3.1a. These ports are used to evacuate and fill the control volume (V_c =

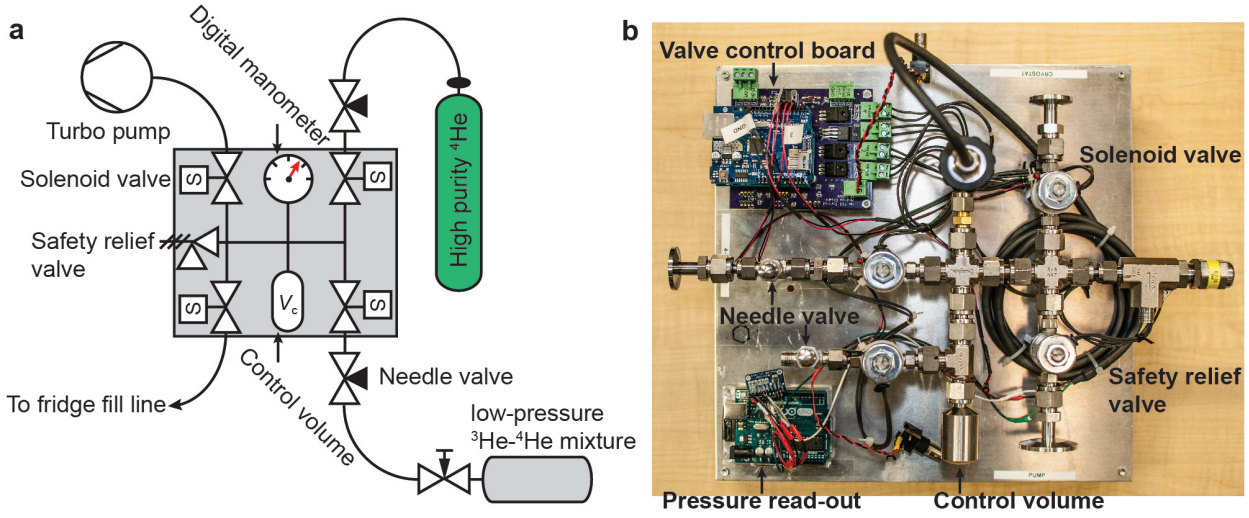

Figure 3.1: (a) Schematic of the helium manifold, controlled by four solenoid valves (IMI Norgren 141011 2WNC). The control volume (Swagelok SS-4CS-TW-10, $V_c = 10$ cm^3) can be filled with ^{4}He gas or a dilute ^{3}He-^{4}He mixture while the pressure is monitored by a digital pressure sensor (Swagelok PTI-S-NC30-22AQ). A safety relief valve limits the pressure inside the manifold to approx. 3 bar. (b) Photograph of the apparatus, also showing the control boards for switching the solenoid valves and pressure read-out.

10 cm^3), and release the helium gas towards the helium fill line inside the refrigerator. The sequence to deliver a single control volume of gas to the sample box ("puff") consists of evacuating the control volume with the turbo pump, briefly opening the helium gas port to pump out the volume behind the needle valve and then closing the pump port. The pressure is then monitored until the digital manometer reads $P = 0.25$ bar after which the helium supply valve is closed and the puff is released to the cryostat.

From room temperature to the 4 K plate, the gas travels through wide stainless steel tubing (0.080" ID), which acts as a cold trap for any remaining impurities such as water vapor. We ensure the injected helium gas thermalizes to the refrigerator by brazing it to OFHC copper cylinders bolted to the the 35 K and 4 K stage. Below the 4 K plate, the inner diameter of the fill line is reduced (0.021" ID) and the tube length between stages is increased by coiling the tubing as shown in Fig. 3.2. This reduces the heat load on the colder stages, because the conductivity of the column of superfluid helium below the still

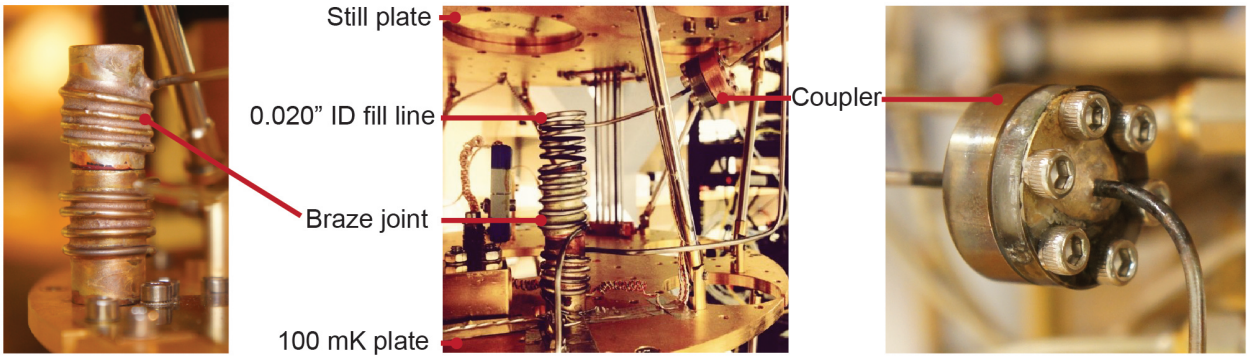

Figure 3.2: Photograph of the helium fill lines inside the dilution refrigerator. The stainless steel tubing is coiled between plates to reduce the heat load, and brazed to 0.25" diameter copper cylinders to thermalize the superfluid helium inside the fill line.

plate scales linearly with the inner diameter of the tube d:

$$\kappa_4 \propto 20 d T^3, \tag{3.1}$$

where κ_4 is the thermal conductivity in W/(K cm) [24]. Tubes with even smaller ID further decrease the heat load from the superfluid helium column, but also make experiments impractical, since evacuating the sample cell dead volume through smaller ID tubing takes correspondingly longer.

Thermalizing liquid helium to the mixing chamber plate is not trivial, because liquid helium has a large interfacial thermal (Kapitza) resistance, due to a mismatch in speed of sound between liquid helium and solids [65]. Even though we have no direct way of measuring the temperature of liquid helium, we expect the liquid helium to be well thermalized, since the amounts used in the experiments are small and adding liquid helium does not increase the mixing chamber plate temperature. To improve thermalization of the helium, we could insert copper or silver sinter heat exchangers right before the sample cell. The metal powder inside these heat exchangers increases the contact area with helium by orders of magnitude, thereby reducing the Kapitza resistance [24].

As helium flows down to the mixing chamber it accumulates in a cylindrical reservoir (diameter $d \approx 5$ mm) inside a hermetic sample cell. The vertical distance from the reservoir

liquid level to the on-chip micro-channel determines whether the micro-channels are filled and sets the curvature of the helium-vacuum interface inside the micro-channel. Since the microwave resonance frequency shift increases with the number of helium puffs, we determine the appropriate amount of helium from the frequency shift as function of added helium. Since this is very specific to the channel geometry, we will discuss this further in section 4.1 and 5.2.

3.2 Hermetic sample cell

The primary purpose of the sample cell is to contain the superfluid helium in a leak-tight cell, while allowing DC and microwaves to pass through. The cell consists of two parts: a lid and a pedestal (Fig. 3.3). The lid contains fourteen hermetic SMP microwave feedthroughs (Corning Gilbert 0119-783-1), two connections for an electron source and a feedthrough for a stainless steel helium fill line (1/16" OD, 0.021" ID). The fill line is brazed to an M4 screw with a 1/16" hole and attaches to the lid of the sample cell with a hex nut.

Inside the cell, a custom designed printed circuit board (PCB), which offers room for a 2×7 mm chip, is mounted to the pedestal using 0-80 screws (Fig. 3.3b). We connect signals from the hermetic connectors on the lid to the PCB with SMP bullets (e.g. Rosenberger 19K106-K00L5). This bullet allows for an axial misalignment between lid and PCB of up to ±0.3 mm.

Before cooling down we position an indium seal around the edge of the pedestal and tighten the assembly from the bottom using eight 4-40 screws. The flattened indium wire (diameter 0.020") prevents superfluid helium leaks. All SMP microwave connectors are also equipped with a similar seal and we have not observed superfluid helium leaks during our experiments.

The second purpose of the cell is to decrease the microwave density of states at the on-chip resonance frequency, such that higher microwave resonator quality factors can be achieved. Inside the sample cell, the density of states is discrete rather than continuous,

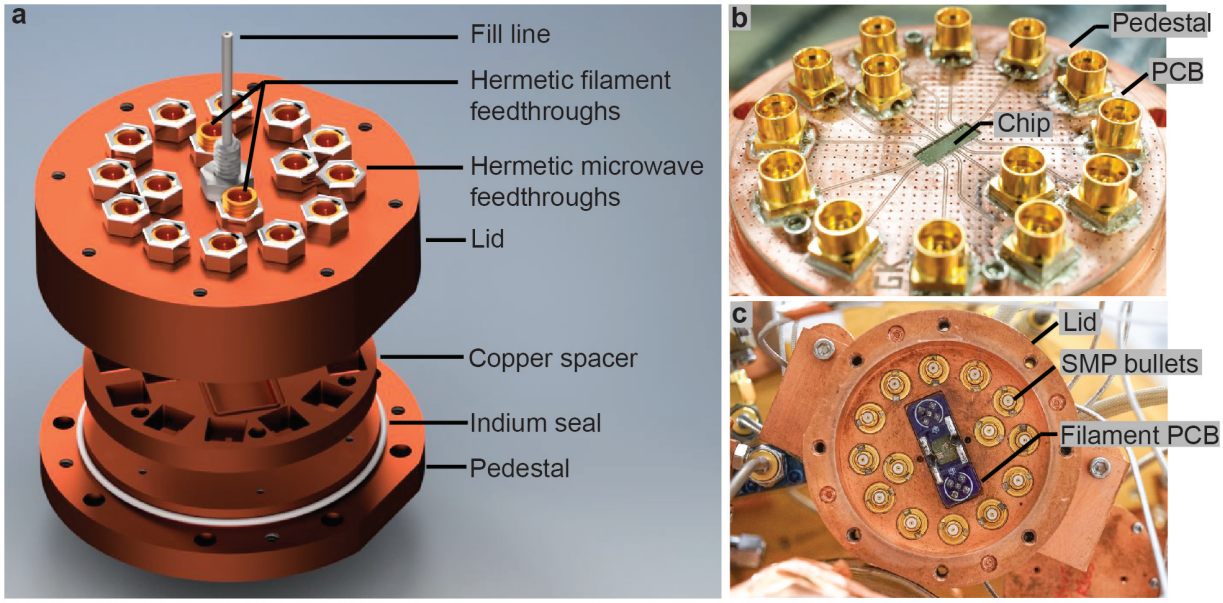

Figure 3.3: A hermetic sample cell for circuit QED with electrons on helium (a) 3D rendering of the hermetic sample cell assembly. The PCB, normally mounted between the pedestal and copper spacer is not shown. (b) Photograph of the pedestal and PCB (c) Photograph of the inside of the lid, showing the microwave feedthroughs and SMP bullets which connect to the SMP connectors on the PCB shown in (b). This photograph also shows the printed circuit board with two filaments which serve as electron sources.

and the mode frequencies can be predicted by treating the sample cell as a cylindrical cavity with inner radius $R = 2.15 \times 10^{-2}$ m. The lowest frequency eigenmode is then

$$\frac{\omega_{\text{cell}}}{2\pi} = 2.405\frac{c}{2\pi R} \approx 5.3\,\text{GHz}. \tag{3.2}$$

Ideally, the sample cell should not have eigenfrequencies below 10 GHz, otherwise low Q sample cell modes may still couple to the on-chip resonance. To increase ω_{cell}, we insert a copper spacer inside the sample cell dead volume (Fig. 3.3a). With the spacer inserted, we measure $\omega_{\text{cell}}/2\pi \approx 10$ GHz, ensuring that our on-chip microwave resonator is not affected by the eigenmodes of the sample cell.

3.3 Electron source

Our electron source is an exposed tungsten filament from a small light bulb found in model train stores (Fig. 3.4). We extract the filament by carefully cracking the glass enclosure with pliers. The two leads are then soldered to a separate printed circuit board that plugs into the inside of the sample cell lid (Fig. 3.3c).

To emit electrons, we send a pulsed current through the filament while keeping the filament negatively biased ($V_{\text{fil}} \approx -0.5$ V). The pulse amplitude is large enough to overcome tungsten's work function ($W \approx 4.5$ eV) and the negative bias ensures that emitted electrons are directed towards the positively biased microwave resonator. The pulsed current also heats the filament and generates a sizable helium vapor inside the sample cell, which scatters and slows down emitted electrons. Hence, electrons land on the helium and accumulate above the microwave resonator.

3.4 Design of a printed circuit board

The printed circuit board (PCB) connects microwave and DC signals to the on-chip microwave resonator and bias electrodes. To accommodate the large number of DC signals

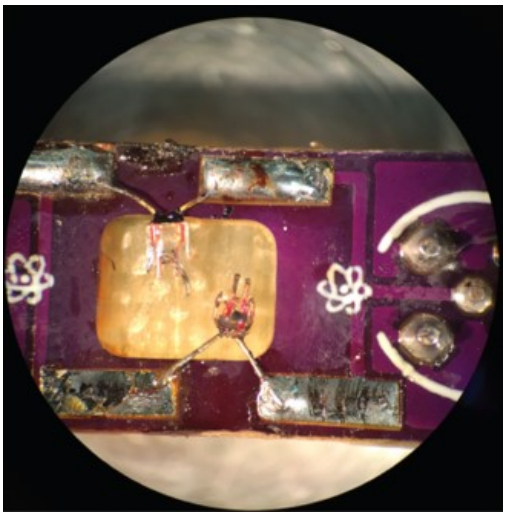

Figure 3.4: Two exposed filaments (one for backup), soldered to a printed circuit board serve as our electron source. The filaments are very delicate and hardly visible, even in this enlarged stereoscope image. After successful installation each filament has a resistance of approx. 15 Ω.

that are necessary to create the appropriate trapping potential, we designed a custom PCB with fourteen connections, which can carry high-frequency microwave signals as well as DC voltages.

Our PCB design (Fig. 3.5a) has soldering pads for fourteen SMP connectors, through-hole plated vias that short the front and back copper layers (Fig. 3.5b), and a cut-out for a 2×7 mm chip, such that the chip's top surface sits flush with the copper. The high dielectric constant of Arlon AD1000 ($\varepsilon = 10.2$) does not vary from 1-10 GHz and matches the dielectric constants of common substrates, such as sapphire and silicon ($\varepsilon \approx 11$). Additionally, in and output signals traveling on the PCB transmission lines are minimally attenuated due to a low loss tangent ($\tan\delta = 2.3 \times 10^{-3}$). The center pin width and gap width of the traces are 5.9 and 3.5 mils, respectively, chosen to match the 50 Ω impedance of the microwave cables and connectors.

We prepare our PCB for a cool down by soldering the SMP connectors to the PCB and cleaning the top surface with isopropyl alcohol. To mount the chip, we first apply GE varnish to the chip insert, which improves thermal contact between the copper bottom layer and the

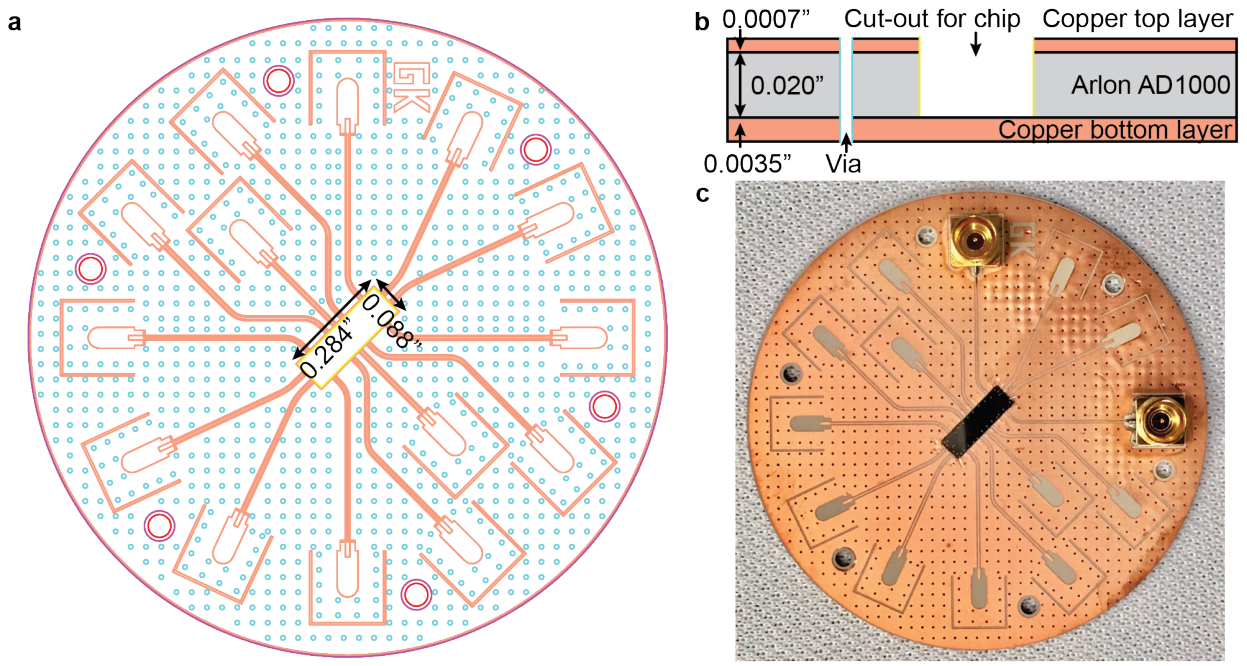

Figure 3.5: Printed circuit board (PCB) for microwave measurements with electrons on helium. (a) Design of the PCB with different colors representing different operations. Pink denotes the border of the PCB, cyan circles denote the location of through vias that connect the front and back copper pours and the yellow rectangle is an insert for a 2×7 mm chip. (b) The PCB dielectric is sandwiched between the front and back copper pours. An example of a via and the chip insert are also shown. (c) Photograph of an assembled PCB with soldered connectors and chip.

chip. After curing at room temperature for several hours, we make the electrical connections to the chip using aluminum wirebonds. Finally, the PCB assembly is mounted to the sample cell pedestal (Fig. 3.3) and is then ready to cool down.

3.5 Setup for low-noise microwave measurements

All experiments in this thesis are performed at temperatures near absolute zero to suppress incoherent microwave radiation that would otherwise obscure quantum mechanical effects. Even though at the mixing chamber plate ($T = 20$ mK) the average thermal intra-cavity photon number is much less than one:

$$n_{\mathrm{th}} = \frac{1}{e^{\hbar\omega_0/(k_B T)} - 1} \ll 1, \tag{3.3}$$

microwave cables from room temperature can still cause heating. To thermalize the microwave input lines to $T = 20$ mK, we insert cryogenic attenuators (XMA Corp.) at the 4 K and mixing chamber plate. These attenuators ensure that only coherent microwave tones from a Keysight PNA-X Network Analyzer (see Fig. 3.6) reach the resonator input port. In the same spirit, circulators (Quinstar OXE89) on the resonator output line redirect thermal radiation from the 4 K plate to ground, but provide minimal attenuation for the output signal from the resonator.

The resonator output (Fig. 3.6) is first amplified by a quantum limited Josephson Parametric Amplifier (JPA), which amplifies reflected photons with a gain of $G_1 \approx 10^2$ (20 dB) while adding a minimum amount of noise. The JPA is relatively narrow band (linewidth $\kappa/2\pi \approx 30$ MHz (Fig. 3.7a), but its operating frequency can be adjusted from 6.67 GHz to 4 GHz using magnetic flux through an array of superconducting quantum interference devices (SQUiDs) that compose the JPA's gain medium (Fig. 3.7b). Experimentally this flux is adjusted using a DC current through an off-chip coil mounted directly below the JPA. To ensure that stray magnetic fields do not affect the operating frequency, the JPA is mounted inside a lead shield and high permeability mu-metal shield. Before the reflected signal reaches the input of the network analyzer it is further amplified by a high electron mobility transistor (HEMT) amplifier (Low Noise Factory LNF-LNC48C, gain 38 dB) at $T = 4$ K and finally by a low-noise amplifier at room temperature (Miteq AFS3-00101200, gain 28 dB).

The most important and defining quantity of the setup is the signal-to-noise ratio (SNR) measured at the network analyzer. To maximize the SNR, it is important to both use low-noise amplifiers and minimize attenuation of resonator output photons. Since optimizing the SNR is such an often-encountered problem, it is worth analyzing the SNR for our three-stage amplifier chain (see Fig. 3.6).

We first calculate the signal power at port 2 of the network analyzer, P_S. This signal is amplified by the three cascaded amplifiers (gains G_1, G_2 and G_3) at different stages of the

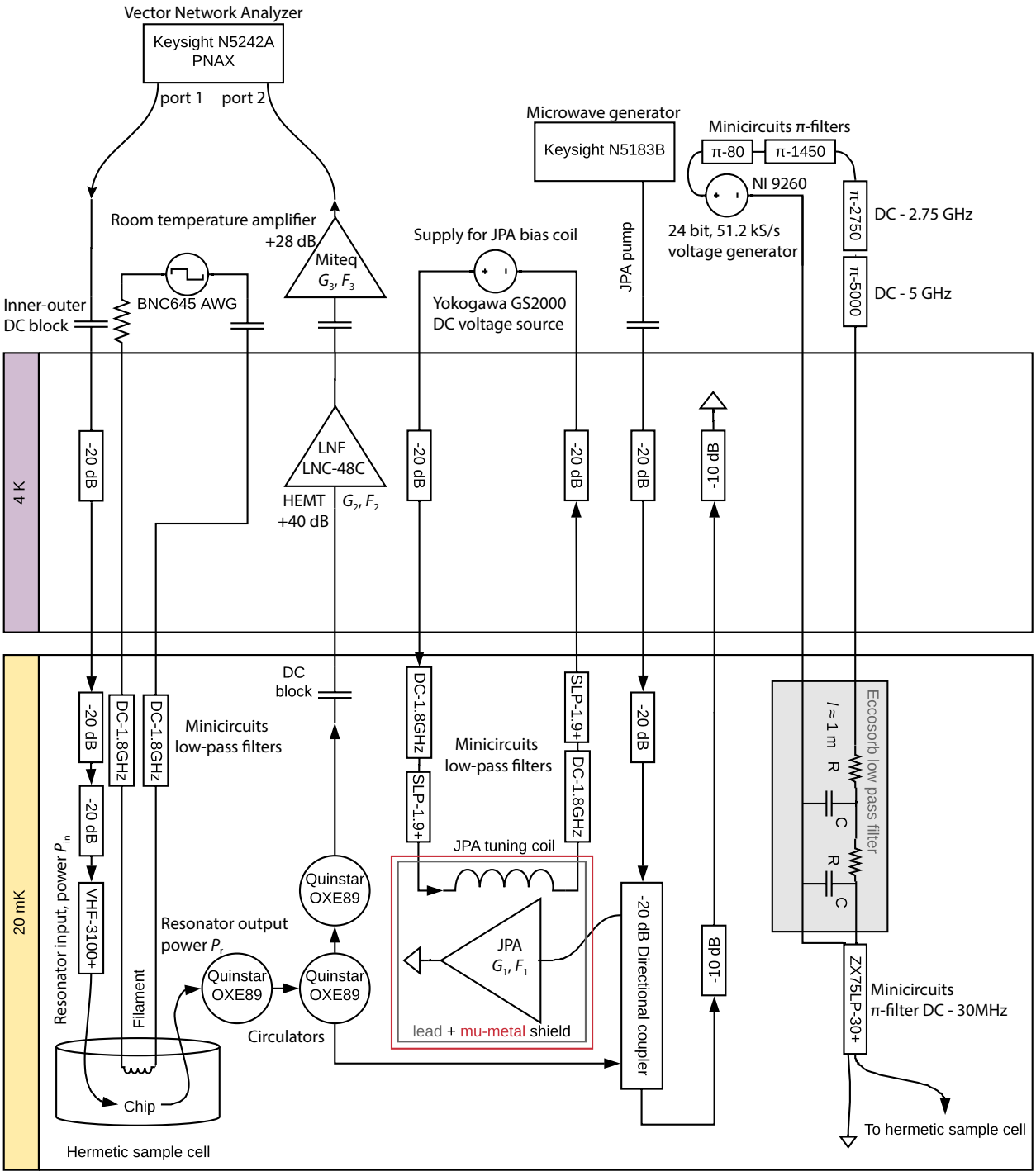

Figure 3.6: Schematic of the microwave and DC connections entering the dilution refrigerator. The room temperature equipment is shown on the top and the 4 K (mixing chamber) plate is shown in the purple (yellow) box. A Josephson Parametric Amplifier is the first amplifier seen from the resonator output and reflects photons with approximately 20 dB of gain ($G_1 \approx 10^2$). Circulators then route the signal towards the network analyzer, which measures the phase and magnitude of the scattering matrix elements S_{ij} as function of frequency. The filtering of one pair of DC wires (signal and ground) is shown on the right, and includes room temperature π filters of increasing cut-off frequency and a three-stage filter at the mixing chamber (see Section 3.6)

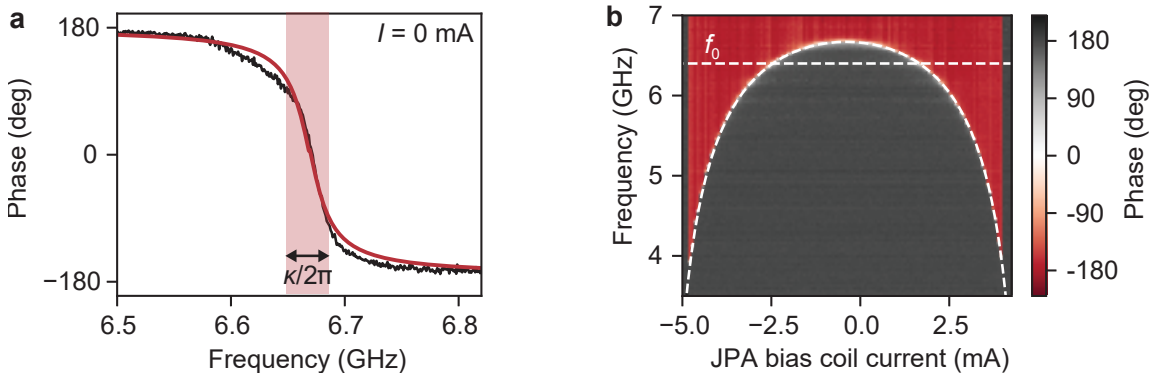

Figure 3.7: JPA calibration and tuning with current (a) Phase of microwaves reflected off the JPA, measured at zero bias current. The solid red line is a fit to $S_{11} = \frac{i(\omega-\omega_{\mathrm{JPA}})+(\gamma-\kappa)/2}{i(\omega-\omega_{\mathrm{JPA}})+(\gamma+\kappa)/2}$ and gives $\kappa/2\pi = 30$ MHz. The bandwidth of the JPA when it is operated as an amplifier is approximately $0.1\,\kappa/2\pi$. (b) Although the JPA is narrow band, the operating point can be tuned over a wide range. The horizontal dashed line indicates the microwave resonator frequency f_0, while the dashed curve is the JPA frequency as function of bias current $\omega_{\mathrm{JPA}}/2\pi$, obtained from fits to JPA spectra, such as the one in (a). $\omega_{\mathrm{JPA}}/2\pi$ follows the predicted shape from theory with a small current offset (0.4 mA) and approximately 9.6 mA needed to thread one flux quantum through the SQUiD array. Finally, the JPA can be operated as an amplifier for currents where f_0 intersects with $\omega_{\mathrm{JPA}}/2\pi$, here $I \approx -2.4, +2.0$ mA.

refrigerator before it reaches the network analyzer. Therefore, $P_S = G_1 G_2 G_3 P_r$, where P_r is the power at the output port of a two-sided microwave cavity, with output coupling rate κ_2:

$$P_r = n_{\mathrm{ph}} \hbar \omega_0 \kappa_2. \tag{3.4}$$

The average number of photons circulating in the cavity can be calculated from input output theory (Section 1.3.3), provided the input power P_{in} at the sample is known [66]:

$$n_{\mathrm{ph}} = \frac{4\kappa_1 P_{\mathrm{in}}}{\hbar\omega_0 \left(\kappa_1 + \kappa_2 + \kappa_{\mathrm{int}}\right)^2} \tag{3.5}$$

To calculate the noise power, we assume the main source of noise is Johnson noise at $T = 20$ mK, and first neglect the noise floor of any imperfect measurement apparatuses. We do take into account added noise from the amplifiers, which is characterized by the noise factor F_i. Note that amplifiers are often specified by their noise figure NF_i or noise

temperature T_i which are related to the noise factor in the following ways:

$$F_i = \left(1 + \frac{T_i}{300\,\mathrm{K}}\right) \tag{3.6}$$

$$F_i = 10^{\mathrm{NF}_i/10} \tag{3.7}$$

The total noise power from both amplified Johnson noise and added amplifier noise can be calculated from Friis' formula:

$$P_N = k_B T \Delta f G_1 G_2 G_3 \left(F_1 + \frac{F_2 - 1}{G_1} + \frac{F_3 - 1}{G_1 G_2}\right). \tag{3.8}$$

P_N depends on the measurement bandwidth Δf, usually set by the measurement equipment. Eq. (3.8) shows that the added noise from the second amplifier is attenuated by a factor $G_1 \gg 1$, and can therefore be safely neglected. Of course, the same holds true for the added noise from the last amplifier, which is attenuated by $G_1 G_2$. The final expression for the expected SNR (in dB) is thus

$$\mathrm{SNR} = 10 \log_{10}\left(\frac{P_S}{P_N}\right) \approx 10 \log_{10}\left(\frac{n_{\mathrm{ph}} \hbar \omega_0 \kappa_2}{k_B T \Delta f F_1}\right). \tag{3.9}$$

To first order the SNR does not depend on the amplifier gains, since both signal and noise are amplified equally. Furthermore, the SNR depends only on the noise factor of the first amplifier in the chain. Of all amplifiers, the quantum-limited JPA adds the smallest possible amount of noise (only half a noise quantum [67]) and therefore offers a considerable boost in SNR, as long as $G_1 \gg 1$.

In reality, the measurement apparatus may not be ideal and may have a finite noise floor P_A. In this case the SNR can be written as $\mathrm{SNR} = 10 \log_{10}(P_S/(P_N + P_A))$, which now weakly depends on the amplifier gains. In practice, with three amplifiers, the noise floor of our vector network analyzer is so low ($P_A \approx -114$ dBm) that only for extremely small Δf the SNR is limited by P_A.

For a typical cavity output coupling of $\kappa_2/2\pi \approx 0.5$ MHz, Eq. (3.9) shows we can achieve a single photon SNR of 0 dB within 0.1 µs. These fast measurement times illustrate the advantage of circuit QED over traditional DC measurement techniques for electrons on helium.

3.6 Filtering of DC electrodes

Noise on the bias electrodes distorts the dot's electrostatic potential and thus leads to electron dephasing (see section 1.3.2). The most common source of noise is the voltage source itself, but electrical pick-up, ground loops and Johnson noise are also often encountered. Since most of these types have a $1/f$-like dependence, filters with a low corner frequency are key to minimizing electron dephasing.

An effective low-pass filter only passes low frequency signals below f_c and rejects all other frequencies. Since it is difficult to find a single filter that rejects frequencies from f_c to well above 10 GHz, we designed and used three separate filters with complementary rejection bands in series. The first two stages are combined on a custom designed printed circuit board, which is situated in a copper enclosure (Fig. 3.8a) filled with Eccosorb CR117. The PCB contains pairs of long meandering traces (similar to Ref. [68]) to increase the effective contact length with the lossy ferrite, and RC-filters with cut-off frequencies $f_c \approx (2\pi\sqrt{R_1 R_2 C_1 C_2})^{-1}$ in the range 2-400 Hz (Fig. 3.8b). The cut-off frequency for each electrode is chosen based on the voltage sweep rate for each electrode. The final filter (Minicircuits ZX75LP-30+, rejection band 30-3000 MHz) cancels self-resonances from the surface mount resistors and capacitors, which typically have resonances in the regime 1-100 MHz.

The total room temperature transmission of a cascaded filter circuit is shown in Fig. 3.8c. At frequencies below 10 kHz an RC-filter with $f_c = 320$ Hz shows the expected roll-off. The uptake in transmission past 10 MHz can be explained via the self-resonances of the surface mount components, which unfortunately are only weakly attenuated by the Minicircuits filter. For frequencies above 1 GHz the eccosorb is an extremely effective absorber and the

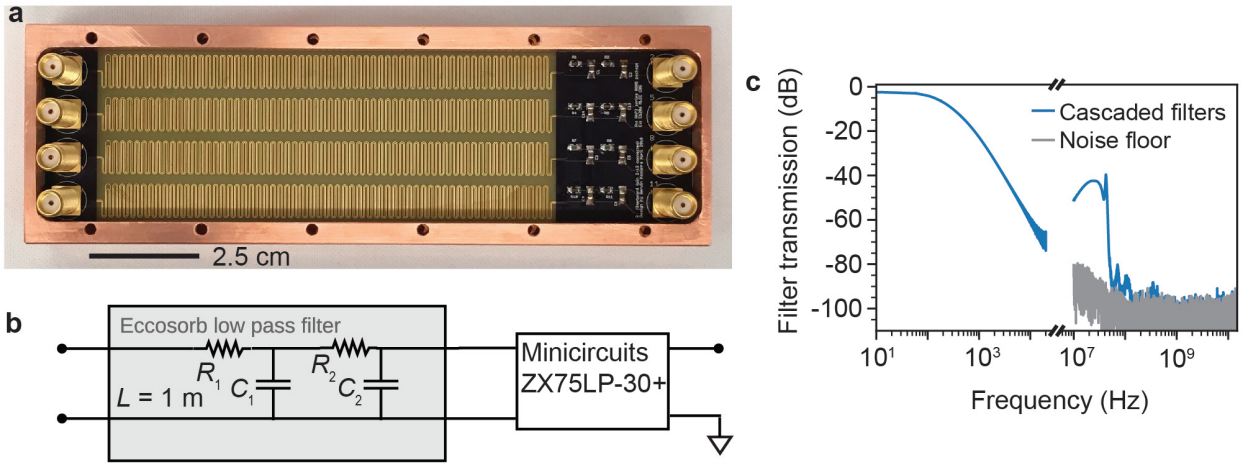

Figure 3.8: Cryogenic low-pass filters for DC electrodes near the dot (a) DC filtering test board mounted in copper enclosure for thermalization and shielding, before it is filled with Eccosorb. (b) Schematic of the three cascaded DC filters (i.e. eccosorb filter, RC-filter and Minicircuits π-filter) used to attenuate high-frequency voltage noise on each bias electrode. (c) Measured transmission through the cascaded filter circuit shown in (b). The transmission from 10 Hz - 10 kHz was measured using the NI 9260 DAQ, whereas the transmission from 100 MHz - 10 GHz was obtained using a network analyzer. We were not able to obtain the transmission from 10 kHz - 10 MHz.

transmission is below the noise floor.

CHAPTER 4

TRAPPING A SINGLE ELECTRON ON HELIUM USING A SUPERCONDUCTING RESONATOR

In this chapter we experimentally realize the coupling of a single electron and Wigner molecules on helium to a microwave cavity, which serves as an electron detector and harbors an electron reservoir. We transfer electrons from the reservoir to a small island where we control the charge with single electron resolution, and perform spectroscopy of a single electron and few-electron Wigner molecules. We observe unique spectra which allow us to identify different molecules, and a large electron-photon coupling. These results open the door to coherent control of the orbital and spin state of Wigner molecules on helium.

At the heart of our circuit QED platform lies a superconducting microwave resonator, which is shown in Fig. 4.1a and was first introduced in section 2.2. This coplanar stripline resonator consists of two niobium center pins, which are joined at one end (Fig. 4.1b) and are situated below the ground plane at the bottom of a micro-channel (width $w = 3.5$ µm, and depth $d_0 \approx 1.2$ µm). In the absence of helium and electrons, the differential mode has a resonance frequency $f_0 = 6.44$ GHz, linewidth $\kappa_{\rm tot}/2\pi = 0.4$ MHz, and a strongly concentrated RF electric field in between the two center pins suitable for coupling to single electrons.

4.1 Helium dynamics

The resonator can be used as a sensitive probe of the liquid helium in the micro-channel, since the presence of liquid helium disturbs the dielectric environment seen by the resonator. Before depositing electrons, we operate the resonator as a liquid helium level meter and characterize the filling behavior in the micro-channel with a transmitted microwave tone.

The measured resonance frequency shift as function of added helium reveals four different filling regimes (Fig. 4.2). In region I, a ∼30 nm Vanderwaals film covers the entire sample

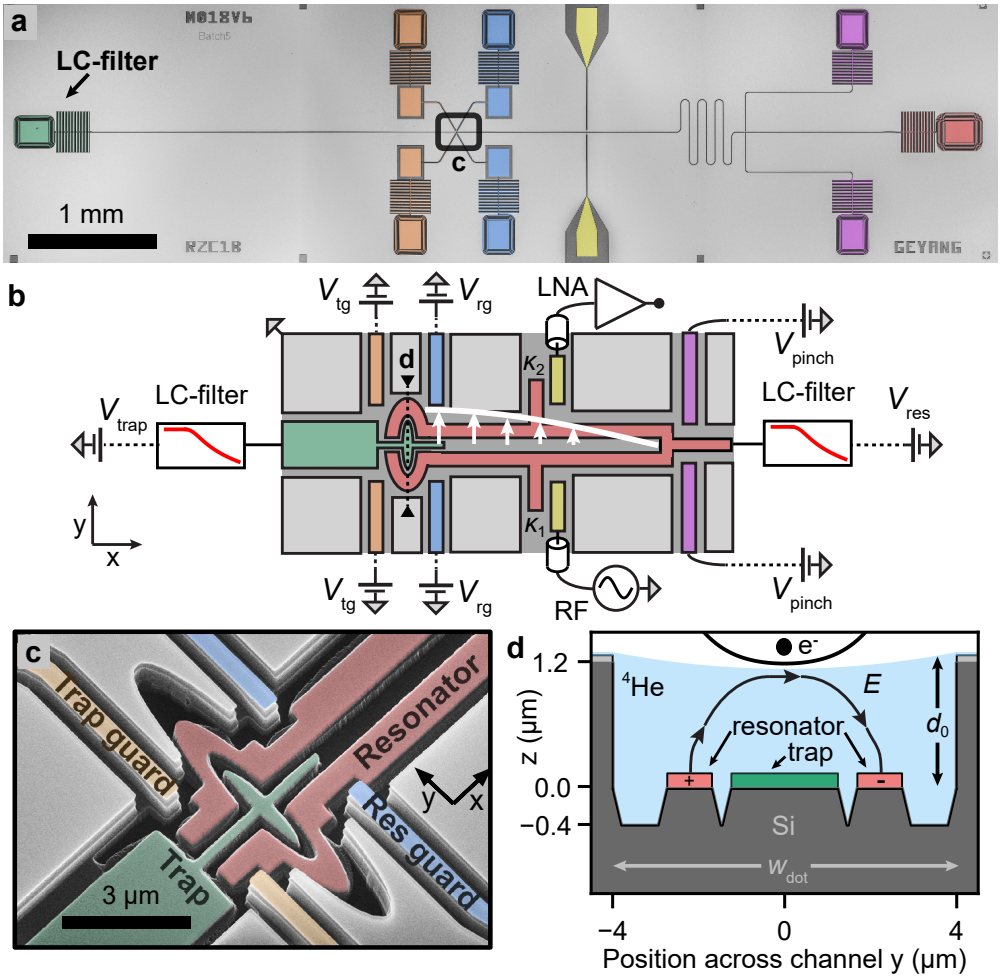

Figure 4.1: An electron-on-helium dot (a) Optical micrograph and (b) schematic of the device. The resonator (red) can be probed with an RF tone via coplanar waveguides (yellow) that couple (decay rates $\kappa_{1,2}$) to the microwave resonator. The white arrows show the electric field of the $\lambda/4$ microwave mode at the center of the channel. The transmission is amplified with a low-noise amplifier (LNA). The electrostatic potential for electrons is controlled with additional electrodes, which are all equipped with individual low-pass filters to reject noise at the resonance frequency [64] . In (b), we only show these filters for the trap and resonator. (c) Tilted, false-colored scanning electron micrograph of the dot showing the micro-machined silicon substrate. The fabrication recipe for this device can be found in Appendix A. The resonator (red) and trap electrode (green) are located on the bottom of a micro-channel, which lies 1.2 µm below the level of the resonator guards (blue), trap guards (orange) and ground plane. (d) Schematic cross-section of the dot shown in (c), depicting the resonator center pins and trap electrode submersed in liquid helium. Wigner molecules are trapped on the interface of liquid ^{4}He and vacuum by the electrostatic potential (solid black line) generated by electrodes near the dot. The electron orbital state couples to the transverse microwave electric field E from the resonator.

cell, resulting in only a small frequency shift. Next, a large frequency shift heralds the second filling regime where liquid helium fills the channel according to Jurin's law

$$\rho g h = \frac{\sigma}{R}. \tag{4.1}$$

Here, h is the vertical distance from the helium in the cylindrical reservoir to the chip, $\rho = 145$ kg/m^3 is the density of liquid helium, $\sigma = 3.78 \cdot 10^{-4}$ N/m^2 is the surface tension and R is the radius of curvature of the helium-vacuum interface. From 30 to 110 puffs, the helium thickness is given by

$$t_{\mathrm{He}} = d_0 - \frac{\rho g h}{2\sigma}\frac{w^2}{4} \tag{4.2}$$

and barely increases from 1.0 to 1.2 µm, which explains the observed resonance frequency plateau. Beyond 110 puffs, the channel overflows and the frequency continues to shift downwards (region III), until helium fills the entire mode volume of the resonator (region IV).

To study the stability of the helium surface in the micro-channel, we repeatedly measure the resonance frequency shift at each point along the curve of Fig. 4.2a. The standard deviation of these repeated measurements is a measure of both the resonator's sensitivity to changes in helium level and of helium surface vibrations. The sensitivity of the resonator is greatest at the transition from region I to region II, which explains the large spike in Fig. 4.2b, and decreases slowly to zero in region IV. Therefore, the smaller standard deviation observed in region II compared with region III points to a more stable helium surface, explained by the stabilizing effect of the capillary filling [58]. Since helium vibrations induce electron dephasing, liquid helium behaves best as a substrate for electrons in region II. Therefore, all measurements below are performed at the black arrow in Fig. 4.2b.

To further quantify the helium vibrations at this filling level, we monitor the resonance frequency as function of time. We observe periodic oscillations with dominant frequencies below 10 Hz (Fig. 4.3a,b). From the helium-resonator coupling $\partial f_0/\partial t_{\mathrm{He}} = 5$ kHz/nm and the integrated spectral density (6.8 kHz) we estimate the magnitude of classical helium fluc-

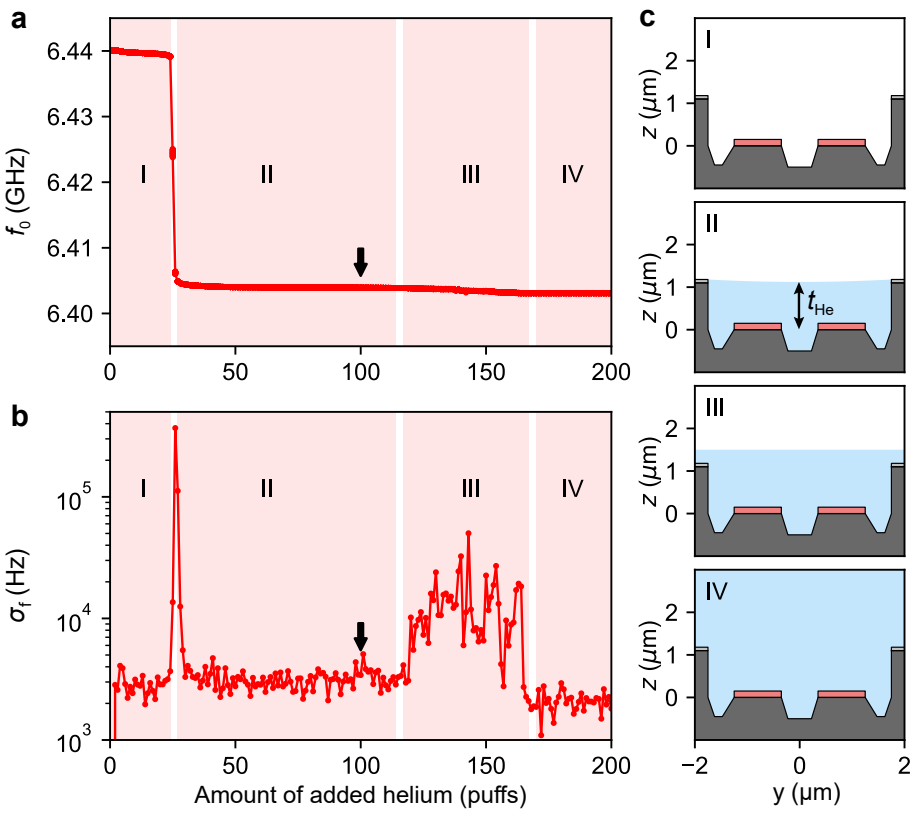

Figure 4.2: Using the microwave resonator as a sensitive probe for liquid helium inside the micro-channel (a) Resonance frequency f_0 and (b) resonance frequency jitter σ_f as function of the number of ^{4}He gas puffs introduced to the sample cell. One puff corresponds to approximately 25 cc of ^{4}He gas at STP. The experiments in this chapter are performed at the black arrow (100 puffs), where liquid helium has an appropriate thickness and forms a stable electron substrate. (c) Schematics of the channel showing the helium level (light blue) in each of the four regions denoted in (a) and (b). For a detailed description see the main text.

tuations to be $\Delta t_{\mathrm{He}} = 1.4$ nm. The resonator frequency fluctuations due to these vibrations increases by a factor of five when reservoir electrons are present (Fig. 4.3c) because electrons couple more strongly to the resonator than helium.

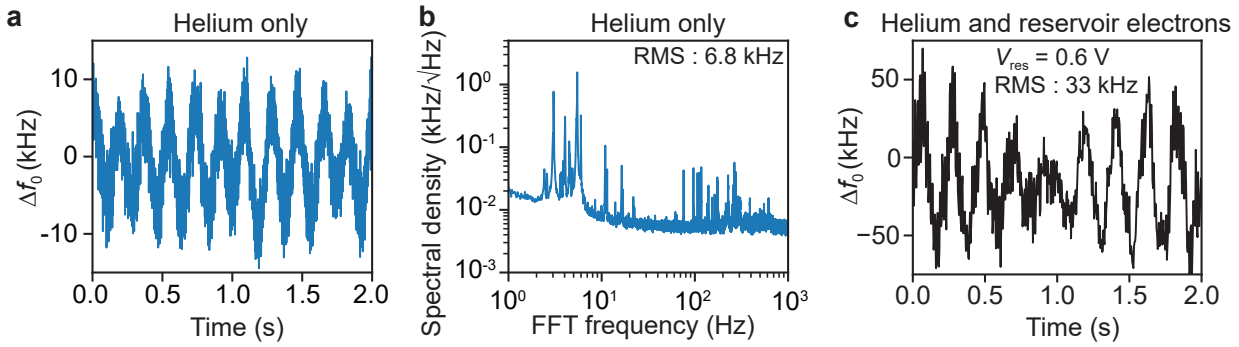

Figure 4.3: (a) Resonance frequency jitter due to helium vibrations measured at $T = 25$ mK without reservoir electrons. (b) Most of the spectral density for the data in (a) lies below 10 Hz. Nearly all of the resonance frequencies in this region can be associated with a multiple of 1.4 Hz, the frequency of the pulse tube refrigerator. The quality factor of these modes are at least a few hundred. (c) After depositing reservoir electrons the frequency jitter increases. Note the difference in scale compared with (a). All time traces are taken with a microwave tone on resonance and converting the phase fluctuations to resonance frequency fluctuations using the resonator linewidth κ_{tot}.

Even though the magnitude of the jitter is less than a resonator linewidth $\kappa_{\mathrm{tot}} = 0.4$ MHz, the variation of the resonance frequency shift over time obscures small frequency shifts due to electrons near the dot. To circumvent the issue of the resonator jitter, we sweep the trap or guard voltages at a rate much faster than the dominant helium vibration frequency, such that frequency shifts from electrons in the dot become quickly apparent after averaging.

4.2 Isolating electrons from the reservoir

We deposit electrons over the resonator through thermal emission from a tungsten filament situated above the chip, while applying a positive voltage to the resonator DC bias electrode and a negative bias voltage to the filament. We detect the deposited electrons as a dispersive resonance frequency shift that depends strongly on the resonator bias voltage V_{res} (Fig. 4.4a) and the number of electrons on the resonator [57]. For the experiments presented hereafter,

we fix V_{res} at 0.6 V such that electrons on the resonator can be treated as a reservoir with constant electron density. Furthermore, our measurements are performed at $T = 25$ mK and low incident microwave power ($n_{\mathrm{ph}} \approx 5$) such that electrons respond linearly to the resonator's driving force.

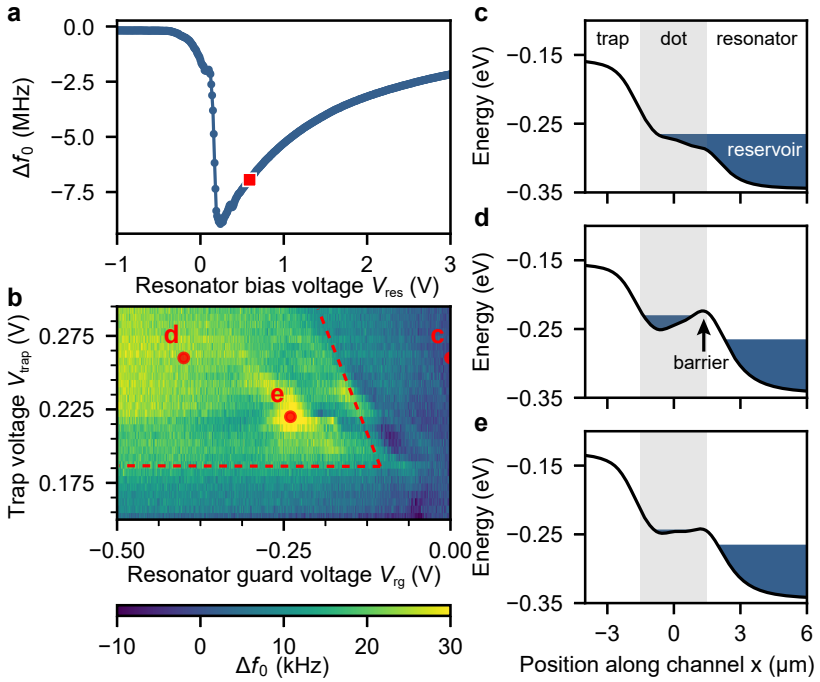

Figure 4.4: Separating electrons from the reservoir. (a) At $T = 25$ mK reservoir electrons are detected through a dispersive resonance frequency shift which depends on V_{res}. According to Eq. (2.8), the jump in Δf_0 at $V_{\mathrm{res}} \approx 0.18$ V signals electron loss from an ensemble with density $n \approx 9 \times 10^{12}$ m^{-2}. The data presented hereafter are taken with the resonator bias voltage fixed at 0.6 V, which is marked by a square. (b) Measured resonance frequency shift while raising a barrier between the dot and reservoir as function of V_{trap}. The dashed line segments mark the border of a region where electrons can be trapped in the dot. The largest Δf_0 are expected when the electron orbital frequency approaches f_0. For $V_{\mathrm{trap}} > 0.3$ V electron trapping is unstable, because reservoir electrons can freely flow through the dot onto the trap electrode. (c)-(e) Simulated potential energy along the channel for three different values of V_{rg}, V_{trap}, marked by the red dots in (b). Reservoir electrons ($x > 2$ µm) and electrons in the dot (-1.5 µm $< x < 1.5$ µm) are represented as a constant energy (blue). Electrons are trapped in the dot in (d) and (e).

We use the dot in Fig. 4.1c to isolate individual electrons from the reservoir, which requires fine control over the electrostatic potential. We achieve this using three sets of electrodes near the tip of the resonator where the microwave electric field is strongest. The

size of the electrodes near the dot is much larger than in semiconducting quantum dots, because the unscreened electron interaction results in inter-electron distances exceeding 200 nm. With appropriate voltages applied to the electrodes, the smooth electrostatic potential (Fig. 4.4d,e) allows for trapping of electrons. Furthermore, due to the dot's oblong shape, the lateral motion of trapped electrons is primarily in the y-direction (see Fig. 4.1d), such that it couples to the transverse microwave field of the resonator.

To load the dot we use the trap electrode (Fig. 4.1c, green) to attract reservoir electrons towards the dot, and the resonator guard (blue) to create a barrier between the dot and reservoir. Only if the trap voltage is sufficiently positive, and the resonator guard is sufficiently negative can electrons be loaded and contained in the dot, respectively. When monitoring the resonance frequency shift Δf_0 in response to these two voltages, we only see significant signal in an area that is marked by two converging dashed lines in Fig. 4.4b. The dashed lines are obtained from simulation of the electrostatic potential near the dot (see Fig. 2.7), and indicate the presence of a barrier between reservoir electrons and electrons in the dot. Well within the predicted trapping region, we observe resonance frequency shifts that depend sensitively on V_{trap} and V_{rg}, indicating that trapped electrons in the dot interact with the resonator. The observed shift depends on the number of trapped electrons, which increases for a larger trap voltage, as well as the shape of the electrostatic potential.

4.3 Signatures of Wigner molecules

To deterministically populate the dot with N electrons, we partially unload the dot using the trap guard electrode (orange in Fig. 4.1c). A partial unload consists of briefly sweeping the trap guard voltage to $V_{\mathrm{unload}} < 0$, which decreases the trap depth (see Fig. 4.5a), followed by a measurement of the resonator transmission at $(V_{\mathrm{trap}}, V_{\mathrm{tg}}) = (0.175, 0.0)$ V. The plateaus in resonator transmission shown in Fig. 4.5b are reproduced after reloading the dot, but are absent when the dot is initially empty. Therefore, each plateau is associated with a constant number of trapped electrons, and the final change in transmission at $V_{\mathrm{unload}} = -0.305$ V

leaves the dot empty.

The sudden changes in transmission are consistent with single electrons leaving the dot. We show this by modeling the trap as an axially symmetric harmonic well in which the electron configurations can be calculated analytically [33, 69]. From the voltage at which the last electron escapes, we estimate unloading voltages for two, three and four electrons, using the effective trap curvature as the only free parameter (see Appendix B). Red arrows in Fig. 4.5b indicate these estimates, and agree within 3 mV with the plateau edges. This unloading method therefore allows us to deterministically populate the dot with one to four electrons.

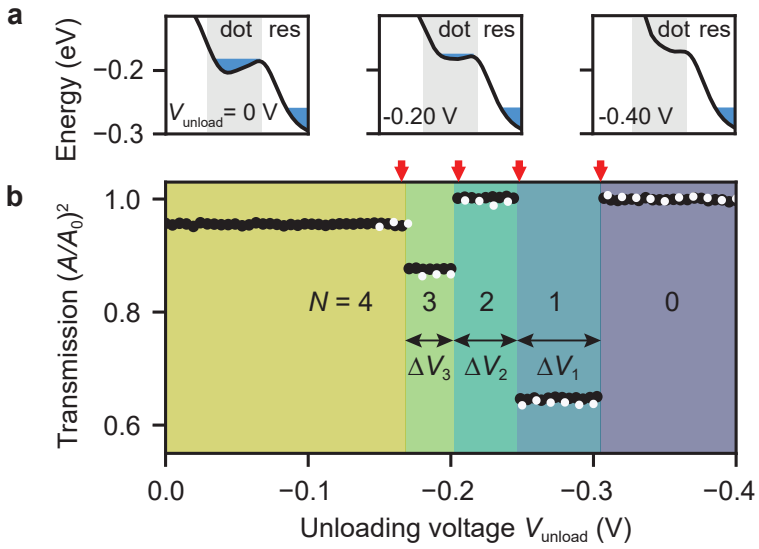

Figure 4.5: Unloading the dot. (a) Schematic of the unloading procedure. At the unloading voltage, the dot's trap depth decreases for more negative V_{unload}. No electrons can occupy the dot at $V_{\mathrm{trap}} = -0.4$V. (b) With decreasing V_{unload}, sudden changes in the resonator transmission (black dots, measured at $V_{\mathrm{trap}} = 0.175$ V and $V_{\mathrm{tg}} = 0$ V and averaged 500 times) indicate that electrons leave the dot. We observe five distinct plateaus that are reproduced after reloading the dot eight hours later (white dots), and are associated with a constant number of trapped electrons N. Red arrows indicate predicted escape voltages for $N = 4$ to 1 electrons (left to right) from a single-parameter model, see Appendix B.

The increasing length of transmission plateaus ΔV_N with decreasing N is a telltale sign of strong electron interactions [70, 71], which originate from an unscreened interaction potential on liquid helium [32]. The ratio of kinetic energy $k_B T$ to interaction energy U as well as

confinement strength $\bar{n}$, quantify electron interaction strength and wavefunction overlap, and predict the formation of Wigner molecules for $\Gamma_c^{-1} = k_B T_c/U \lesssim 1/137$ and $\bar{n}_c \lesssim 1/37$ [34, 35]. Since our experiment operates in the low-temperature ($\Gamma^{-1}/\Gamma_c^{-1} \approx 9$), low-confinement regime ($\bar{n}/\bar{n}_c \approx 3$), the irregular step size signals the presence of Wigner molecules inside the dot.

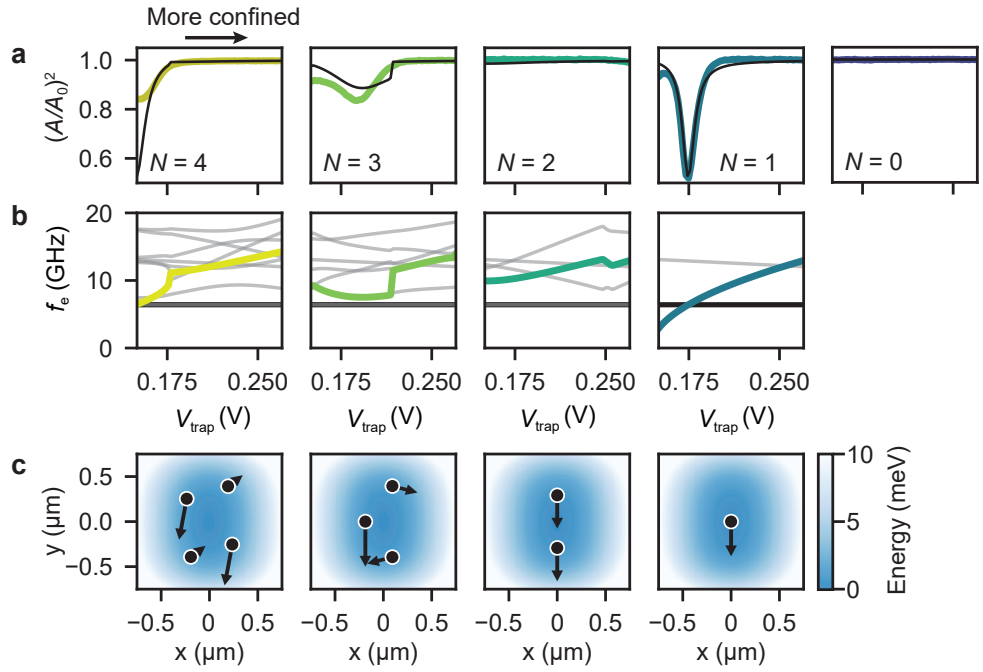

Figure 4.6: (a) Resonator transmission spectra of Wigner molecules consisting of up to four electrons, measured by varying the trap curvature using V_{trap}. Below $V_{\text{trap}} = 0.15$ V electron trapping is unstable. The solid black lines are simulated cavity responses and agree qualitatively with the measured spectra. The discontinuity in the simulation for $N = 3$ is due to a sudden change in position of the electrons, and is not expected to be visible in the averaged data. (b) Simulated orbital frequencies associated with the simulated cavity responses in (a). The strongest coupled electron eigenmode is highlighted and more weakly coupled eigenmodes are shown in gray. For $N = 1$, the crossing of the electron orbital frequency with the resonator explains the large measured signal in (a). (c) Simulated electron configurations in the approximated electrostatic potential, shown for $V_{\text{trap}} = 0.175$ V. The arrows show the electron motion for the eigenmode that is most strongly coupled to the resonator. The microwave electric field is in the y-direction.

While a Wigner molecule is trapped in the dot, we use the resonator to observe it's unique spectrum, which provides insight in the electron configurations and orbital frequencies. We perform spectroscopy by monitoring the resonator's transmission while varying the trap

voltage, which deforms the trap and therefore controls the orbital frequencies. For this measurement, a Wigner molecule can be trapped and studied for hours, since the trap depth is large compared to the zero-point energy and thermal energy. Fig. 4.6a shows five different spectroscopy traces, each corresponding to the different-sized Wigner molecules from Fig. 4.5b. To retrieve electron configurations and orbital frequencies, we numerically minimize the total energy of the ensemble and solve the coupled equations of motion (see Appendix C). The electron configurations (Fig. 4.6c) change significantly as electrons are added or removed from the dot, and show correlated electron motion, originating from strong electron interactions. The largest signal in Fig. 4.6a occurs for a single electron at $V_{\mathrm{trap}} = 0.175$ V when its orbital frequency f_e is resonant with the resonator (Fig. 4.6b). In our model, the orbital frequency of larger Wigner molecules remains detuned for all V_{trap}, which is due to a strong anharmonic component in the electrostatic potential. From the quartic term in this potential, we estimate a single-electron anharmonicity of 85 MHz (section 2.3.3), which holds promise for creating an electron-on-helium orbital state qubit.

4.4 Properties of a single electron in the dot

We now focus on a single trapped electron and investigate its properties by tuning the orbital frequency into resonance with the resonator. Fig. 4.7a shows a crossing of the orbital frequency with the resonator around $V_{\mathrm{trap}} = 0.184$ V, which is accompanied by a rapid change in Δf_0 (Fig. 4.7c). By fitting the measured frequency shift to a model, which takes into account one orbital mode coupled to a single resonator mode [52], we obtain a single-electron-photon coupling strength $g = 2\pi \times (4.8 \pm 0.3)$ MHz and electron linewidth $\gamma = \gamma_1/2 + \gamma_\varphi = 2\pi \times (77 \pm 19)$ MHz. The coupling strength is large compared to the resonator linewidth ($\kappa/2\pi \approx 0.5$ MHz), indicating that each photon measures the presence of the electron, and the coupling is similar to that measured in semiconducting quantum dot circuit QED architectures [55]. In addition, our estimate of the anharmonicity (see Fig. 2.9) is similar to that in superconducting qubits, indicating that with a reduced linewidth the

orbital state of a single electron on helium can be used as a qubit.

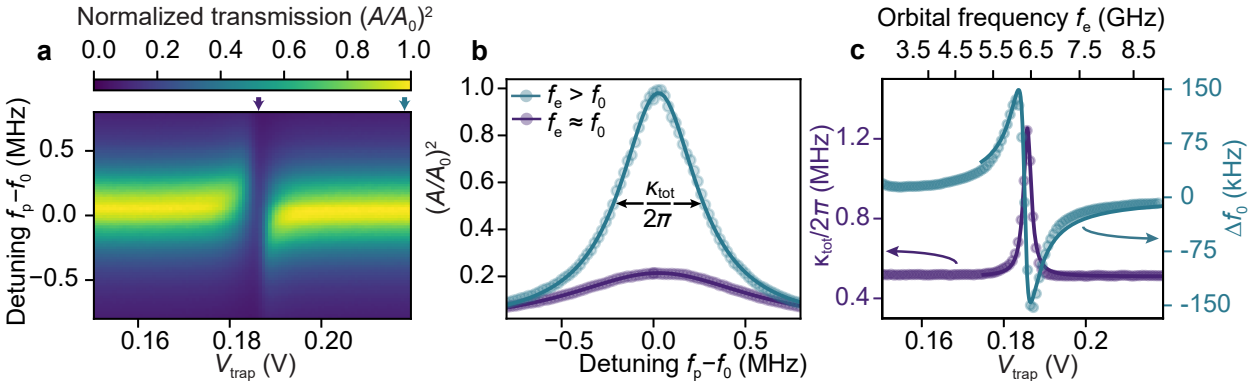

Figure 4.7: Single electron resonator spectroscopy. (a) Normalized transmission amplitude as function of trap voltage and microwave probe detuning $f_p - f_0$. (b) Resonator spectra for two values of V_{trap}, indicated by arrows on the horizontal axis in (a). For $V_{\text{trap}} = 0.184$ V (0.23 V) the electron is on (off) resonance with the cavity. The resonant trace illustrates the sensitivity of our device to a single electron. (c) Resonance frequency shift (right axis) and resonator decay rate (left axis) obtained by fitting the Lorentzian resonator spectra from (a). The solid line is a fit to a model that yields a coupling strength near resonance of $g/2\pi = 4.8 \pm 0.3$ MHz and total electron linewidth $\gamma/2\pi = 77 \pm 19$ MHz. The top horizontal axis displays how the electron orbital frequency varies as function of V_{trap}, and shows a crossing with the resonator ($f_e = 6.4$ GHz) at $V_{\text{trap}} = 0.184$ V.

The total linewidth γ is three orders of magnitude larger than expected from the electron-phonon coupling in ^{4}He and charge noise from the bias electrodes, respectively ($\gamma/2\pi < 0.1$ MHz) [28]. We identify the dominant source of excess noise as classical helium fluctuations in the dot, caused by the pulse tube refrigerator. This is corroborated by a measurement of the crossing voltage as function of time, which shows spectral features of the pulse tube refrigerator (see Fig. 4.8). To estimate the dephasing rate due to helium fluctuations, we estimate an electron's sensitivity to helium fluctuations from electrostatic simulations ($\partial f_e/\partial t_{\text{He}} \approx 80$ MHz/nm) and independently measure helium fluctuations ($\Delta t_{\text{He}} \approx 1.4$ nm), yielding $\gamma_\varphi/2\pi \approx 110$ MHz. Therefore, we expect the single electron linewidth to be limited by dephasing due to helium level fluctuations.

4.5 Evidence of a helium-limited linewidth

We verify the hypothesis that the single electron linewidth is limited by helium vibrations by quickly and repeatedly bringing the electron in and out of resonance. If there were no electron dephasing, the crossing voltage would be constant each time the electron is brought into resonance. However, Fig. 4.8a,b clearly shows a spread in crossing voltages of $\Delta V^*_{\mathrm{trap}} = 0.3$ mV, from which we predict a dephasing

$$\gamma/2\pi = 2\sqrt{2\ln 2}\frac{\partial f_e}{\partial V_{\mathrm{trap}}}\Delta V^*_{\mathrm{trap}} = 67\,\mathrm{MHz}, \tag{4.3}$$

which is consistent with the measured single electron linewidth $\gamma_\varphi/2\pi = (77 \pm 19)$ MHz from Fig. 4.7. Moreover, the spectrum of crossing voltages (Fig. 4.8c) contains multiples of the characteristic pulse tube frequency (1.4 Hz). Therefore, we conclude that the single electron linewidth is limited by dephasing due to helium vibrations originating from the pulse tube.

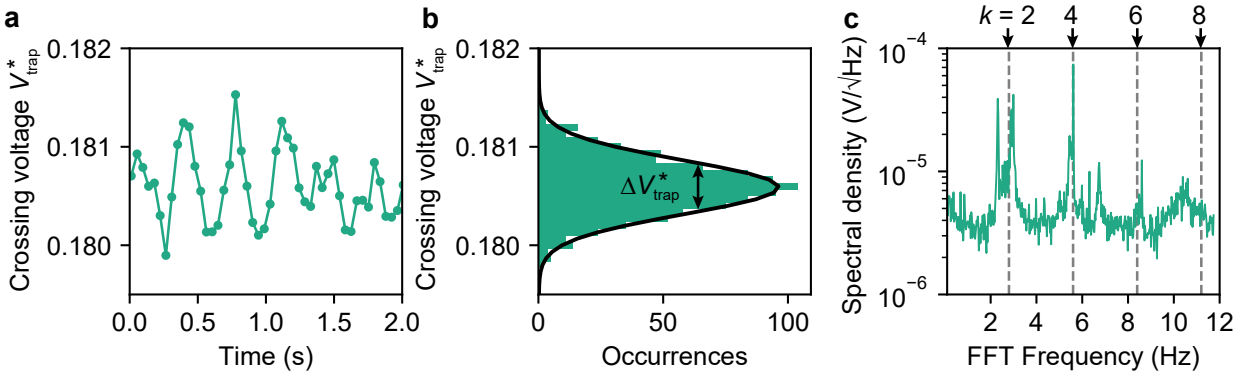

Figure 4.8: Quick and repeated measurements of the crossing voltage of a single electron. (a) After loading a single electron we repeatedly sweep the electron in and out of resonance while recording the resonator transmission. The crossing voltage as function of time is found by fitting to the location of the minima in the measured resonator transmission. (b) Statistics of 10^3 crossings with the resonator. The solid black line is a Gaussian fit with standard deviation $\Delta V^*_{\mathrm{trap}} = 0.28$ mV. (c) Fourier transform of the crossing voltage time series. The dashed lines at $f_k = 1.4\,k$ Hz with $k = 2, 4, 6, 8$ indicate multiples of the pulse tube refrigerator frequency and align with peaks in the crossing spectrum. The maximum FFT frequency is set by the sweep time needed to bring the electron in and out of resonance (45 ms), which in turn is limited by the corner frequency of the RC filter, the number of measurement points and the re-trigger time of the PNAX.

If the helium surface vibrates more slowly than the measurement time of Fig. 4.8a, it should be possible to manually align the resonator transmission spectra to find the electron linewidth in the absence of helium vibrations. We did not observe a decrease in linewidth after refocussing the transmission spectra, possibly because helium vibrations with higher frequencies limit the linewidth on the timescale of the sweep time. By increasing the corner frequency of the RC filter of the trap electrode, it may be possible to measure the crossing voltage fast enough to find the linewidth in the absence of vibrations.

4.6 Additional contributions to the electron linewidth

Besides helium vibrations, the electron linewidth is also broadened due to deleterious effects of voltage noise and the presence of the electron reservoir. Taking into account the RC-filters and the dot geometry allows for a more accurate estimate than in section 1.3.2 or Ref. [28], and shows that both these contributions are smaller than the contribution due to helium vibrations.

4.6.1 Voltage noise from the bias electrodes

The linewidth due to voltage noise depends on the magnitude of the noise, which is reduced due to an RC filter on each bias electrode, and the electron's sensitivity to voltage noise from each electrode $\partial f_e/\partial V_i$. We determine the sensitivities from simulation of the electron frequency near the resonant condition and they are summarized in Table 4.1. The large slope associated with the trap electrode indicates f_e can be tuned over a large range with a small trap voltage, but also makes a single electron very vulnerable to noise on the trap electrode. However, due to the low corner frequency of the RC filter ($f_{3\mathrm{dB}} \approx 300$ Hz) we estimate only 5 µV of noise on each electrode, such that the estimated linewidth, determined by adding

the contributions in quadrature

$$\frac{\gamma_\varphi^{\text{noise}}}{2\pi} = \sqrt{\sum_i \left(\frac{\partial f_e}{\partial V_i}\right)^2 \Delta V_i^2}, \tag{4.4}$$

should not exceed 1 MHz.

Table 4.1: Effect of voltage noise on the electron orbital frequency f_e and the resulting contribution to the single electron linewidth $\gamma_\varphi^i/2\pi$, assuming a voltage noise on each electrode of $\Delta V_i = 5$ µV. The relative magnitudes of the simulated slopes $\partial f_e/\partial V_i$ are equal to the ratio of electrode lever arms, shown in Fig. 2.8a (the expected electron position is $x = -0.5$ µm).

Electrode i	$\partial f_e/\partial V_i$ (GHz/V)	$\gamma_\varphi^i/2\pi$ (MHz)
Resonator	-48	0.2
Trap	95	0.5
Resonator guard	-7	<0.1
Trap guard	-11	<0.1
Total		0.5

4.6.2 Helium vibrations on the resonator

Reservoir electrons above the resonator form a capacitor with the image charges induced in the resonator electrode below and fluctuations in the helium level Δt_{He} modulate the capacitance C_{res} of the electron reservoir. Since the resonator electrode also extends into the dot area, fluctuating image currents caused by the fluctuating capacitance cause single electron decoherence.

The capacitance of the sheet of electrons above the resonator can be approximated by a parallel plate capacitance: $C_{\text{res}} = \varepsilon_0 \varepsilon_{\text{He}} A/t_{\text{He}}$, where t_{He} is the height of the electrons above the electrode, and A the area of the electron reservoir. A change in the helium thickness causes a change in the capacitance

$$\Delta C_{\text{res}} = -\frac{C_{\text{res}}}{t_{\text{He}}} \Delta t_{\text{He}}. \tag{4.5}$$

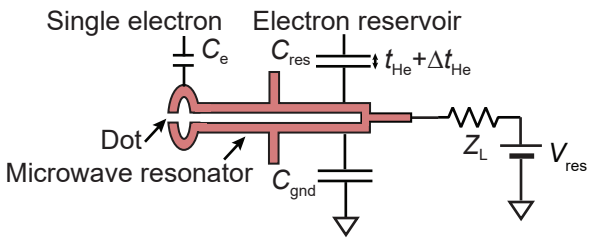

Figure 4.9: Electrical schematic used to calculate the effect of a fluctuating electron reservoir on a single electron. The reservoir is represented by the capacitor $C_{\rm res}$, which fluctuates due to classical helium fluctuations $\Delta t_{\rm He}$. The resonator electrode is biased using a voltage source, which is hooked up to the electrode with leads that have impedance Z_L. This impedance also includes the bias source output impedance and filters.

The effect of $\Delta C_{\rm res}$ on a single electron depends on the value of Z_L (Fig. 4.9), which includes the output impedance of the voltage source and the line impedance. If $Z_L \to \infty$, the resonator potential is floating and fluctuating image currents do not dissipate via the leads but dissipate entirely via the capacitors. An estimate of the single-electron linewidth assuming $Z_L \to \infty$ therefore gives an upper limit for the dephasing due to reservoir fluctuations.

If the helium thickness fluctuations are quasi-static and $Z_L \to \infty$, a small fluctuation in capacitance results in voltage noise on the resonator electrode via $V = Q/C_{\rm tot}$, such that the voltage noise $\Delta V_{\rm res}$ is given by:

$$\Delta V_{\rm res} = -\frac{V_{\rm res}}{C_{\rm tot}} \Delta C_{\rm res} = \frac{V_{\rm res}}{t_{\rm He}} \frac{C_{\rm res}}{C_{\rm tot}} \Delta t_{\rm He}. \tag{4.6}$$

In Eq. (4.6) we define the total capacitance of the resonator electrode $C_{\rm tot} \approx C_{\rm res} + C_{\rm gnd}$ and have assumed that (i) the capacitance to the single electron C_e is negligible and (ii) $C_{\rm gnd}$ is approximately constant with $t_{\rm He}$. The ratio $C_{\rm res}/C_{\rm tot}$ equals the resonator electrode lever arm at the location of the electron reservoir, and is approximately 0.6 from electrostatic simulations (see Fig. 2.8a).

Finally, using Eq. (4.6), we estimate the dephasing from the electron sensitivity to the

resonator electrode:

$$\frac{\gamma_\varphi^{\mathrm{res}}}{2\pi} = \left|\frac{\partial f_e}{\partial V_{\mathrm{res}}}\right| \Delta V_{\mathrm{res}} = \left|\frac{\partial f_e}{\partial V_{\mathrm{res}}}\right| \frac{V_{\mathrm{res}}}{t_{\mathrm{He}}} \frac{C_{\mathrm{res}}}{C_{\mathrm{tot}}} \Delta t_{\mathrm{He}} \tag{4.7}$$

With $\Delta t_{\mathrm{He}} = 1.4$ nm, $t_{\mathrm{He}} = 1.2$ µm, $V_{\mathrm{res}} = 0.6$ V and $\partial f_e/\partial V_{\mathrm{res}}$ from Table 4.1, we estimate an upper limit for the single-electron linewidth $\gamma_\varphi^{\mathrm{res}}/2\pi \approx 20$ MHz. Furthermore, we assume there are no electrons on the trap, resonator guards or trap guards, such that a similar calculation for these electrodes does not result in additional dephasing. In a future device, this source of dephasing can be completely eliminated by removing the reservoir electrons or using an additional reservoir that does not couple to the resonator.

4.7 Towards strong coupling

Reducing the linewidth and increasing the coupling strength offers a path towards the strong coupling regime, which has recently been achieved for the cyclotron motion of electron ensembles on liquid helium [46]. In the strong coupling regime, direct measurement of the single electron and Wigner molecule orbital frequencies using two-tone spectroscopy [72] may bring to light new microwave features of strongly correlated electron states [73]. Since the orbital frequencies span tens of GHz (see Fig. 4.6b) this measurement would benefit from a frequency tunable microwave resonator [49, 74–77], a feature that can be embedded in a future device.

To reduce the linewidth, the pulse tube, which excites the helium surface, can be turned off for a short period of time without noticeable heating of the mixing chamber plate. However, turning off the pulse tube has not resulted in a smaller linewidth, because the ringdown time of surface vibrations at $T = 20$ mK is tens of seconds (see Appendix D). At temperatures above $T \approx 0.3$ K the ringdown time decreases as T^{-4} [78] due to damping from the normal component in ^{4}He. However, operating the experiment at elevated temperatures is unfeasible, since thermal excitations also broaden the electron transition (Fig. 4.10).

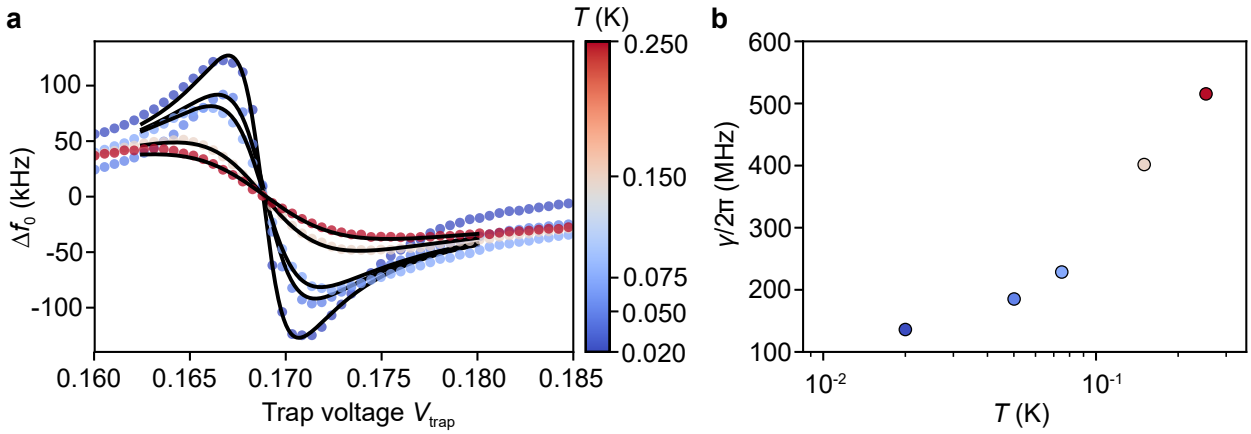

Figure 4.10: Resonator spectroscopy as function of temperature. (a) Single electron resonator spectroscopy for $T = 20$ mK (blue), 50, 75, 150 and 250 mK (red). (b) Fits to the single-electron resonator spectroscopy with fixed $g/2\pi$, show an increased linewidth $\gamma/2\pi$ with increased temperature. Over the same temperature range helium fluctuations remain constant and the Q of the superconducting Nb resonator is hardly affected, such that the increased linewidth must be due to increased thermal occupancy of the excited state of the single electron.

In an effort to dampen superfluid vibrations more quickly without heating the electron, we have added small amounts of ^{3}He to the sample cell. Due to a larger zero-point motion ^{3}He atoms uniformly coat the surface of the ^{3}He-^{4}He substrate and its non-zero viscosity should dampen surface vibrations [24, 79]. For ^{3}He concentrations of 500 ppm, the substrate is coated in multiple monolayers of ^{3}He atoms, but we have not observed a decrease in electron linewidth. For higher concentrations, we were unable to trap reservoir electrons due to unexpected electron loss events.

A promising approach to decreasing the linewidth is via passive vibration isolation of the sample cell at the mixing chamber, or via active noise cancellation of the sample cell or the helium surface (see section 5.4). Both methods are challenging because the fill line and microwave cables are rigid connections that transmit vibrations effectively. In addition, passive vibration isolation of low-frequency vibrations requires long extended springs where space is limited [80], and active noise cancelation suffers from reduced piezo travel distance at temperatures below 4 K.

The most promising approach to reaching the strong coupling regime is to design a dot

insensitive to helium vibrations ($\partial f_e/\partial t_{\mathrm{He}} = 0$). A preliminary design of a dot with a single electrode on the bottom of the micro-channel shows a hundredfold reduction in linewidth, although this comes at the expense of a smaller trap depth (see section 2.3.1). Such a dot combined with a microwave resonator made of a high kinetic inductance superconductor, which can enhance the coupling strength by more than three times via an increased characteristic impedance [43, 48], could allow for circuit QED with a single electron on helium in the strong coupling regime.

In conclusion, we have integrated an electron-on-helium dot with a superconducting microwave resonator and observed distinct resonator spectra of Wigner molecules consisting of up to four electrons. The large anharmonicity and coupling strength of a single electron on helium hold promise for creating an electron-on-helium qubit, which can be readily integrated with superconducting qubits while leveraging established protocols. Finally, when combined with a magnetic field gradient, the orbital state offers a clear path towards control of single electron and Wigner molecule spin states.

CHAPTER 5

COUNTERACTING VIBRATIONS OF THE LIQUID HELIUM SURFACE

Superfluid helium is host to many long-lived elementary excitations which hold great promise as mechanical resonators [81–85]. Liquid helium can interact with electromagnetic fields via a dielectrophoretic force, which attracts liquid helium towards locations where the modulus of the electric field is maximum, similar to the trapping force on a dielectric particle from an optical tweezer. This coupling is the main ingredient in superfluid helium optomechanics, which studies the mechanical properties of liquid helium using photons [82, 84, 86]. The same mechanism also allows for static control over the liquid helium film thickness, which can be used to tune optomechanical mode frequencies *in-situ* or control helium film thickness in ripplon studies on the helium surface [78, 87].

During experiments liquid helium is often subject to classical vibrations, which are due to external excitation of the experimental device (e.g. from the refrigerator itself or the laboratory environment) [57, 88]. Typically, at temperatures above 0.3 K the viscous damping in liquid helium is sufficient to attenuate these excitations in a reasonable timescale [78], such that experiments are minimally affected [86]. However, electron-on-helium qubits require temperatures below 0.1 K [28], where the liquid helium damping time exceeds minutes (appendix D) and classical fluctuations are the main source of dephasing, limiting the linewidth to tens of MHz (section 4.5). Stabilization of the liquid helium surface using the dielectrophoretic force could drastically reduce the linewidth of an electron on helium and greatly increase the measurement duty-cycle for superfluid optomechanics experiments.

In this chapter, we identify the pulse tube (PT) as the main source of vibrations inside the dilution refrigerator and measurements with a sub-pm/$\sqrt{\text{Hz}}$-sensitive helium level meter suggest that on-chip helium vibrations are caused by PT-induced vibrations in the off-chip helium reservoir. By applying only a moderate bias voltage to our helium level meter, we

can vary the helium thickness by more than the vibration amplitude. This allows us to actively cancel classical helium vibrations, which results in a fivefold reduction of on-chip RMS vibrations. If implemented with with electrons on helium, this technique could bring strong electron-photon coupling within reach.

5.1 Characterization of refrigerator vibrations

We first determine the cause of classical helium vibrations by measuring vibrations inside the refrigerator with a geophone, a device which produces a time-dependent voltage proportional to the speed of a small magnet suspended inside a coil. The voltage across the coil, caused by environmental vibrations which excite magnet motion, depends on the geophone's resonance frequency f_g, quality factor Q_g and coil's electrical properties. A measurement of the geophone's transfer function (Fig. 5.1b) calibrates these quantities and relates the measured output voltage to the magnet displacement. The transfer function is large around the geophone's resonance frequency f_g and from a fit we determine the geophone's essential properties, both at room temperature and $T = 20$ mK (Table 5.1). At cryogenic temperatures the quality factor decreases notably, which results in a reduced sensitivity

$$S(f) = \frac{Z_{12}\left(\frac{f}{f_g}\right)^2}{1-\left(\frac{f}{f_g}\right)^2+\frac{i}{Q_g}\frac{f}{f_g}}, \tag{5.1}$$

especially at frequencies below f_g (Fig. 5.1c). Because the displacement is inversely proportional to the sensitivity $d(f) = V_{\text{out}}(f)/2\pi f S(f)$, a reduced sensitivity produces a more noisy vibration spectrum at low frequencies, compared with room temperature.

During normal operation of the refrigerator, the geophone's vibration spectrum $d(f)$ shows a series of peaks at frequencies predicted by multiples of the natural pulse tube frequency ($f_k = 1.41\,k$ Hz, see Fig. 5.2b). The peaks disappear when the pulse tube (PT) is turned off and the root-mean-square (RMS) vibration amplitude decreases from

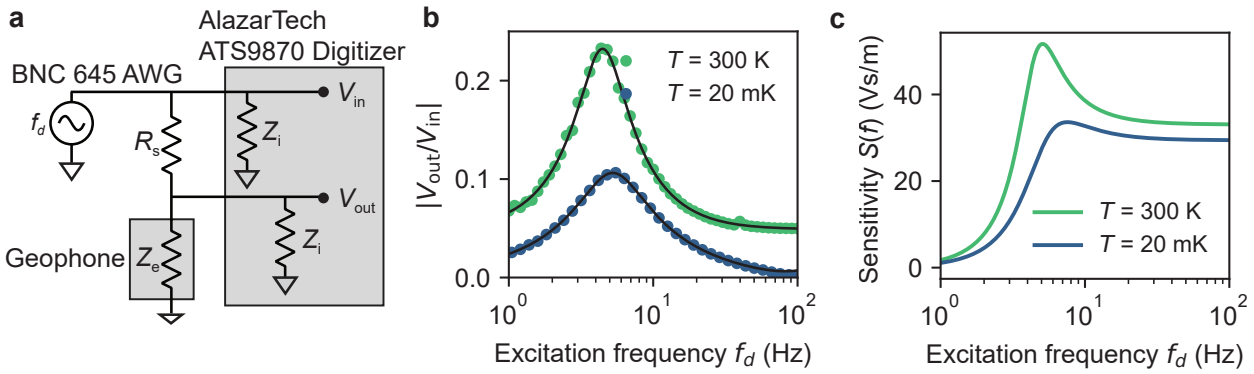

Figure 5.1: Calibration of the geophone inside a dilution refrigerator. (a) Electrical circuit used to calibrate the relevant parameters that determine the response of the geophone. The electrical circuit is driven by a sine wave of frequency f_d, and the geophone's transfer function is measured by recording V_{in} and V_{out} using a digitizer. In our circuit the series resistance is $R_s = 10$ kΩ, the input impedance of the digitizer is $Z_i = 1$ MΩ and Z_e is the geophone's impedance to be determined. (b) Transfer function of the geophone at $T = 300$ K (green dots) and $T = 20$ mK (blue dots). The solid lines represent fits to the theoretical response. (c) The fits allow for extraction of the sensitivity at room temperature (green) and cryogenic temperatures (blue). A slight decrease in sensitivity is observed at cryogenic temperatures.

Table 5.1: Comparison between geophone properties at room temperature and $T = 20$ mK. The parameters were extracted using the calibration method from Ref. [89].

	$T = 300$ K	$T = 20$ mK
Natural frequency f_g (Hz)	4.46	5.26
Quality factor Q_g	1.47	0.98
Impedance Z_{12} (Ω)	33.0	29.4
Transducer coil resistance R_T (Ω)	513	58
Coil inductance L_T (Ω)	0.03	0.15

$d_{\text{rms}} = 0.5$ µm to $d_{\text{rms}} = 0.2$ µm. The slope in the spectra is consistent with voltage noise with a $1/f$-like dependence and tends to exaggerate vibrations below $f_g \approx 5$ Hz. The prominent feature in both spectra at $f \approx 10$ Hz originates from building vibrations which are transmitted to the mixing chamber plate via the refrigerator frame. This was confirmed by a frequency shift after loading the frame with sandbags.

Since the PT must stay turned on for continuous cooling, it is important to minimize vibrations at the mixing chamber plate with the PT on. We identify three rigid connections inside the refrigerator responsible for transmitting vibrations from the PT to the mixing chamber plate. Firstly, since the cryostat is mounted on air bellows which deflate over time,

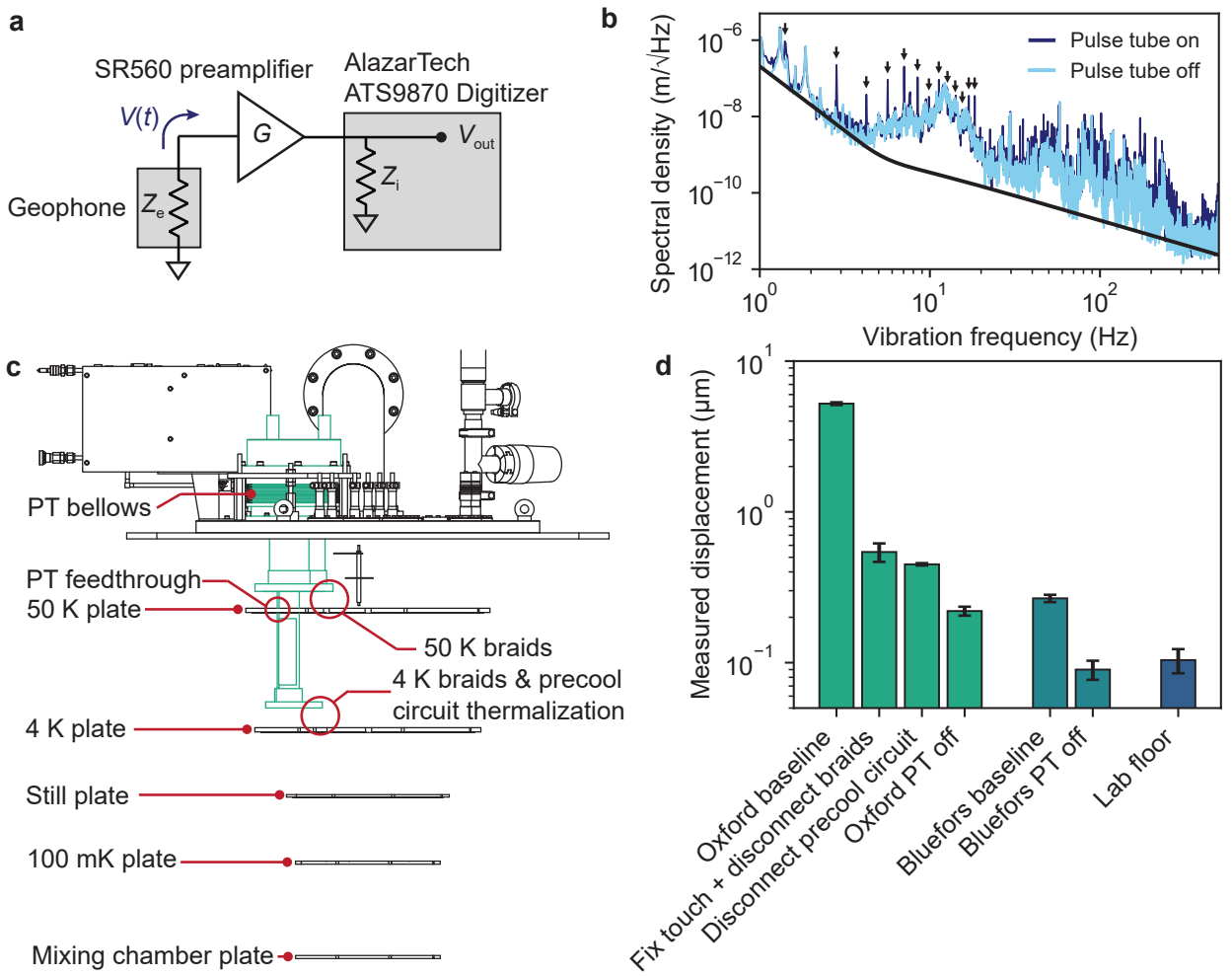

Figure 5.2: (a) Electrical circuit used to measure vibrations. The geophone produces a time-dependent voltage $V(t)$ due to external vibrations, which is subsequently amplified with gain $G = 500$ and recorded. (b) Two vibration spectra recorded with the pulse tube on and off (dark blue and light blue, respectively) at $T = 20$ mK. The arrows show expected locations of the first few pulse tube overtones ($f_k = 1.41k$ Hz), which disappear when the pulse tube is turned off. The solid black line shows the contribution of voltage noise with a $1/f$-like scaling ($V \propto f^{-0.3}$). (c) Oxford Triton 200 schematic with the pulse tube (PT) drawn in green. Vibrations from the pulse tube are transmitted to the mixing chamber plate via the PT bellows, thermalization braids at both 50 K and 4 K, physical contact (i.e. a touch) at the PT feedthrough, and through the precool circuit thermalization. (c) Measurements of the vertical RMS displacement at the mixing chamber plate with the PT turned on at room temperature. The Oxford baseline is measured with braids and precool circuit thermalization installed and with an unintended touch at the PT feedthrough. The biggest reduction in vibrations was achieved after fixing the touch and disconnecting the braids. For reference we also show the displacement with the PT turned off. A measurement at the mixing chamber of a different refrigerator in the laboratory, labeled Bluefors, shows much lower vibrations. This indicates that our measured vibration levels depend sensitively on the fridge construction and environment. The displacement measured with the PT turned off is comparable to the displacement measured with the geophone placed on the laboratory floor.

the PT may touch the 50 K plate at the PT feedthrough (Fig. 5.2c). Secondly, the factory-installed copper thermalization braids between the PT and plates are not flexible enough to block PT vibrations from entering the plate. Replacing these braids with longer and more flexible home-made braids in combination with fixing the physical touch at the PT feedthrough reduces the RMS vibrations by an order of magnitude (Fig. 5.2d). The precool circuit constitutes the final rigid connection, but it cannot be disconnected during cooling and, moreover, disconnecting the precool circuit only slightly reduces the RMS vibrations. With the refrigerator in working condition, the remaining RMS vibrations are $d_{\mathrm{rms}} = 0.5$ µm.

The remaining RMS vibrations are a factor two larger compared with the PT turned off, and are considerably larger than the those of a comparable dilution refrigerator in the same laboratory space (Fig. 5.2d), suggesting it should be possible to further reduce the RMS vibrations to below $d_{\mathrm{rms}} = 0.5$ µm. This may be accomplished by repositioning the PT motorhead to relieve tension in the braided hose attached to the PT, or disconnecting the PT from the fridge frame by mounting it to the lab ceiling. However, the efficacy of these passive vibration isolation methods remains to be tested and in general it is difficult to isolate a device from low-frequency vibrations using only passive isolation techniques [80].

Active vibration cancellation can be very effective at cancelling low-frequency vibrations [90]. In the next sections, we implement active vibration cancellation of the liquid helium substrate in a micro-channel using electric fields. On-chip vibration cancellation is advantageous over off-chip cancellation, since on-chip electric fields regularly exceed 1 MV/m and thus produce a large dielectrophoretic force on the superfluid. In addition, the amount of liquid helium on the chip is small, and in the case of superconducting electrodes, cancellation does not dissipate heat.

5.2 A microwave resonator as superfluid helium levelmeter

We detect on-chip pulse-tube-induced liquid helium vibrations using a lumped element LC-resonator, which consists of two meandering inductances and interdigitated capacitors (IDCs,

see Fig. 5.3a). A 0.4 µm layer of hard-baked photoresist covers the entire 80 nm thick Al resonator and ground plane, except at a narrow strip which aligns with the IDC. This strip forms a micro-channel (width $w = 17$ µm and depth $d_0 = 0.4$ µm) for liquid helium and confines liquid helium above the IDC where most of the resonator's microwave electric field is concentrated (Fig. 5.3d). When liquid helium is present in the micro-channel, we detect a change in the helium level as a negative resonance frequency shift, because the dielectric constant of helium is slightly larger than ε_0. Therefore, our microwave resonator acts as a sensitive helium level meter with resonance frequency $f_0 = 6.06$ GHz and linewidth $\kappa/2\pi = 160$ kHz[1].

The response of the level meter to liquid helium shows three distinct regions, each associated with a different filling regime (Fig. 5.3e). In region I, a thin layer of liquid helium coats the entire sample cell including the resonator, which leads to a small resonance frequency shift of $\Delta f_0 < 0.1$ MHz. In the second regime, there is enough helium to fill the gaps between the fingers of the IDC and finally in region III, liquid helium fills the micro-channel as shown in Fig. 5.3c. For the following experiments, we fix the helium level as indicated by the red star in Fig 5.3e, where we estimate a helium thickness in the center of the micro-channel $t_{\mathrm{He}} = 250$ nm[2].

Vibrations from the building and PT perturb the liquid helium level inside the off-chip cylindrical reservoir (Fig. 5.3c) and subsequently modulate the helium level in the micro-channel, which we detect as a time-dependent resonance frequency jitter σ_f (Fig. 5.3f). The jitter increases by an order of magnitude during the transition from region I to region II, because the level meter is most sensitive to small changes in helium level between the

1. We find that the loaded quality factor ($Q_L \approx 4 \times 10^4$) is limited by the coupling capacitance, and not (as one may expect) by the presence of the hardbaked photoresist, because the participation of the electric field in the photoresist is minimized by removing the photoresist above the IDC. If the photoresist had also covered the IDC, we expect an internal quality factor $Q_i \approx 1/\tan\delta \approx 10^2$ [91].

2. The maximum resonance frequency shift occurs when the entire upper half plane is filled with helium and is given by $\Delta f_0 = -f_0\left(1 - \sqrt{(\varepsilon_s p_s + \varepsilon_0 p_u)/(\varepsilon_s p_s + \varepsilon_{\mathrm{He}} p_u)}\right) \approx -16.9$ MHz, where p_s and p_u are the energy of the electric field stored in the substrate and upper half plane, respectively. Because the energy density $E^2(x, y, z)$ extends a few microns above the shallow micro-channel, the frequency shift does not saturate when the channel is full.

IDC fingers, and decreases again in region III, because surface tension stabilizes the liquid helium surface. The large correlation between the resonator jitter and the derivative of the data in Fig. 5.3d ($\partial f_0/\partial h$) confirms that the observed jitter is caused by helium reservoir vibrations of magnitude $\Delta h \approx 50$ µm. This large value is consistent with the PT vibrations ($d_{\mathrm{rms}} = 0.5$ µm) and an underdamped helium reservoir resonance of $Q \approx 10^2$.

5.3 Liquid helium response to DC bias voltages

To gain control over the helium level in the micro-channel without adding helium to the sample cell, we apply a bias voltage to the resonator center pin. The symmetric design of the level meter allows for applying such a bias voltage while maintaining a narrow resonator linewidth. For small voltages we observe a resonance frequency shift proportional to V_{res}^2 (Fig. 5.4), consistent with an electrostatic model which assumes the frequency shifts linearly with a small change in t_{He}

$$\Delta f_0 = g_{\mathrm{He}} \Delta t_{\mathrm{He}} = \frac{w^2}{16\sigma} g_{\mathrm{He}} \left(\varepsilon_{\mathrm{He}} - 1\right) \varepsilon_0 V_{\mathrm{res}}^2 E_V^2(x, y) = \alpha V_{\mathrm{res}}^2, \tag{5.2}$$

where E_V^2 is the electric energy density above the IDC with an applied bias voltage of $V_{\mathrm{res}} = 1$ V, and g_{He} is the helium coupling strength. For larger voltages, the resonance frequency increases faster than quadratic and the helium vibrations become more prominent, which we attribute to the formation of a helium bubble above the IDC. The simple model of Eq. (5.2) is therefore no longer appropriate.

The helium coupling strength is a key parameter of our level meter, since it determines the smallest observable change in helium thickness. We determine $g_{\mathrm{He}} = 0.79 \pm 0.03$ kHz/nm from a fit to the quadratic coefficient α and the average value of the simulated E_V^2 at $z = 0.4$ µm above the capacitor (Fig. 5.3d). It is slightly smaller than for comparable coplanar waveguide resonators [57] because the channel is wider and helium occupies a smaller portion of the resonator's mode volume in our design. Since the mode volume is

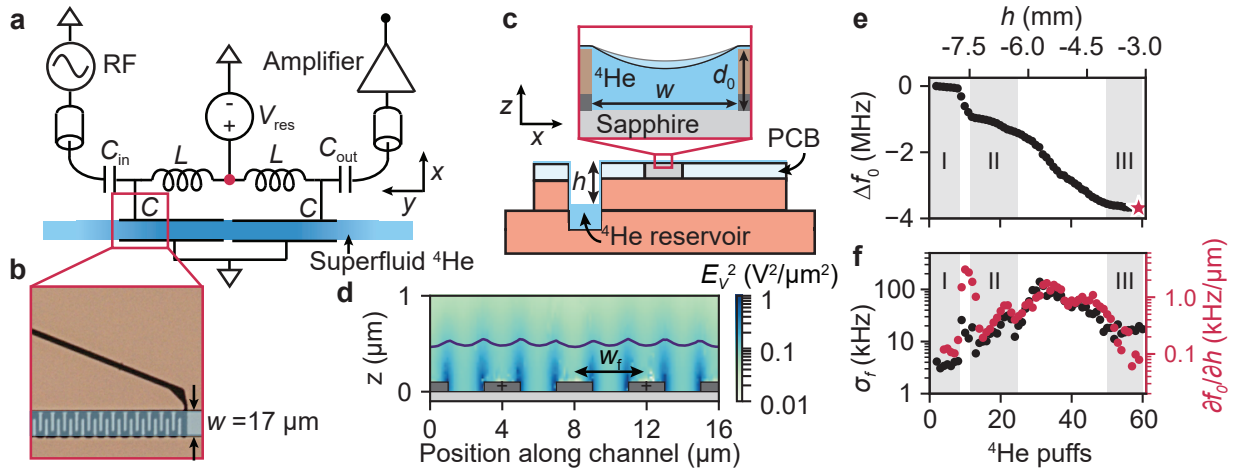

Figure 5.3: (a) Schematic of the circuit used to characterize and mitigate on-chip helium vibrations. The helium sensor consists of a symmetric lumped element LC-resonator, which can be probed and read out by sending RF tones via the coupling capacitors C_{in} and C_{out}. Due to the symmetric resonator design, the microwave mode has a voltage node at the red dot, which we exploit to apply a bias voltage V_{res} to the resonator center pin without destroying the resonator quality factor. (b) Zoomed in micrograph of one of the capacitors of the LC-resonator. The interdigitated capacitor fingers are aligned with a micro-channel (width $w = 17$ μm) such that liquid helium interacts with the electric fringing field from the interdigitated capacitor. (c) Cross-section of the shallow ($d_0 = 0.5$ μm) micro-channel shown in (b), with the photoresist (SU8) micro-channels shown in brown. Off-chip helium reservoir vibrations (Δh) change the helium surface curvature. (d) Simulated microwave electric field along the micro-channel as function of the height above the IDC. When helium fills the volume above the IDC the level meter responds with a negative frequency shift until the mode volume, which extends up to approx. $w_f/2\pi$, is filled. (e) The resonance frequency shifts down after adding liquid helium to the sample cell and we recognize three different filling regions. (f) The vibrating helium surface modulates the microwave resonance frequency over a frequency range σ_f. Each black dot represents the resonance frequency jitter measured by taking the standard deviation of $N = 25$ quick measurements of the resonance frequency. The red dots are determined from the derivative of the data shown in (d), and the correlation between both datasets suggests that the resonance frequency jitter is caused by helium vibrations in the off-chip reservoir.

related to the IDC finger spacing w_f, we can increase g_{He} in a future design by decreasing the IDC finger spacing. In addition, we can increase the coupling strength orders of magnitude by creating a superfluid helium resonator, an approach that has been successful in the optical domain and has allowed cooling of surface excitations [86].

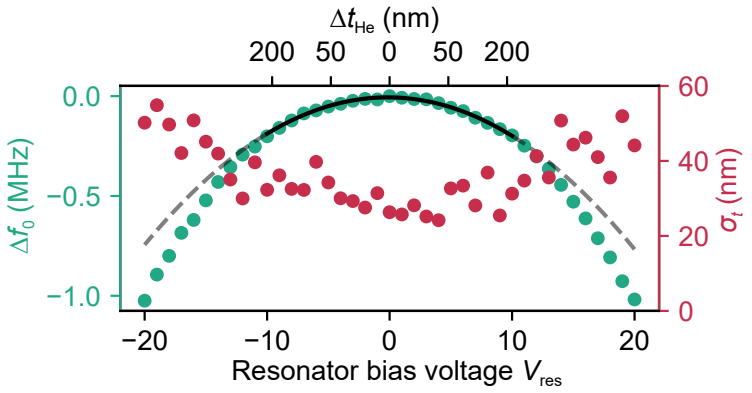

Figure 5.4: (a) Frequency shift (green) and helium fluctuations (red) of the level meter as function of the bias voltage applied to the resonator center pin, measured at the helium level indicated by the red star in Fig. 5.3d. For small bias voltages, the resonance frequency closely follows a quadratic model $\Delta f_0 = \alpha V^2$ (solid black line), where $\alpha = -1.87 \pm 0.07$ kHz/V^2, whereas for larger voltages the resonance shifts faster than the quadratic response. The measured helium fluctuations in the micro-channel σ_t are approximately constant for small voltages but increase for larger voltages.

5.4 Active stabilization of the superfluid interface

From the coupling strength we estimate that a small bias voltage of ± 5 V increases the helium thickness in the micro-channel by 74 nm, which exceeds the helium fluctuations estimated from the measured resonance frequency jitter $\sigma_t = \sigma_f / g_{\mathrm{He}} \approx 26$ nm. Therefore, it should be possible to cancel the resonance frequency jitter σ_f by applying a time-dependent voltage and using the level meter's resonance frequency as the control signal. For a continuous measurement of the resonance frequency, we construct a microwave interferometer shown in Fig. 5.5a. We feed the interferometer output Q, which varies due the helium vibrations d, into a control law K. For sufficiently large K, the control law attenuates helium vibrations

and ensures that the interferometer output follows the setpoint s [92], since

$$Q = (Ks + d)\,\frac{G}{1 + KG} \approx s \tag{5.3}$$

if $KG \gg 1$.

Successful stabilization of the helium surface depends on the detection sensitivity of disturbances $d(f)$ as well as our ability to correct for them. Assuming Johnson noise limits the signal to noise of the detection chain, the smallest observable change in helium thickness depends sensitively on the helium coupling strength g_{He}, on the noise figure of the first amplifier in the chain (F_1), and can be increased with a stronger microwave drive (which increases the average intra-cavity photon number, n_{ph}):

$$\frac{\Delta t_{\mathrm{He}}^2}{\Delta f} = \frac{\pi}{2}\frac{k_B T F_1 \kappa}{g_{\mathrm{He}}^2 n_{\mathrm{ph}} h f_0}. \tag{5.4}$$

For a typical drive power just below the resonator's bifurcation point ($n_{\mathrm{ph}} \approx 10^5$) we achieve a detection sensitivity of 0.5 pm/$\sqrt{\mathrm{Hz}}$, two orders of magnitude better than quartz tuning fork helium surface probes [93, 94]. We can correct for the helium vibrations as long as the vibration spectrum contains no frequency components above the resonator linewidth $\kappa/2\pi = 160$ kHz, since the time for photons to leak out of the cavity is $1/\kappa$. For helium vibrations within the resonator bandwidth, the proportional gain must be large enough to dampen vibrations and to avoid instabilities that arise due to higher-order resonances or time delays (i.e. if $KG = -1$) [92]. We avoid time delays from sampling, often seen in digital control loops, by implementing our control law $K(f)$ using op-amps with a large bandwidth and fast slew rate (see Appendix F).

The transfer function $G(f)$ captures to what extent we can compensate for helium vibrations at different frequencies and encompasses the level meter with helium above the IDC, amplifiers, filters and the IQ mixer on the output line. We experimentally determine G by applying an oscillating voltage $u(f) = u_{\mathrm{dc}} + u_{\mathrm{ac}} \cos(2\pi f t)$, where $u_{\mathrm{dc}} = 4.0$ V and

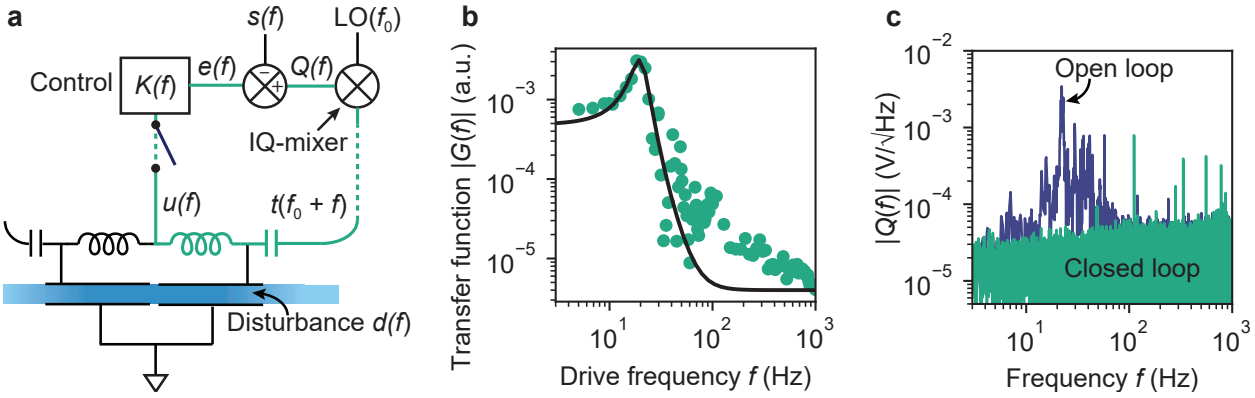

Figure 5.5: (a) When operating the microwave resonator in a closed loop configuration (green, switch closed), a control law $K(f)$ cancels liquid helium vibrations $d(f)$ by applying a voltage $u(f)$ to the resonator center pin. Helium vibrations are detected as sidebands on a resonant transmitted microwave tone $t(f_0+f)$, which is demodulated at the IQ-mixer using a local oscillator (LO(f_0)). The demodulated resonator transmission $Q(f)$ and a setpoint $s(f)$ serve as inputs for the control law. A constant setpoint tunes the liquid helium level inside the micro-channel. (b) By applying a voltage $u(f) = u_{\mathrm{dc}} + u_{\mathrm{ac}} \cos(2\pi f t)$ and recording the resonator transmission $Q(f)$ we determine the system transfer function $|G(f)|$ (green dots). The transfer function follows the response of a second-order model (black line) with $f_0 = 20.3$ Hz, $Q = 2.5$ and a high frequency response described by a constant noise floor of $|G(f)| = 4 \times 10^{-6}$. (c) Comparison of closed and open loop operation of the feedback loop shown in (a). The closed loop operation (green) shows a strong suppression of liquid helium vibrations.

$u_{\mathrm{ac}} = 1.0$ V, while recording the demodulated microwave transmission $Q(f)$. The resonance in the transfer function at $f_0 = 20.3$ Hz is likely associated with liquid helium in the micro-channel, since we have observed different G for different micro-channel geometries. The increased G around the resonance implies that vibrations around f_0 are easily cancelled with only a small voltage. However, the decrease in G at higher frequencies indicates that a high-frequency drive hardly affects the helium surface, which negatively impacts cancelation of any potential high frequency vibrations. Fortunately, there are hardly any vibrations with frequency above 1 kHz (Fig. 5.2b), so the decrease in $G(f)$ should not be an issue.

We now test the performance of the control loop by comparing the resonator output $Q(f)$ with the feedback turned on (closed loop) and off (open loop). The envelope of the open loop spectrum (Fig. 5.5c, blue) follows the shape of the transfer function with a maximum around the transfer function resonance. The additional structure between 10^1 and 10^2 Hz is due to the PT and building vibrations, since they are also visible in the geophone spectra of Fig. 5.2b. When the control loop is closed, all features disappear and the RMS vibrations decrease from $\sigma_t = 26$ nm to $\sigma_t = 5$ nm, indicating that the control law successfully cancels helium vibrations and stabilizes the surface to a quiet state. The remaining output signal is dominated by measurement noise, and more averaging can provide insight into what ultimately limits the closed loop vibration level.

A quiet helium surface would reduce noise in measurements with electrons on helium and drastically reduce dephasing of a single electron trapped on helium. It is straightforward to implement the control loop of Fig. 5.5a with a charged helium surface, although canceling single electron vibrations requires a local measurement of the helium vibrations and therefore requires a different resonator design than presented in chapter 4 or Ref. [57]. Alternatively, since on-chip helium vibrations originate from the cylindrical reservoir, it may be possible to cancel on-chip using a level meter inside the helium reservoir [88].

In conclusion, we have used a microwave resonator to stabilize the vibrating surface of superfluid helium and achieved a fivefold reduction in vibrations. Application of these results

to electrons on helium may help to reach the strong coupling regime of a single electron on helium.

CHAPTER 6

OUTLOOK

6.1 Strong electron-photon coupling

The measurements of chapter 4 suggest that by increasing the coupling strength and decreasing the electron linewidth, strong electron-photon coupling should be possible. Here we present two promising strategies to achieve this, starting with the use of high-kinetic inductance (KI) materials.

6.1.1 High-Kinetic Inductance materials

High-KI materials are a promising and convenient way to increase the electron-photon strength. KI originates from the inertia of Cooper pairs, the charge carriers in a superconductor, and is particularly large for superconductors such as TiN, NbN and NbTiN, because they have a large magnetic penetration length λ_L.

A large KI results in a large coupling strength, because a large (kinetic) inductance increases the zero-point fluctuations $V_{\mathrm{rms}} = \omega_0\sqrt{\hbar Z/2}$ and according to Eq. (1.37), g is proportional to the zero-point fluctuations across the capacitor. By increasing the resonator's inductance relative to the capacitance, for example through the use of high KI materials, we can increase the electron-photon coupling strength. The use of high-impedance microwave resonators has already led to strong electron-photon and spin-photon coupling in semiconducting quantum dots [41, 43, 49].

Using materials with a large KI L_k is an attractive method to enhance the coupling strength, because the kinetic inductance can be lithographically adjusted via the wire width w and film thickness t:

$$L_k = \frac{\mu_0 \ell \lambda_L^2}{wt} = \frac{L_\square \ell}{w}, \tag{6.1}$$

where ℓ is the inductor length and $L_\square$ is the sheet inductance. For example, resonators

with thin, narrow titanium nitride inductors can easily reach sheet inductances of 0.1 nH/$\square$ which result in characteristic impedances of $Z \approx 10$ kΩ, while maintaining a high quality factor ($Q_i > 10^5$)[48]. Therefore, by fabricating our coplanar stripline resonators of titanium nitride, and reducing the film thickness to $t \approx 15$ nm, we expect a coupling strength enhancement of

$$\frac{g'}{g} = \sqrt{\frac{Z'}{Z}} = \left(1 + \frac{L_\square}{\mu_0 w}\right)^{\frac{1}{4}} \approx 3, \tag{6.2}$$

where we have assumed the geometric inductance can be approximated as $\mu_0 \ell$, and a reasonable sheet inductance is $L_\square = 50$ pH/$\square$, which would correspond to a 15 nm TiN film [48]. Note that the coupling strength can be further enhanced by reducing the center pin width.

6.1.2 Vibration insensitive dot

The single electron linewidth γ_φ is limited by classical helium fluctuations inside the dot, and depends on the vibration amplitude Δt_{He} as well as the electron's sensitivity $\partial f_e / \partial t_{\mathrm{He}}$. Since attempts at reducing Δt_{He} have been unsuccessful thusfar, or are not straightforward to incorporate with our experimental system, we believe designing a vibration insensitive dot is the most promising way to reduce γ_φ. The sensitivity of the two-electrode design (discussed in Fig. 2.6) is particularly large, because the curvature of the electrostatic potential changes sign as t_{He} increases. Therefore, even though the two-electrode design offers a large trap depth, it is very susceptible to an increased linewidth due to classical helium fluctuations.

Electrostatic simulations of a single-electrode design suggest we can decrease the sensitivity $\partial f_e / \partial t_{\mathrm{He}}$ by changing the electrode and channel dimensions. Fig. 6.1a depicts a preliminary design which shows a negligible sensitivity to helium vibrations over a $\Delta t_{\mathrm{He}} \approx 100$ nm-wide region (Fig. 6.1d). This single-electrode design also offers a 25-mV-deep trap near the resonance condition (Fig. 6.1b), which according to Fig. 2.7 should be sufficient to keep electrons contained in the dot.

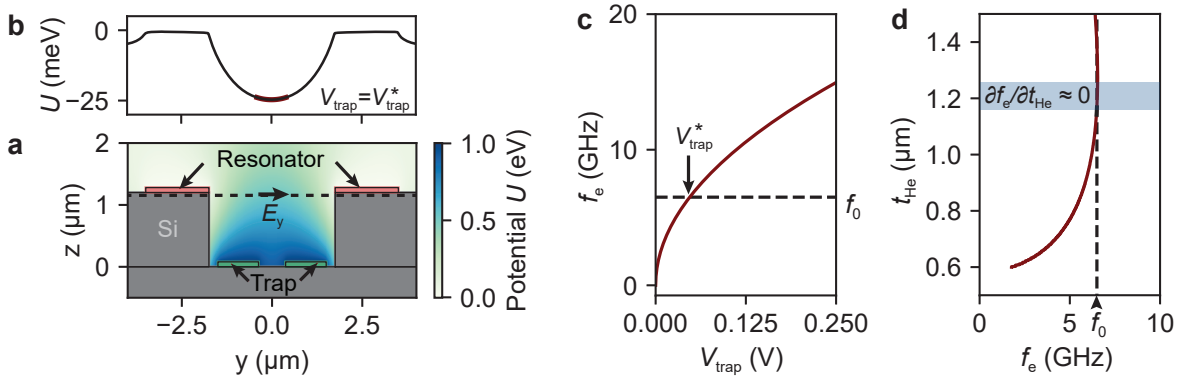

Figure 6.1: An improved dot design with a helium vibration-insensitive region. (a) A single electrode on the bottom of the micro-channel creates an electrostatic potential (color) which is less sensitive to classical helium fluctuations. Removing metal from the center of the trap electrode slightly increases the anharmonicity of this design. The differential mode of the resonator, which is located above the micro-channel (red), produces a transverse microwave electric field E_y which couples to the electron. (b) Electrostatic potential evaluated at the dashed line in (a) for the crossing voltage V^*_{trap} (i.e. where $f_e = f_0$). The trap depth is 25 meV. (c) The electron frequency tunes over 15 GHz in 0.25 V and the dot has a sensitivity of $\partial f_e/\partial V_{\mathrm{trap}} = 70$ GHz/V at the crossing with the resonator. (d) For a constant voltage $V_{\mathrm{trap}} = V^*_{\mathrm{trap}}$, the electron frequency approaches f_0 as helium fills the channel. Above a certain helium level t_{He} the sensitivity to small changes in t_{He} is negligible, but the maximum filling level is set by the depth of the channel. This lower and upper bound mark the blue shaded region, which depicts the desired operating regime where the linewidth should be insensitive to helium vibrations.

Since the electrons on the reservoir form the second largest contribution to the single electron linewidth ($\gamma_\varphi^{\mathrm{res}}/2\pi \approx 20$ MHz), we also aim to reduce the coupling to the electron reservoir by fabricating an additional "reservoir" electrode at the bottom of the micro-channel, which displaces the electron reservoir from the trap electrode towards the reservoir electrode. The improvements to the dot's sensitivity as well as removing the electron reservoir should reduce the linewidth to order of 1 MHz.

6.2 Coupling to the electron spin state

Achieving strong coupling to a single electron's orbital state also allows for an indirect coupling to the electron spin state. This is significant, because achieving a large *direct* spin-photon coupling is very difficult due to the electron's small magnetic moment. To illustrate this, let us first derive the direct spin-photon coupling strength.

The coupling of a microwave photon to an electron spin is given by the interaction Hamiltonian

$$H_{\mathrm{spin}} = -\boldsymbol{\mu} \cdot \mathbf{B} = g\mu_B \mathbf{B} \cdot \mathbf{S}, \tag{6.3}$$

where g is the Landé g-factor for an electron spin and $\mathbf{S} = \hbar/2\,\boldsymbol{\sigma}$ is the electron spin operator. The magnitude and direction of the resonator's B-field determine the coupling g_{spin}:

$$\hbar g_{\mathrm{spin}} = \frac{\hbar}{2} g\mu_B B_I I_0, \tag{6.4}$$

where we wrote the microwave B-field as a product of magnetic field per unit current (B_I) and vacuum fluctuations of the current (I_0). On resonance, the zero-point energy $\frac{1}{2}\hbar\omega_0$ is equally divided between the inductor and the capacitor, such that the vacuum fluctuations in the current are $I_0 = \sqrt{\hbar\omega_0/2L} = \omega_0\sqrt{\hbar/2Z}$. Therefore, the coupling spin-photon coupling strength is

$$\frac{g_{\mathrm{spin}}}{2\pi} = g\mu_B B_I \omega_0 \sqrt{\frac{\hbar}{8Z}} \tag{6.5}$$

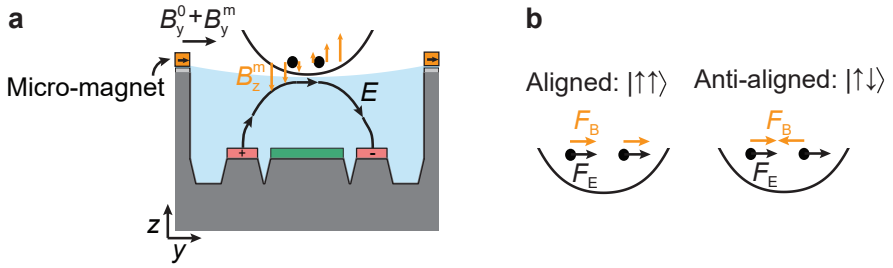

Figure 6.2: A way towards addressing the electron spin state. (a) A micro-magnet deposited on top of the ground plane creates an out-of-plane magnetic field B_z^m that varies linearly at the electron location. The resulting field gradient results in a spin-dependent force for electrons in the dot. (b) Illustration of the magnetic force F_B and electric force F_E as seen by a two-electron Wigner molecule inside the dot. The magnetic force on anti-aligned spins excited differential electron motion, which is off-resonant from the center-of-mass mode due to strong electron interactions. This principle could form the basis of a Wigner molecule spin detection scheme.

Even in optimized resonator geometries with very low resonator impedance and concentrated magnetic fields B_I, the direct spin-photon coupling strength may only reach 100 Hz [95].

Coupling to the electron-spin via the electron orbital state can result in a much larger coupling strength, because in the presence of a spatially inhomogeneous magnetic field[1], the strong electric dipole moment mediates coupling to the spin. An oscillating electron in an inhomogeneous B-field experiences an oscillatory magnetic field, which can flip the electron spin if the orbital frequency is resonant with the Larmor frequency $\omega_L/2\pi$. The resulting spin-photon coupling is given by [28]

$$g_{\text{spin}} = \mu_B y_{\text{zpf}} \frac{\partial B_z}{\partial y} \frac{g_{\text{orb}}\sqrt{2}}{\hbar\omega_e \left(1-\omega_L^2/\omega_e^2\right)}, \tag{6.6}$$

which can reach $g_{\text{spin}}/2\pi \approx 1$ MHz for sufficiently small detuning ($\omega_L \approx \omega_e$).

Implementation of such a system is almost straightforward, for example by depositing a strip of magnetic material on top of the ground plane (Fig. 6.2a). The permanent magnetization of such a strip creates a field gradient $\partial B_z^m/\partial y$, which establishes the spin-photon coupling to the resonator.

1. This inhomogeneous magnetic field can be created with a deposited strip of cobalt (i.e. a micro-magnet) [96] or a current-carrying wire [28].

Our ability to trap Wigner molecules on helium could also allow for detection of their spin state. In the presence of a large biasing field B_y^0 (oriented parallel to the thin superconducting film), electron spins either point both in the same direction ($|\uparrow\uparrow\rangle$ or $|\downarrow\downarrow\rangle$) or in opposite directions ($|\uparrow\downarrow\rangle$ or $|\downarrow\uparrow\rangle$). Now suppose we have adjusted the bias voltages such that the center-of-mass motion is resonant with the resonator ($\omega_e = \omega_0$). Photons in the resonator exert an electrostatic force F_E on these electrons, causing the electrons to oscillate in concert at frequency ω_e. However, the direction of the magnetic force on the spins depends on σ_z and therefore, the magnetic force on the anti-aligned electrons (e.g. $|\uparrow\downarrow\rangle$) will try to excite differential electron motion (Fig. 6.2b). Because the differential electron mode frequency is off-resonant with the resonator due to the strong electron interactions, the electron motion will be unaffected for anti-aligned spins. On the other hand, the magnetic force on aligned spins adds to F_E and therefore results in a much stronger resonator signal. Therefore, the strong electron interactions within Wigner molecules in a magnetic field can be used to distinguish different spin states, and could possibly be used to create entangled spin states of Wigner molecules.

By now, it is hopefully clear that the future of circuit QED with strongly interacting electrons looks bright, and has many future research directions. These projects are left as an exercise for the interested reader of this thesis.

APPENDIX A

FABRICATION OF AN ELECTRON-ON-HELIUM DOT

In this appendix, we outline the fabrication recipe for the electron-on-helium dot described in chapters 2 and 4. Our recipe consists of four steps, which we summarize below.

First an 80 nm thick Nb ground plane is evaporated onto a high-resistivity (> 10 kΩcm) Si $\langle 100 \rangle$ wafer, followed by deposition of a 100 nm thick silicon oxide sacrificial layer, which is used to protect the Nb ground plane during the following etch steps. The micro-channels are defined using a Raith EBPG-5000+ electron beam lithography system and etched using a CHF_3/SF_6 chemistry, immediately followed by an HBr/O_2 etch. In the second step the resonator center pins are defined using e-beam lithography. After development, evaporation of a 150 nm thick Nb layer and lift-off, the center pins remain on the bottom of the micro-channel. To improve robustness of the device and avoid electrical breakdown at low temperatures, we etch an additional $\sim$400 nm of Si substrate in between the resonator center pins. To this end, another layer of 80 nm thick silicon oxide is deposited, after which the additional Si is etched with the previously described etch chemistry. The silicon oxide layer is removed using buffered HF and a DI water rinse.

A.1 Preparation of metal layer and hard mask

1. On a blank Si wafer, deposit 80 nm Nb at a rate of 0.9 nm/s using a Plassys e-beam evaporator.

2. Deposit 80 nm of SiO_2 using a PlasmaTherm Apex SLR HDPCVD. For consistency we run the machine with the Si wafer mounted on a SiO_2 carrier wafer, both for the preconditioning as well as the actual deposition.

3. Spin 800 nm ARP 6200.13.

   (a) 500 rpm @ 250 rpm/s for 5 s

(b) 2000 rpm @ 1000 rpm/s for 60 s (gives 800 nm thickness)

4. Make sure the back of the wafer is relatively clean, then bake wafer at 150 °C for 60 s.

A.2 Defining the channels

1. We use a Raith electron beam lithography tool to write the patterns that define our channels.

2. Develop in N-amyl acetate. Use a cold development plate with internal PID loop set to 2.0 °C and develop for 60 s, no agitation.

3. Quickly transfer the wafer into a dish of IPA and agitate slightly for 10 s. Let sit for another 2 minutes agitating now and then. Blow dry.

4. Using a CHF_3 and SF_6 chemistry etch through the Nb and SiO_2. We used a PlasmaTherm ICP Fluorine Etcher to do this step.

5. After transferring the wafer to a PlasmaTherm ICP Chlorine Etcher, use a Cl_2 punch through step to clear the native oxide from the now exposed Si substrate. Next use a HBr and O_2 based chemistry to etch into the Si.

6. After the HBr etch, the resist has been consumed fully and the SiO_2 has done its job as a hardmask to prevent the Nb from being etched. To remove the SiO_2, but not the Nb, we dip the wafer in a dish of buffered HF for 2:30 min. After this, we rinse the wafer in a dish with DI water, making sure to agitate.

A.3 Defining the resonator center pin

1. Spin ARP 6200.13 at 4000 rpm and bake at 150 °C for 60 s.

2. Align the layer that contains the microwave resonator center pin to the previously written layer. Even though resist profile in the trenches is non-uniform we found a similar dose as in the first layer gives good results.

3. Develop for 60 s with internal PID of the cold plate set to 2.0 °C.

4. Evaporate 150 nm of Nb on the developed wafer at 0.9 nm/s.

5. Use a teflon wafer holder to place the wafer upside down in a pre-heated bath (80 °C) of NMP for 8 min and gently agitate.

6. Sonicate at 70 kHz at half power for 8 min.

7. Take out of the hot NMP, spray with cold NMP and transfer to IPA dish. Blow dry.

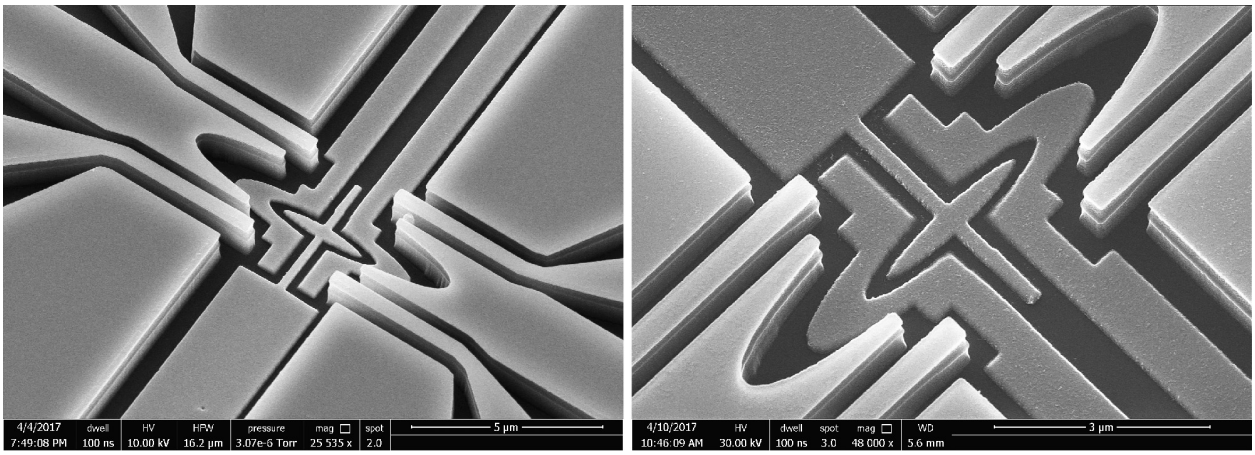

Figure A.1: Scanning electron microscope images after lift-off of the trap and resonator electrodes.

The next steps are intended to prevent electrical break down between the resonator and trap electrodes. The minimum distance between these electrodes is 200 nm, and typical electric fields used in experiment can range up to 10 MV/m. To prevent electrical break down we etch into the Si substrate in between the resonator and trap electrodes

A.4 Etch in between the resonator and trap electrode

1. Deposit 80 nm of SiO_2 with the wafer mounted on a 4" SiO_2 carrier wafer using the same process as in step a2.

2. Spin ARP 6200.13 at 2000 rpm and bake for 60 s at 150 °C.

3. Write the pattern and develop at 2.0 °C for for 60 s. When drying the wafer make sure to be extremely gentle.

4. Use the previously used SF_6 and CHF_3 based chemistry to etch through the SiO_2.

5. Use the previously used HBr and O_2 based chemistry to etch in between the center pins. The length of the Cl_2 punch through step is extremely important, since the tall resist structure is sensitive to deformation due to overheating.

6. Strip the resist by leaving the wafer in 80 °C NMP and sonicating for 10 min. Then dip in HF for 2:30 min and dump rinse with DI water. Repeat the NMP and HF strip step once more in order to make sure all the resist is removed from all electrodes.

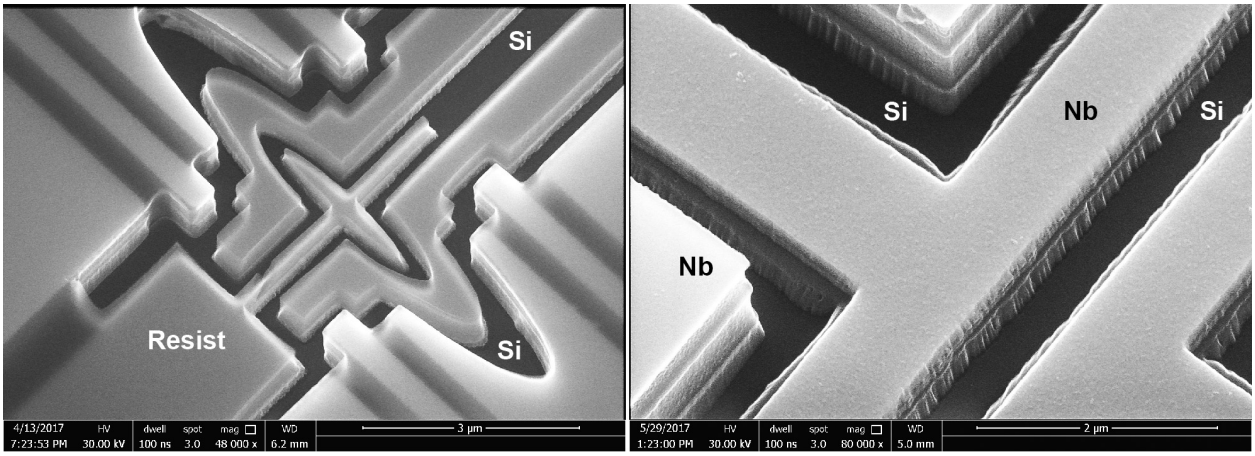

Figure A.2: Scanning electron microscope images of the etch in between the resonator and trap electrode. Left: image after step 3. The resist forms a mask that protects the electrodes from being etched in the following steps. Right: image after step 6. The etch has removed approximately 450 nm of Si in between the resonator center pins.

APPENDIX B

MODEL FOR UNLOADING THE DOT

In the experiments presented in chapter 4, we unload the dot by sweeping the trap guard to $V_{\mathrm{tg}} = V_{\mathrm{unload}} < 0$ while keeping all other electrodes constant at $(V_{\mathrm{res}}, V_{\mathrm{trap}}, V_{\mathrm{rg}}) = (0.6, 0.15, -0.4)$ V. We then ramp the electrodes back to $(V_{\mathrm{trap}}, V_{\mathrm{tg}}) = (0.175, 0)$ V in order to probe the resonator transmission. A single unloading procedure takes about 10 ms, which is limited by the corner frequency of the trap guard electrode RC-filter. The ramp speed does not affect the charging diagram of Fig. 4.5b.

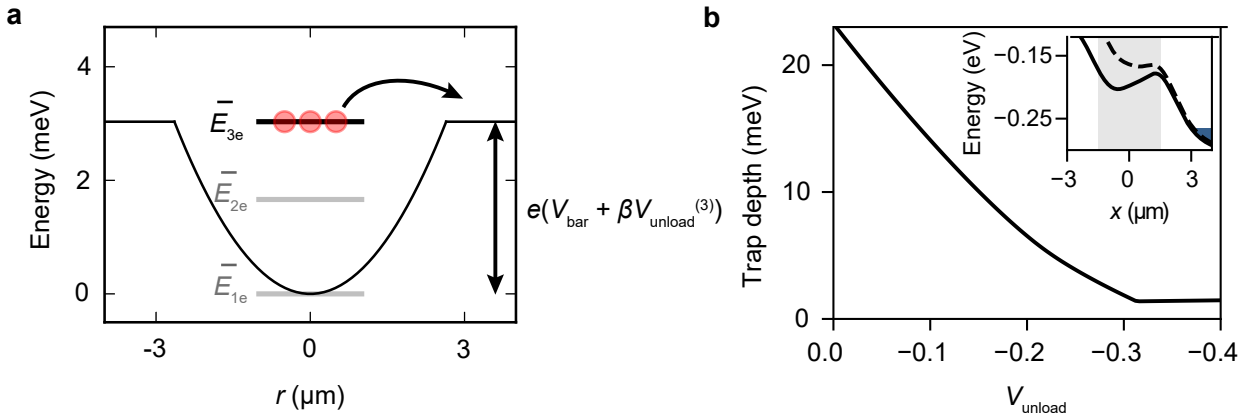

Figure B.1: Electrostatic model for unloading of the dot. (a) One electron leaves the dot if the average energy per electron $\bar{E}_{ne}$ exceeds the trap depth. (b) The simulated trap depth depends linearly on the unloading voltage V_{unload}, and approaches zero for $V_{\mathrm{unload}} = -0.305$ V, which coincides with the measured voltage of the last jump in Fig. 4.5b. The inset shows the electrostatic potential along the channel for two values of the unloading voltage: $V_{\mathrm{unload}} = 0$ (solid line) and $V_{\mathrm{unload}} = -0.40$ V (dashed line).

To confirm that changes between transmission plateaus in Fig. 4.5b are associated with single electron transport, we simulate electron unloading using a combination of electrostatic simulations and analytical calculations. Even though the electrode geometry in the dot produces a complex and anharmonic trapping potential on the scale of the dot (8×4 μm), the small extent of the electron ensemble (0.5×0.5 μm) justifies a model based on an axially symmetric harmonic well with potential energy $E = \frac{1}{2} m_e \omega_e^2 r^2$ (Fig. B.1a). In a harmonic well, we can calculate the Wigner molecule energies analytically, which simplifies

the calculation of the unloading voltages.

We predict unloading events when the average energy per electron exceeds the trap depth V_b, which is expected to decrease linearly with more negative unloading voltages: $V_b = V_{\mathrm{bar}} + \beta V_{\mathrm{unload}}$. From finite element simulations of the electrostatic potential, we confirm this linear dependence (Fig. B.1b) and we determine $V_{\mathrm{bar}} = 22$ meV. Furthermore, we determine β from the final jump in resonator transmission in Fig. 4.5b. Finally, using the analytical expressions for the Wigner molecule energies [97], we find the unloading voltages $V_{\mathrm{unload}}^{(N)}$ when $N = 1 - 4$ electrons escape the dot:

$$
\begin{aligned}
V_{\mathrm{unload}}^{(1)} &= -\frac{V_{\mathrm{bar}}}{\beta} = -0.305\,\mathrm{V} \\
V_{\mathrm{unload}}^{(2)} &= V_{\mathrm{unload}}^{(1)} + \frac{3}{4}\frac{E_0}{\beta e} \\
V_{\mathrm{unload}}^{(3)} &= V_{\mathrm{unload}}^{(1)} + 1.31037\frac{E_0}{\beta e} \\
V_{\mathrm{unload}}^{(4)} &= V_{\mathrm{unload}}^{(1)} + 1.83545\frac{E_0}{\beta e}
\end{aligned}
$$

where

$$
E_0 = \left(\frac{m_e \omega_e^2 e^4}{2\,(4\pi)^2\,\varepsilon_0^2 \varepsilon_{\mathrm{He}}^2} \right)^{\frac{1}{3}} \tag{B.1}
$$

depends only on the trap curvature at the unloading point (ω_e), electron mass (m_e) and other physical constants. We find best agreement between model and experiment with an effective trap curvature $\omega_e/2\pi = 26$ GHz, which produces the red arrows in Fig. 4.5b.

If the dot had initially contained five electrons, our model would have predicted an additional plateau starting at $V_{\mathrm{unload}}^{(5)}$ = -0.127 V. Since we did not observe this plateau we concluded the trap was initially loaded with $N = 4$ electrons.

APPENDIX C

MODELING OF WIGNER MOLECULE SPECTRA

We have modeled the Wigner molecule spectra of Fig. 4.6 in a two-step process, similar to the process for modeling the equations of motion for an ensemble of electrons on helium, which was briefly discussed in section 2.2.2. First, we solve for the equilibrium positions of electrons in the electrostatic potential, which are then used to solve the coupled equations of motion of the resonator and electrons. The shape of the electrostatic potential strongly affects the electron positions and resonator transmission spectra, and therefore, finding the electrostatic potential that matches the dot's potential is crucial for reproducing the resonator transmission spectra.

We first attempted to simulate the electrostatic potential using a finite element solver (Ansys Maxwell). In Maxwell we obtain a separate potential for each electrode by applying 1 V to an electrode while keeping all other electrodes grounded. We reconstruct the experimental potential in Python by summing the separate potentials with the appropriate electrode weights (i.e. the electrode voltages) and evaluating the potential on the two-dimensional plane $z = 1.15$ µm. With this method, we were unable to reproduce the Wigner molecule spectra of Fig. 4.6 for $N = 3$ and $N = 4$, because the numerical noise in the potential (approx. 0.1 mV) was too large to obtain clean higher order derivatives of the potential ($\partial^2 V/\partial x^2$ and $\partial^2 V/\partial y^2$). We tried to filter numerical noise by applying digital low-pass filters, but were unable to both retain the shape of the potential and obtain a reasonable signal-to-noise for the higher order derivatives.

To avoid numerical noise, we assume that for small x, y around the potential minimum, the potential is given by an anharmonic potential with unknown voltage-dependent coefficients:

$$V(x_i, y_i) = \alpha_0(V_{\text{trap}})x^2 + \alpha_1(V_{\text{trap}})y^2 + \alpha_2(V_{\text{trap}})y^4. \tag{C.1}$$

This is a reasonable assumption, because V contains only even powers of x and y, and thus

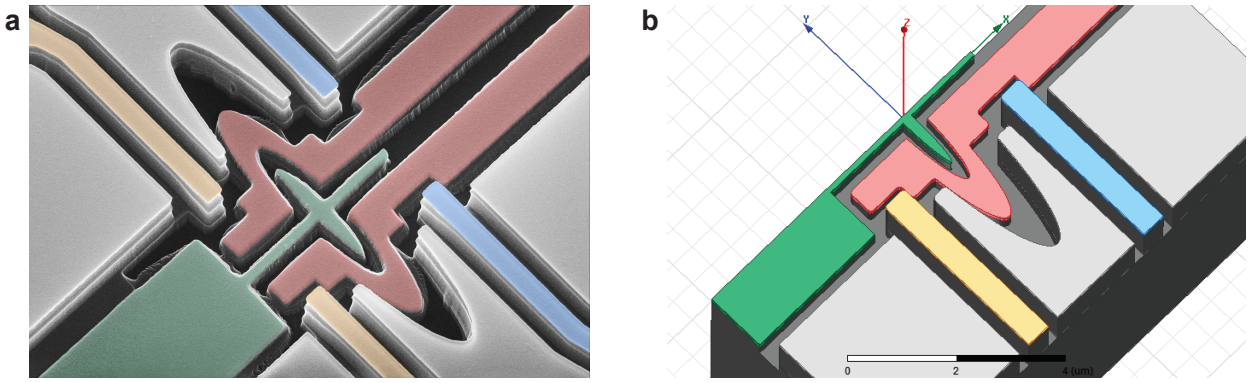

Figure C.1: To determine the electron positions inside the dot we simulate the electrostatic potential using the finite element method. Since the dot is symmetric along the micro-channel axis (left), we can speed-up the simulation (right) by a factor of two by implementing a symmetric boundary condition. The numerical noise in the simulated potential is set by the mesh density and the specified solution accuracy, and it is ultimately limited by the computer's RAM. Even though the model resembles the fabricated device and several attempts have been made to reduce the numerical noise while reducing the computation time, the simulated potential of this model did not reproduce the measured Wigner molecule spectra.

reflects the symmetric design of the dot. Furthermore, the quartic term is justified because without it, the method described below predicts crossings for all Wigner molecules at equal $V^{\star}_{\mathrm{trap}}$, which is inconsistent with experiment. Therefore, the quartic term in Eq. (C.1) is necessary to reproduce the spectroscopy traces. The coefficients α_i were determined by first fitting Eq. (C.1) to the electrostatic potential obtained via finite element modeling, and were then slightly adjusted to reproduce the spectroscopy traces from experiment, using the following method.

For a particular trap voltage we find the Wigner molecule configurations by numerical minimization of the total energy

$$H = \sum_i eV(x_i, y_i) + \sum_{i<j} \frac{e^2}{4\pi\varepsilon_0 |\mathbf{r}_i - \mathbf{r}_j|} \exp(-|\mathbf{r}_i - \mathbf{r}_j|/\lambda), \tag{C.2}$$

which includes a small screening correction to the interaction energy ($\lambda = 1.0$ µm) due to the superconducting electrodes below the electrons. In addition, we neglect the kinetic term in Eq. (C.2), since at $T = 25$ mK the kinetic energy is approximately three orders of magnitude

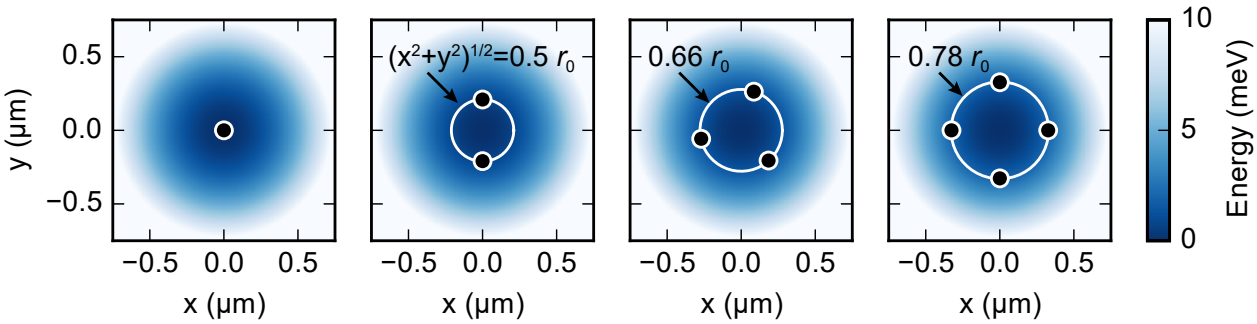

Figure C.2: Verification of the minimization routine by comparing the minimizer's electron configurations in a harmonic well with the theoretical prediction. The electron configurations lie on the circles predicted by the theory.

smaller than the interaction energy. The numerical minimization is implemented in Python and uses the built-in minimization routines of scipy. To speed up this minimization, we explicitly provide the analytical gradient functions calculated from Eqs. (C.2) and (C.1). To ensure that the minimization routine reaches the ground state, we repeat the minimization multiple times with different initial conditions and keep the Wigner molecule configuration with the lowest total energy. This artificial annealing method becomes important for larger Wigner molecules, which tend to have nearly degenerate ground states [97].

To verify our minimization routine, we first run the minimizer with a harmonic electrostatic potential ($\alpha_0 = \alpha_1$, $\alpha_2 = 0$), neglect screening ($\lambda \to \infty$) and compare the electron configurations with theoretical predictions [69, 97]. For 2, 3 and 4 electrons, the electron positions should fall on a circle with radius $0.5\,r_0$, $0.66\,r_0$ and $0.78\,r_0$, respectively, where $r_0 = (e^2/\alpha_0\varepsilon)^{1/3}$. The excellent agreement between the minimizer and harmonic theory (Fig. C.2) boosts our confidence in the minimizer's electron configurations for the anharmonic potential.

With the electron positions for the anharmonic potential at hand, we calculate the orbital frequencies (Fig. 4.6b) and electron eigenmodes (Fig. 4.6c) by numerically diagonalizing the linearized equations of motion of the coupled cavity-electron system (Eq. (2.11)). We include the effects of screening in the kinetic and mass matrix by adjusting the values of $k_{ij}^{\pm}$ and l_{ij}

from Ref. [57] to

$$k_{ij}^{\pm} = \frac{\mathrm{e}^{-\xi}}{4} \frac{e^2}{4\pi\varepsilon_0} \frac{(1+\xi+\xi^2) \pm (3+3\xi+\xi^2)\cos(2\theta_{ij})}{r_{ij}^3} \tag{C.3}$$

$$l_{ij} = \frac{\mathrm{e}^{-\xi}}{4} \frac{e^2}{4\pi\varepsilon_0} \frac{(1+3\xi+\xi^2)\sin(2\theta_{ij})}{r_{ij}^3}, \tag{C.4}$$

where $\xi = r_{ij}/\lambda = |\mathbf{r}_i - \mathbf{r}_j|/\lambda$ and θ_{ij} is the angle between electrons i and j. Note that in the absence of screening, $\xi \to 0$ and we retrieve the familiar values of $k_{ij}^{\pm}$ and l_{ij} from Ref. [57].

To retrieve the resonator transmission spectra of Fig. 4.6a, we use the expression from input-ouput theory (section 1.3.3):

$$\frac{A}{A_0} = \left| \frac{\sqrt{\kappa_1 \kappa_2}}{i(\kappa_1 + \kappa_2 + \kappa_{\mathrm{int}})/2 - \chi(\omega_0)} \right|, \tag{C.5}$$

where we insert the orbital frequency of the strongest coupled eigenmode ω_e into the susceptibility $\chi(\omega_0)$. In Eq. (C.5), $\kappa_{1,2,\mathrm{int}}$ represents the coupling through port 1 and 2 of the resonator and the internal loss rate, respectively. In addition, the susceptibility is given by

$$\chi(\omega_0) = \frac{g^2}{(\omega_0 - \omega_e) + i\gamma}, \tag{C.6}$$

where $g/2\pi$ is fixed at 5 MHz (based on the estimate from section 2.4.2) and $\gamma/2\pi$ is adjusted to get good agreement for $N = 1$. For larger Wigner molecules, we do not further adjust γ because all modes remain far detuned from the cavity resonance and therefore, the modeled traces depend only weakly on the linewidth[1]. This means we cannot make predictions on the linewidth of larger Wigner molecules based on agreement between experiment and simulation.

1. This also follows from the cavity frequency shift, which does not depend on γ if the orbital frequency stays far detuned from the cavity frequency: $\Delta f_0 = \mathrm{Re}(\chi(\omega_0)) = g^2(\omega_0 - \omega_e)/((\omega_0 - \omega_e)^2 + \gamma^2) \approx g^2/(\omega_0 - \omega_e)$ [53].

The simulated spectra for three and four-electron Wigner molecules do not agree as well with the data, as the $N = 1$ and $N = 2$ spectra. We attribute this to the larger size of the three and four-electron Wigner molecules, since the approximation of the electrostatic potential in Eq. (C.1) only holds for small x, y around the potential minimum. In addition, each measured Wigner molecule spectrum was averaged about 500 times which blurs sharp features, such as the one in the modeled three-electron spectrum.

APPENDIX D

ESTIMATE OF LIQUID HELIUM RINGDOWN TIME

It may seem surprising that turning off the pulse tube cooler has little effect on the coherence of a single electron, as was stated in section 4.7. However, at $T = 20$ mK liquid helium is a very low-viscosity superfluid whose excitations have been exploited in several optomechanics experiments [82, 84, 86]. We estimate the damping time for liquid helium surface waves below.

The damping time of the reservoir fluctuations can be estimated from $\tau = Q/\omega_{\mathrm{He}}$, where Q is the quality factor of the helium surface vibrations and ω_{He} the fundamental vibration mode of the helium surface. We may treat the helium surface in the cylindrical reservoir as a drum with clamped edges, and the fundamental vibration frequency is related to the wavelength via the anomalous dispersion $\omega_{\mathrm{He}}^2 = gk_{\mathrm{He}}$, where we neglect the short-wavelength contribution due to surface tension (Eq. (1.14)). Clamped boundary conditions imply $k_{\mathrm{He}} = p_{01}/r$, where $p_{01} \approx 2.4$ is the first zero of the Bessel function J_0. This gives a fundamental frequency $f_0 = \frac{1}{2\pi}\sqrt{gp_{01}/r} \approx 15$ Hz, assuming a cylindrical reservoir of diameter 5 mm. The dominant mode in the spectrum of Fig. 4.3b occurs at 5.6 Hz. This discrepancy may be due to larger ($r \approx 15$ mm), unexpected reservoirs inside the sample box. Nevertheless, this estimate gives a fundamental frequency of the right order of magnitude.

We estimate the quality factor of the dominant mode in Fig. 4.3b and find $Q \approx 700$ for the $f_0 = 5.6$ Hz peak. We may compare this with the expression from Ref. [78], which is valid for damping of short-wavelength surface waves. Extrapolation of their results to longer wavelengths gives $Q \propto \omega_{\mathrm{He}}/k_{\mathrm{He}} = 1/\sqrt{k_{\mathrm{He}}}$, and thus $Q \sim 10^2 - 10^3$, which agrees with our measured value. Plugging in these values yields an estimated damping time of $\tau = \frac{Q}{\omega_{\mathrm{He}}} \approx 20$ s, which should scale linearly with the reservoir radius r.

We have tried to turn off the pulse tube for as long as 120 seconds before measuring the electron coherence time and even though this is longer than the estimated damping time, we have not observed a decrease in electron linewidth. It is possible that we have

underestimated the quality factor, or the electron temperature increased during the period the cooling was stopped. This could occur through heating from the fill lines, even though we did not observe a direct increase in mixing chamber temperature. Further research is needed to fully understand the observed results or alternatively, the experiment may be performed in a wet dilution refrigerator (i.e. a refrigerator without pulse tube cooler).

APPENDIX E

MEASUREMENTS AT LARGER V_{RES}

The vibrating electron reservoir complicates sensitive measurements of electrons in the dot, since it causes a time-dependent resonance frequency jitter which obscures small frequency shifts. The resonance frequency jitter originates from helium vibrations, which modulate the electron ensemble's frequency and in turn modulate the cavity's resonance frequency. Fig. E.1 shows that σ_f diverges at $V_{\mathrm{res}} \approx 0.4$ V, where the ensemble's frequency approaches the cavity's resonance, and decreases monotonically for larger values of V_{res}, because the ensemble is far off-resonant and less sensitive to a change in helium thickness. Therefore, working at a higher bias voltage $V_{\mathrm{res}} = 1.0$ V decreases the resonance frequency jitter by a factor of 2, and it is worth measuring the single-electron crossing with the resonator in this regime.

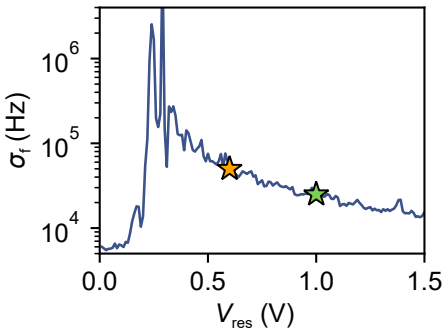

Figure E.1: Resonance frequency jitter due to a vibrating electron reservoir, as function of the bias voltage V_{res}. Since all measurements presented in chapter 4 were performed at a resonator bias voltage of $V_{\mathrm{res}} = 0.6$ V (orange star), a decrease in resonance frequency jitter is possible by working at a larger bias voltage, such as $V_{\mathrm{res}} = 1.0$ V (green star).

At $V_{\mathrm{res}} = 1.0$ V, the single-electron crossing voltage occurs for larger $V^*_{\mathrm{trap}} \approx 0.36$ V compared with $V_{\mathrm{res}} = 0.6$ V (see Eq. (2.18)), and the dot's loading voltage is slightly higher as well. Besides that we manage to obtain a similar single-electron spectrum as in Fig. 4.6, and we do not observe a significant change in single-electron linewidth. Therefore, the measured linewidth seems unaffected by the resonator bias voltage.

We also investigate the role of the guard electrodes on the single-electron spectrum (Fig. E.2). The resonator guards and trap guards deform dot's the electrostatic potential and control the position of the potential minimum inside the dot. For more negative V_{tg} and more positive V_{rg}, the electron moves towards the electron reservoir until it unloads, as indicated by the red arrows in Fig. E.2. Comparing both figures indicates that a positive resonator guard voltage has the equivalent effect as a negative trap guard voltage, which can be explained by the symmetry of the dot and the lever arms of similar magnitude (Fig. 2.8). The single-electron spectroscopy varies wildly with V_{rg} and V_{tg} because the coupling, frequency and anharmonicity vary with the electron position along the channel and affect the transmission spectrum.

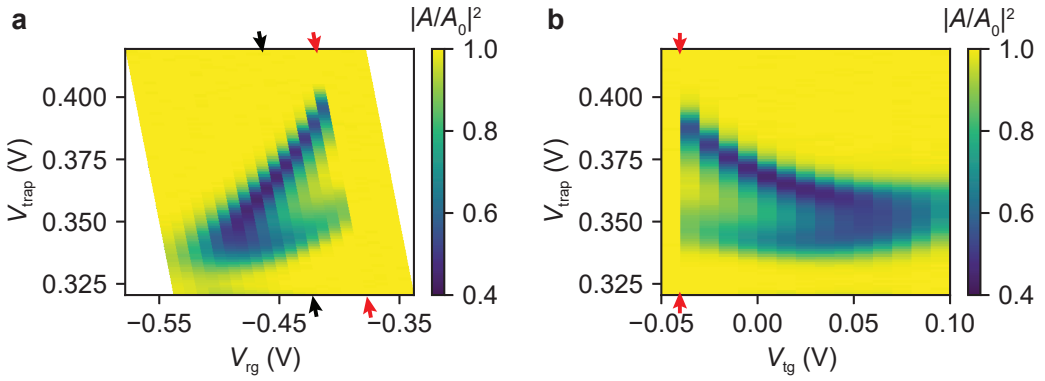

Figure E.2: Resonator spectroscopy of a single electron as function of the two guard electrode voltages V_{rg} (left) and V_{tg} (right). These measurements were taken at $V_{\mathrm{res}} = 1.0$ V with a probe tone on resonance ($f_p = f_0$). The reduction in transmission (dark blue) occurs when the single-electron frequency approaches f_0. The data in (b) was taken with V_{rg} biased at the black arrows in (a) and shows that the trap guard electrode has a similar, but opposite effect as the resonator guard electrode, which is due to the symmetry of the dot. Finally, the red arrows show the voltages for which the electron can no longer be contained inside the dot.

APPENDIX F

DESCRIPTION OF THE LOCKING CIRCUIT

The work presented in Chapter 5 showed that we were able to detect the microwave resonator response due to varying amounts of helium on top of the resonator and control the amount of liquid helium on the resonator using electric fields. We combined these two ingredients to actively stabilize the liquid helium surface using an analog control circuit (Fig. F.1).

The electrical circuit of Figs. F.1 and F.2 consists of a cascade of standard operational amplifiers circuits and transforms the demodulated resonator transmission $Q(f)$, which varies due to the vibrations on the helium surface, into a control voltage $u(f)$ that actively dampens helium vibrations. Below we deconstruct this circuit into separate blocks and briefly describe each block's purpose.

The demodulated resonator transmission from the IQ-mixer $Q(f)$ enters the circuit on the left of Fig. F.2, where any common-mode noise is rejected first. The filtered signal is then amplified by an inverting amplifier (orange block) with adjustable gain. The next stage (green block) subtracts $Q(f)$ from the setpoint $s(f)$ using a summing circuit and returns the error signal $e(f) = Q(f) - s(f)$. Before passing on the error signal, a unity gain buffer (light blue) resets the output impedance to $Z_{\text{out}} = 0$.

The proportional feedback comes from the dark blue block labeled "Proportional gain". This op-amp circuit has a DC gain $K(f) = K_p$ that can be adjusted *in-situ* by swapping out the resistor or adjusting the potentiometer labeled "total gain". The final stage sums the error signal, an adjustable output offset, and the output of an external voltage ramp circuit which can be turned on or off with a switch. This external circuit consists of op-amps and diodes and produces a periodic ramp that can be used to verify that $Q(f)$ follows the control voltage $u(f)$. When the feedback loop is closed to cancel vibrations, this circuit is turned off.

With the feedback loop closed and set up properly, we can monitor residual noise due to helium vibrations in the "error output" terminal of the circuit. We retrieve the spectra of

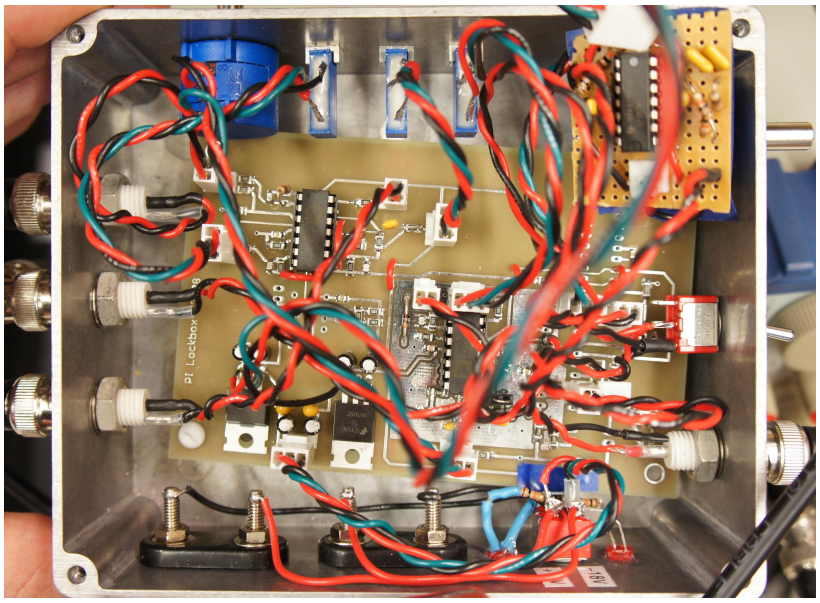

Figure F.1: Photograph of the locking circuit used to cancel helium vibrations. The printed circuit board contains the circuit shown in Fig. F.2 and is shielded by a metal box with various feedthroughs for the power, control signal $Q(f)$ and error output $e(f)$. The setpoint $s(f)$, error offset and several gains are controlled with blue potentiometers in the top of the figure. In addition, a separate circuit in the top right generates a voltage ramp which is used to verify the resonator's response before closing the feedback loop.

Fig. 5.5c by recording the error output as function of time (while the setpoint $s(f) = 0$) and applying a Fast Fourier transform (FFT) to the measured time series. The power spectral density of the error output e, sampled with N points over a time t_{meas}, is proportional to the Fourier transform

$$\text{PSD}(f) = \frac{t_{\text{meas}}}{N^2} \left| \sum_{n=1}^{N} e[n] e^{-2\pi i f n} \right|^2 , \tag{F.1}$$

and has units V^2/Hz. We show the amplitude spectral density, which is the square root of the PSD, in Fig. 5.5c. Since the integrated amplitude spectral density decreases dramatically compared with the open feedback loop, we conclude that the analog circuit performs as expected.

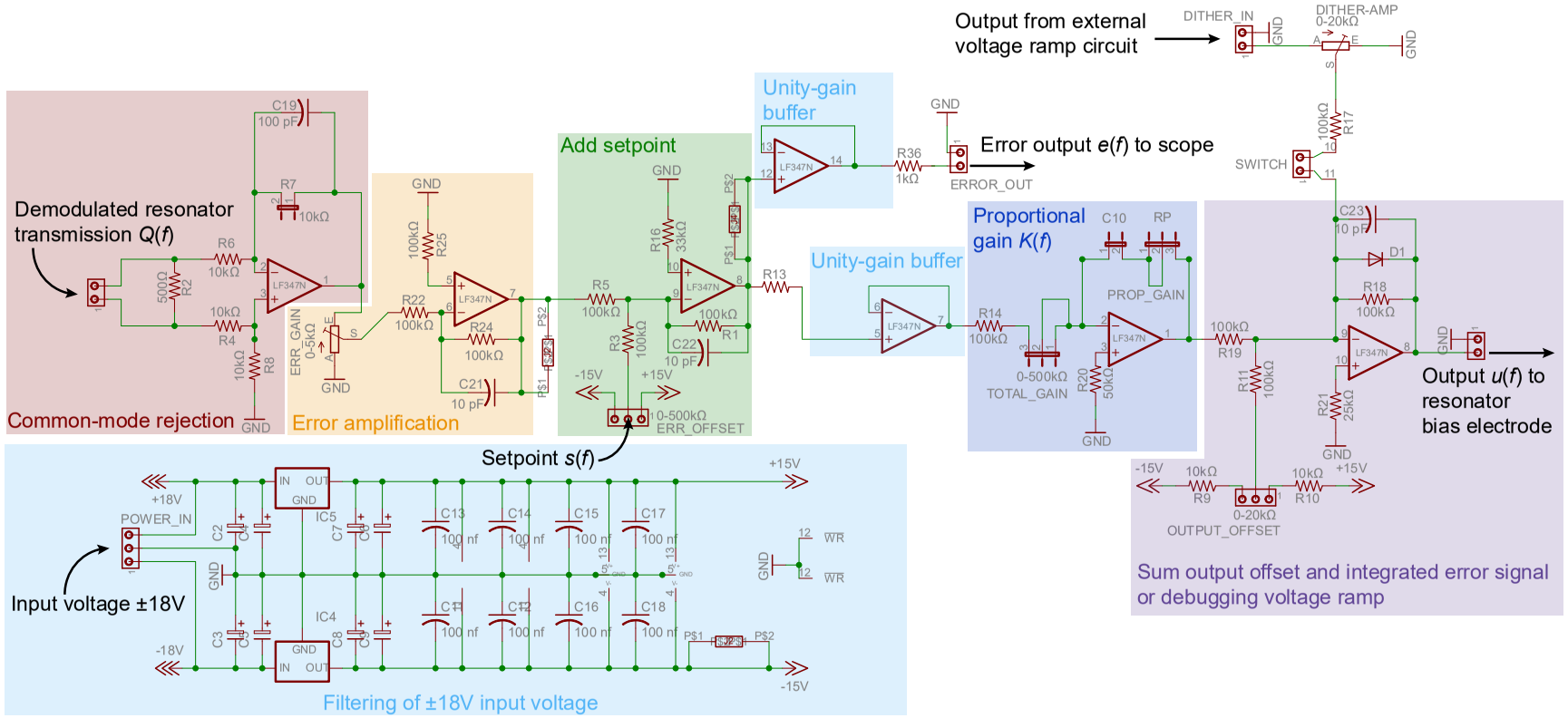

Figure F.2: A simplified schematic of the proportional-integration locking circuit used to stabilize the liquid helium surface. This design was adapted from a design by Ariel Sommer from the Simon lab at Univeristy of Chicago and constructed with the help of David McKay. All op-amps in this circuit are Texas Instruments LF347N, which have a large 3 MHz bandwidth and high slew rate of 13 V/µs. Careful balancing of resistor values on the non-inverting inputs of the op-amps ensures common-mode rejection. External signal inputs and outputs are shown as black arrows.

Bibliography

1. Monarkha, Y. & Kono, K. *Two-Dimensional Coulomb Liquids and Solids* ISBN: 3-540-20754-6 (Springer-Verlag, Berlin, 2004).

2. Jackson, J. D. *Classical electrodynamics* 3rd ed. ISBN: 9780471309321 (Wiley, New York, NY, 1999).

3. Chase, C., Maxwell, E. & Millett, W. The dielectric constant of liquid helium. *Physica* **27,** 1129 –1145. ISSN: 0031-8914 (1961).

4. Huang, Y. & Maris, H. J. Effective Mass of an Electron Bubble in Superfluid Helium-4. *Journal of Low Temperature Physics* **186,** 208–216. ISSN: 1573-7357 (2017).

5. Vadakkumbatt, V., Joseph, E., Pal, A. & Ghosh, A. Studying electrons on curved surfaces by trapping and manipulating multielectron bubbles in liquid helium. *Nature Communications* **5.** Article, 4571 (2014).

6. Sommer, W. T. Liquid Helium as a Barrier to Electrons. *Phys. Rev. Lett.* **12,** 271–273 (1964).

7. Grimes, C. C., Brown, T. R., Burns, M. L. & Zipfel, C. L. Spectroscopy of electrons in image-potential-induced surface states outside liquid helium. *Phys. Rev. B* **13,** 140–147 (1976).

8. Platzman, P. M. & Dykman, M. I. Quantum Computing with Electrons Floating on Liquid Helium. *Science* **284,** 1967–1969 (1999).

9. Dykman, M. I., Platzman, P. M. & Seddighrad, P. Qubits with electrons on liquid helium. *Phys. Rev. B* **67,** 155402 (2003).

10. Kawakami, E., Elarabi, A. & Konstantinov, D. Image-Charge Detection of the Rydberg States of Surface Electrons on Liquid Helium. *Phys. Rev. Lett.* **123,** 086801 (2019).

11. Klindworth, M., Melzer, A., Piel, A. & Schweigert, V. A. Laser-excited intershell rotation of finite Coulomb clusters in a dusty plasma. *Phys. Rev. B* **61,** 8404–8410 (2000).

12. Shapir, I. *et al.* Imaging the electronic Wigner crystal in one dimension. *Science* **364,** 870–875. ISSN: 0036-8075 (2019).

13. An Dinh, V. & Saitoh, M. Cyclotron Resonance of Wigner Crystal in Semiconductor Heterostructures. *Journal of the Physical Society of Japan* **72,** 1779–1783 (2003).

14. Crandall, R. & Williams, R. Crystallization of electrons on the surface of liquid helium. *Physics Letters A* **34,** 404 –405. ISSN: 0375-9601 (1971).

15. Grimes, C. C. & Adams, G. Evidence for a Liquid-to-Crystal Phase Transition in a Classical, Two-Dimensional Sheet of Electrons. *Phys. Rev. Lett.* **42,** 795–798 (1979).

16. Ikegami, H., Akimoto, H. & Kono, K. Melting of a quasi-one-dimensional Wigner crystal: Electrons on superfluid ^{4}He in a narrow channel. *Phys. Rev. B* **82,** 201104 (2010).

17. Rees, D. G. *et al.* Structural order and melting of a quasi-one-dimensional electron system. *Phys. Rev. B* **94,** 045139 (2016).

18. Rees, D. G. *et al.* Point-Contact Transport Properties of Strongly Correlated Electrons on Liquid Helium. *Phys. Rev. Lett.* **106,** 026803 (2011).

19. Rees, D. G., Beysengulov, N. R., Lin, J.-J. & Kono, K. Stick-Slip Motion of the Wigner Solid on Liquid Helium. *Phys. Rev. Lett.* **116,** 206801 (2016).

20. Rees, D. G., Yeh, S.-S., Lee, B.-C., Kono, K. & Lin, J.-J. Bistable transport properties of a quasi-one-dimensional Wigner solid on liquid helium under continuous driving. *Phys. Rev. B* **96,** 205438 (2017).

21. Ikegami, H., Akimoto, H., Rees, D. G. & Kono, K. Evidence for Reentrant Melting in a Quasi-One-Dimensional Wigner Crystal. *Phys. Rev. Lett.* **109,** 236802 (2012).

22. Pecker, S. *et al.* Observation and spectroscopy of a two-electron Wigner molecule in an ultraclean carbon nanotube. *Nature Physics* **9,** 576–581 (2013).

23. Torii, R. *et al.* Removal of superfluid helium films from surfaces below 0.1 K. *Review of Scientific Instruments* **63,** 230–234 (1992).

24. Pobell, F. *Matter and Methods at Low Temperatures* ISBN: 978-3-540-46356-6 (Springer-Verlag, Berlin, Heidelberg, 2007).

25. Everitt, C. W. F., Atkins, K. R. & Denenstein, A. Third Sound in Liquid Helium Films. *Phys. Rev.* **136,** A1494–A1499 (1964).

26. Campbell, C. E. in *Excitations in Two-Dimensional and Three-Dimensional Quantum Fluids* (eds Wyatt, A. F. G. & Lauter, H. J.) 159–171 (Springer US, Boston, MA, 1991). ISBN: 978-1-4684-5937-1.

27. Edwards, D. & Saam, W. in (ed Brewer, D.) 283 –369 (Elsevier, 1978).

28. Schuster, D. I., Fragner, A., Dykman, M. I., Lyon, S. A. & Schoelkopf, R. J. Proposal for Manipulating and Detecting Spin and Orbital States of Trapped Electrons on Helium Using Cavity Quantum Electrodynamics. *Phys. Rev. Lett.* **105,** 040503 (2010).

29. Constable, J. H., Clark, C. F. & Gaines, J. R. The dielectric constant of H2, D2, and HD in the condensed phases. *Journal of Low Temperature Physics* **21,** 599–617. ISSN: 1573-7357 (1975).

30. Papageorgiou, G. *et al.* Counting Individual Trapped Electrons on Liquid Helium. *Applied Physics Letters* **86,** 153106 (2005).

31. Glasson, P. *et al.* Trapping single electrons on liquid helium. *Journal of Physics and Chemistry of Solids* **66.** Proceedings of the ISSP International Symposium (ISSP-9)on Quantum Condensed System, 1539 –1543 (2005).

32. Rousseau, E. *et al.* Addition spectra of Wigner islands of electrons on superfluid helium. *Phys. Rev. B* **79,** 045406 (2009).

33. Bedanov, V. M. & Peeters, F. M. Ordering and phase transitions of charged particles in a classical finite two-dimensional system. *Phys. Rev. B* **49,** 2667–2676 (1994).

34. Bonitz, M. *et al.* Classical and quantum Coulomb crystals. *Physics of Plasmas* **15,** 055704 (2008).

35. Filinov, A. V., Bonitz, M. & Lozovik, Y. E. Wigner Crystallization in Mesoscopic 2D Electron Systems. *Phys. Rev. Lett.* **86,** 3851–3854 (2001).

36. DiVincenzo, D. P. The Physical Implementation of Quantum Computation. *Fortschritte der Physik* **48,** 771–783 (2000).

37. Nielsen, M. A. & Chuang, I. L. *Quantum Computation and Quantum Information: 10th Anniversary Edition* 10th. ISBN: 1107002176, 9781107002173 (Cambridge University Press, New York, NY, USA, 2011).

38. Lyon, S. A. Spin-based quantum computing using electrons on liquid helium. *Phys. Rev. A* **74,** 052338 (2006).

39. Haroche, S. & Raimond, J. M. *Exploring the Quantum: Atoms, Cavities, and Photons* (Oxford Univ. Press, Oxford, 2006).

40. Schuster, D. I. *Circuit Quantum Electrodynamics* PhD thesis (Yale University, 2007).

41. Mi, X. *et al.* A coherent spin-photon interface in silicon. *Nature* **555,** 599–603 (2018).

42. Landig, A. J. *et al.* Coherent spin–photon coupling using a resonant exchange qubit. *Nature* (2018).

43. Samkharadze, N. *et al.* Strong spin-photon coupling in silicon. *Science* **359,** 1123–1127 (2018).

44. Schuster, D. I. *et al.* High-Cooperativity Coupling of Electron-Spin Ensembles to Superconducting Cavities. *Phys. Rev. Lett.* **105,** 140501 (2010).

45. Creedon, D. L. *et al.* Strong coupling between $P1$ diamond impurity centers and a three-dimensional lumped photonic microwave cavity. *Phys. Rev. B* **91,** 140408 (2015).

46. Chen, J., Zadorozhko, A. A. & Konstantinov, D. Strong coupling of a two-dimensional electron ensemble to a single-mode cavity resonator. *Phys. Rev. B* **98,** 235418 (2018).

47. Gerry, C. & Knight, P. *Introductory Quantum Optics* doi:10.1017/CBO9780511791239 (Cambridge University Press, 2004).

48. Shearrow, A. *et al.* Atomic layer deposition of titanium nitride for quantum circuits. *Applied Physics Letters* **113,** 212601 (2018).

49. Stockklauser, A. *et al.* Strong Coupling Cavity QED with Gate-Defined Double Quantum Dots Enabled by a High Impedance Resonator. *Phys. Rev. X* **7,** 011030 (2017).

50. Martinis, J. M., Nam, S., Aumentado, J., Lang, K. M. & Urbina, C. Decoherence of a superconducting qubit due to bias noise. *Phys. Rev. B* **67,** 094510 (2003).

51. Walls, D. & Milburn, G. *Quantum Optics* ISBN: 9783540285731 (Springer Berlin Heidelberg, 2008).

52. Cottet, A. *et al.* Cavity QED with hybrid nanocircuits: from atomic-like physics to condensed matter phenomena. *Journal of Physics: Condensed Matter* **29,** 433002 (2017).

53. Viennot, J. *Charge and spin dynamics in a hybrid circuit quantum electrodynamics architecture* PhD thesis (École normale supérieure, 2013).

54. Wallraff, A. *et al.* Strong coupling of a single photon to a superconducting qubit using circuit quantum electrodynamics. *Nature* **431,** 162–167 (2004).

55. Mi, X., Cady, J. V., Zajac, D. M., Deelman, P. W. & Petta, J. R. Strong coupling of a single electron in silicon to a microwave photon. *Science* **355,** 156–158 (2017).

56. Abdurakhimov, L. V., Yamashiro, R., Badrutdinov, A. O. & Konstantinov, D. Strong Coupling of the Cyclotron Motion of Surface Electrons on Liquid Helium to a Microwave Cavity. *Phys. Rev. Lett.* **117,** 056803 (2016).

57. Yang, G. *et al.* Coupling an Ensemble of Electrons on Superfluid Helium to a Superconducting Circuit. *Phys. Rev. X* **6,** 011031 (2016).

58. Marty, D. Stability of two-dimensional electrons on a fractionated helium surface. *Journal of Physics C: Solid State Physics* **19,** 6097–6104 (1986).

59. Takita, M. & Lyon, S. A. Isolating electrons on superfluid helium. *Journal of Physics: Conference Series* **568,** 052034 (2014).

60. Beysengulov, N. R. *et al.* Structural Transitions in a Quasi-1D Wigner Solid on Liquid Helium. *Journal of Low Temperature Physics* **182,** 28–37. ISSN: 1573-7357 (2016).

61. Koch, J. *et al.* Charge-insensitive qubit design derived from the Cooper pair box. *Phys. Rev. A* **76,** 042319 (2007).

62. Pozar, D. M. *Microwave Engineering, Fourth Edition* ISBN: 978-0-470-63155-3 (John Wiley & Sons, Inc., Hoboken, NJ, 2012).

63. Mi, X. *Circuit Quantum Electrodynamics with Silicon Charge and Spin Qubits* PhD thesis (Princeton University, 2018).

64. Mi, X. *et al.* Circuit quantum electrodynamics architecture for gate-defined quantum dots in silicon. *Applied Physics Letters* **110,** 043502 (2017).

65. Swartz, E. T. & Pohl, R. O. Thermal boundary resistance. *Rev. Mod. Phys.* **61,** 605–668 (1989).

66. Bienfait, A. *Magnetic resonance with quantum microwaves* PhD thesis (Université Paris-Saclay, 2016).

67. Castellanos-Beltran, M. A., Irwin, K. D., Hilton, G. C., Vale, L. R. & Lehnert, K. W. Amplification and squeezing of quantum noise with a tunable Josephson metamaterial. *Nature Physics* **4,** 929–931 (2008).

68. Mueller, F. *et al.* Printed circuit board metal powder filters for low electron temperatures. *Review of Scientific Instruments* **84,** 044706 (2013).

69. Schweigert, V. A. & Peeters, F. M. Spectral properties of classical two-dimensional clusters. *Phys. Rev. B* **51,** 7700–7713 (1995).

70. Tarucha, S., Austing, D. G., Honda, T., van der Hage, R. J. & Kouwenhoven, L. P. Shell Filling and Spin Effects in a Few Electron Quantum Dot. *Phys. Rev. Lett.* **77,** 3613–3616 (1996).

71. Tarucha, S., Austing, D. G., Honda, T., van der Hage, R. & Kouwenhoven, L. P. Atomic-Like Properties of Semiconductor Quantum Dots. *Japanese Journal of Applied Physics* **36,** 3917–3923 (1997).

72. Schuster, D. I. *et al.* ac Stark Shift and Dephasing of a Superconducting Qubit Strongly Coupled to a Cavity Field. *Phys. Rev. Lett.* **94,** 123602 (2005).

73. Desjardins, M. M. *et al.* Observation of the frozen charge of a Kondo resonance. *Nature* **545,** 71–74 (2017).

74. Ferdinand, B., Bothner, D., Kleiner, R. & Koelle, D. Tunable Superconducting Two-Chip Lumped-Element Resonator. *Phys. Rev. Applied* **11,** 034050 (2019).

75. Xu, M. *et al.* Frequency-tunable high-Q superconducting resonators via wireless control of nonlinear kinetic inductance. *Applied Physics Letters* **114,** 192601 (2019).

76. Kennedy, O. *et al.* Tunable Nb Superconducting Resonator Based on a Constriction Nano-SQUID Fabricated with a Ne Focused Ion Beam. *Phys. Rev. Applied* **11,** 014006 (2019).

77. Vissers, M. R. *et al.* Frequency-tunable superconducting resonators via nonlinear kinetic inductance. *Applied Physics Letters* **107,** 062601 (2015).

78. Roche, P., Deville, G., Keshishev, K. O., Appleyard, N. J. & Williams, F. I. B. Low Damping of Micron Capillary Waves on Superfluid 4He. *Phys. Rev. Lett.* **75,** 3316–3319 (1995).

79. Ikegami, H. *et al.* Anomalous Quasiparticle Reflection from the Surface of a ^{3}He-^{4}He Dilute Solution. *Phys. Rev. Lett.* **119,** 195302 (2017).

80. Pelliccione, M., Sciambi, A., Bartel, J., Keller, A. J. & Goldhaber-Gordon, D. Design of a scanning gate microscope for mesoscopic electron systems in a cryogen-free dilution refrigerator. *Review of Scientific Instruments* **84,** 033703 (2013).

81. Souris, F., Rojas, X., Kim, P. H. & Davis, J. P. Ultralow-Dissipation Superfluid Micromechanical Resonator. *Phys. Rev. Applied* **7,** 044008 (2017).

82. Kashkanova, A. D. *et al.* Superfluid Brillouin optomechanics. *Nature Physics* **13.** Article, 74–79 (2016).

83. Childress, L. *et al.* Cavity optomechanics in a levitated helium drop. *Phys. Rev. A* **96,** 063842 (2017).

84. Lorenzo, L. A. D. & Schwab, K. C. Superfluid optomechanics: coupling of a superfluid to a superconducting condensate. *New Journal of Physics* **16,** 113020 (2014).

85. De Lorenzo, L. A. & Schwab, K. C. Ultra-High Q Acoustic Resonance in Superfluid 4He. *Journal of Low Temperature Physics* **186,** 233–240. ISSN: 1573-7357 (2017).

86. Harris, G. I. *et al.* Laser cooling and control of excitations in superfluid helium. *Nature Physics* **12.** Article, 788–793 (2016).

87. Byeon, H. *et al.* Anomalous Attenuation of Piezoacoustic Surface Waves by Liquid Helium Thin Films. *Journal of Low Temperature Physics* **195,** 336–342. ISSN: 1573-7357 (2019).

88. Manninen, M. S., Ranni, A., Rysti, J., Todoshchenko, I. A. & Tuoriniemi, J. T. Surface Waves on the Superfluids ^{3}He and ^{4}He. *Journal of Low Temperature Physics* **183,** 399–415 (2016).

89. Van Kann, F. & Winterflood, J. Simple method for absolute calibration of geophones, seismometers, and other inertial vibration sensors. *Review of Scientific Instruments* **76,** 034501 (2005).

90. Ryou, A. & Simon, J. Active cancellation of acoustical resonances with an FPGA FIR filter. *Review of Scientific Instruments* **88,** 013101 (2017).

91. Ghannam, A., Viallon, C., Bourrier, D. & Parra, T. Dielectric microwave characterization of the SU-8 thick resin used in an above IC process, 1041–1044 (2009).

92. Bechhoefer, J. Feedback for physicists: A tutorial essay on control. *Rev. Mod. Phys.* **77,** 783–836 (2005).

93. Todoshchenko, I., Savin, A., Haataja, M., Kaikkonen, J.-P. & Hakonen, P. J. Quartz tuning fork as a probe of surface oscillations. *Applied Physics Letters* **110,** 071601 (2017).

94. Callaghan, F. D., Yu, X. & Mellor, C. J. Dynamic force microscopy in superfluid helium. *Applied Physics Letters* **81,** 916–918 (2002).

95. Eichler, C., Sigillito, A. J., Lyon, S. A. & Petta, J. R. Electron Spin Resonance at the Level of 10^4 Spins Using Low Impedance Superconducting Resonators. *Phys. Rev. Lett.* **118,** 037701 (2017).

96. Pioro-Ladrière, M. *et al.* Electrically driven single-electron spin resonance in a slanting Zeeman field. *Nature Physics* **4,** 776–779 (2008).

97. Kong, M., Partoens, B. & Peeters, F. M. Transition between ground state and metastable states in classical two-dimensional atoms. *Phys. Rev. E* **65,** 046602 (2002).